Linear Oscillations of Compact Stars in the Cowling Approximation

DISSERTATION

zur Erlangung des Grades eines Doktors
der Naturwissenschaften
der Fakultät für Mathematik und Physik
der Eberhard-Karls-Universität zu Tübingen

vorgelegt von
Erich Gaertig
aus Piešt'any

2008

Tag der mündlichen Prüfung: 12.12.2008
Dekan: Prof. Dr. Wolfgang Knapp
1. Berichterstatter: Prof. Dr. Kostas Kokkotas
2. Berichterstatter: Prof. Dr. Hanns Ruder

Abstract

During their evolution, relativistic stars may undergo oscillations which can become unstable under certain conditions. Newly born neutron stars are expected to oscillate wildly during their creation shortly after a supernovae collapse. They are also expected to oscillate if they are members of binary systems and there is tidal interaction or mass and angular momentum transfer from the companion star. Rotation strongly affects these oscillations and perturbed stars can become unstable if they rotate faster than some critical velocities. During these oscillatory phases of their lives, compact stars emit copious amounts of gravitational waves which together with viscosity tend to suppress the oscillations. These oscillations are divided into distinct families according to the restoring force; each of these classes providing valuable information about the stars interior. It is therefore of particular interest to investigate pulsations of relativistic objects.

During the last two decades, these studies have become even more important due to the relations of the oscillations and instabilities to the emission of gravitational waves and the possibility of getting information about the stellar parameters (mass, radius, equation of state) by the proper analysis of the oscillation spectrum. Still, all these studies were mainly dealing with non-rotating stars, because the combination of rotation and general relativity made both the analytic and numerical studies extremely involved. This led to certain approximations in studying rotating stars in general relativity; the most obvious of them is probably the restriction to small rotation rates which has also been used extensively in the Newtonian theory of stellar oscillations.

Although most of our understanding on the oscillations of relativistic stars is due to perturbative studies, recently it became possible to study stellar oscillations using evolutions of the non-linear equations of motion for the fluid. Finally, differential rotation is another key issue that is believed to play an important role in the dynamics of nascent neutron stars. Actually it is associated with dynamical instabilities both for fast and slowly rotating neutron stars and affects the onset of secular instabilities; still it has not yet been studied extensively and remains an open issue.

Since rotational instabilities are typically connected with fast rotating stars, it is of great importance to study the oscillations of this type of objects. As a first step one can drop the slow rotation-approximation but freeze the spacetime perturbations or in the best case to freeze the radiative part of these perturbations. This was the approach used up to now for most of the studies of the oscillations of fast rotating relativistic stars either in perturbative approaches or in non-linear (but axisymmetric) cases.

In this PhD-thesis we will present a new approach based on 2D evolution of the perturbation equations which seems to be promising for the study of the oscillations and instabilities of fast rotating neutron stars. This is the first study of its kind; earlier 2D perturbative studies have been done either in Newtonian theory or in reduction to an eigenvalue problem. The advantage of this method is that can be easily extended to include differential rotation or the perturbations of the spacetime. On the other hand it provides a robust tool in studying the onset of rotational instabilities in fast rotating neutron stars while as it has been demonstrated here one can get easily results for realistic equations of state which is vital for developing gravitational wave asteroseismology.

Contents

1 Introduction 7
1.1 Overview . . . 7
1.1.1 Classical Stellar Oscillations . . . 7
1.1.2 Relativistic Stellar Oscillations . . . 9
1.1.3 Gravitational Wave Asteroseismology . . . 11
1.2 Methodology . . . 12
1.3 Conventions . . . 14

2 The Perturbation Equations 15
2.1 The 3+1 Split in General Relativity . . . 15
2.2 Linear Perturbation Theory . . . 18
2.3 The Cowling Approximation . . . 20
2.4 The Metric and the Energy-Momentum–Tensor . . . 21
2.5 Derivation of the Linearized Perturbation Equations . . . 23
2.5.1 The Equations . . . 24
2.5.2 Some Properties of the Equations . . . 26
2.5.3 Boundary Conditions . . . 28

3 Numerical Implementations 31
3.1 A Brief Introduction to Spectral Methods . . . 31
3.2 Pros and Cons of Spectral Methods . . . 35
3.3 Layout of the Computational Domain . . . 36
3.4 The Time-Evolution Scheme . . . 41
3.5 Results with the Pseudospectral Approach . . . 44
3.6 The Finite Difference Algorithm . . . 46
3.6.1 Crank-Nicholson Methods . . . 47
3.7 Results with the Finite Difference Approach . . . 49
3.8 Artificial Viscosity . . . 51
3.9 Post-Processing Routines . . . 54
3.9.1 Discrete Fourier Transforms and Data Windowing . . . 54
3.9.2 Peak Localization and Mode Recycling . . . 58

4 Results 61
4.1 The Background Models . . . 61
4.2 First Axisymmetric Validation Runs . . . 63
4.3 Convergence Tests . . . 71
4.4 The Axisymmetric Case . . . 73
4.4.1 Polar Perturbations . . . 73
4.4.2 Axial Perturbations . . . 77
4.5 The CFS-Instability . . . 79
4.6 Additional Background Models . . . 82
4.7 First Non-Axisymmetric Test Runs . . . 83
4.8 Distinguishing Counter- And Corotating Modes . . . 85
4.9 The Non-Axisymmetric Case . . . 88

4.9.1 Polar Perturbations 90
4.9.2 Axial Perturbations 95

5 Summary and Outlook 101

A Proofs about the Perturbation Equations 105
A.1 A Toy Model 105
A.2 Analytical Proofs 107

B Documentation of the Software Package 109
B.1 General Layout 109
B.2 The Modules 110
B.2.1 `akm` 110
B.2.2 `initial_data_generator` 110
B.2.3 `time_evolution` 110
B.2.4 `dft` 111
B.2.5 `recycling` 111
B.2.6 `convenience` 111

At terrestrial temperatures matter has complex properties which are likely to prove most difficult to unravel; but is is reasonable to hope that in a not too distant future we shall be competent to understand such a simple thing as a star.

Arthur Stanley Eddington
(1882-1944)

1
Introduction

1.1 Overview

1.1.1 Classical Stellar Oscillations

The study of how and why certain types of stars pulsate has a very long history. Effectively it already started with Newton who studied the gravitational equilibrium of homogeneous uniformly rotating bodies. Based on simple arguments he calculated that the Earth should have the shape of an oblate spheroid with an ellipticity of $\epsilon \sim 1/230$. Interestingly enough during these days there was a strong debate whether the Earth was actually oblate according to Newton or rather prolate; a concept favoured by the Cassinis. Finally, geodetic measurements in Lapland showed that Newton was right. Roughly 50 years later MacLaurin generalized Newtons results for homogeneous bodies that rotate with a uniform angular velocity around its symmetry axis; the corresponding equilibrium figures are called MacLaurin spheroids. It is worth mentioning that the shape of a rotating body is not uniquely determined by its angular velocity. In fact for each rotation rate less than a certain maximum there are two MacLaurin spheroids with different oblateness. A stability analysis showed furthermore that if one slightly changes the shape of such an equilibrium configuration, the spheroid will start to oscillate in various normal modes that, depending again on the ellipticity, are either stable, become degenerate at a bifurcation point or are dynamically unstable. In fact over nearly a century it was believed that MacLaurins solution were the only possible figures of equilibrium and it was Jacobi who showed that there exists also a class of stable triaxial configurations which solve the problem of uniformly rotating masses. At a point along the MacLaurin sequence where the frequency of a normal mode becomes zero this sequence bifurcates into the Jacobian sequence. For certain rotation rates there are now three equilibrium configurations possible; two axisymmetric ones belonging to the original class of MacLaurin and a third ellipsoid with three unequal axes belonging to the Jacobi sequence. Other very important contributions in this area of research were made by people like Poincaré, Dedekind, Riemann and Roche; see [1] as reference. Even though rather limited for real physical applications it is already evident from the homogeneous density case that the oscillation frequencies of perturbations depend on certain physical parameters like the rotation rate and the density; measuring these frequencies therefore reveals important information about stellar parameters. Now moving on from this rather mathematical approach to a more astrophysical one, it is well known that stars with a periodic change in brightness were an established phenomenon for centuries but only within the last hundred years it became clear that these variations are due to intrinsic pulsations of the stars themselves. These oscillations are generally accompanied by a corresponding change in luminosity; the most famous examples are maybe the Cepheids and the RR Lyrae stars. It was realized quite early (see [2]) that the oscillation periods of these classical variable stars are approximately given by their dynamical timescale which again is proportional to the mean density. There were theories that tried to explain the periodic variation in brightness by an eclipsing binary system but it was Eddington [3] who successfully applied the idea of a stellar pulsation to the problem.

Usually in order to solve the Newtonian equations of hydrodynamics one writes all background perturbations (usually velocity and pressure/density) as product of a radial function and an angular part which is further decomposed into spherical harmonics. Their harmonic indices l and m are used to parametrize the angular part while the radial part is labelled according to the number of nodes n its oscillation pattern has in the stellar interior. In todays language one would say that indeed most of the Cepheid variables are pulsating in the fundamental or the first overtone radial mode; i.e. $(n = 0, 1; l = 0)$. Since radial pulsations are more prominent observationally, quite naturally this was also the focus of the theoretical research. Within the 1940s more and more calculations were also done for $l \neq 0$-type of perturbations; Cowling [4] obtained analytical solutions for adiabatic nonradial oscillations of polytropes and Ledoux [5] obtained the rotational splitting of mode frequencies for uniformly rotating stars. The discovery of the famous solar five-minute oscillations in 1962 shows the large variety of nonradial modes; in the case of the sun they consist of sound waves with very high spherical harmonic degree $(l = 200 - 1000)$. Part of this richness is of course due to the additional degree of freedom in the polar index l, another reason is that instead of pressure being the only restoring force in the radial case now gravity enters the game as well. It is quite easy to see why the gravitational attraction cannot be the restoring force for the Cepheid stars. The change in the gravitational force is directed inwards if a star contracts and outwards if it expands but in order to push the perturbations back to equilibrium one would need it the other way round. So in general for a nonrotating Newtonian star there exist exactly two types of oscillations connected to the two types of restoring force. Based on the nomenclature originally invented by Cowling, we have

1. *(p)ressure modes:* These are acoustic waves, pretty much like sound waves in the air; the propagation mechanism is the same. The amplitude of these modes is large in the outer parts of the star but relatively small in the central regions. For increasing node number n, its frequency tends to infinity while for a given n the frequency is higher for modes with larger spherical polar index l and there are infinitely many of them.

2. *(g)ravity modes:* These modes are restored by gravity and acts in the following way. If a fluid element is moved upwards and is still heavier than the displaced fluid then buoyancy will push it back to its original position. Here we can again see the nonradial character of g-modes. In order to move vertically, a fluid element has to displace matter horizontally which introduces a nonradial perturbation component. The amplitude of these modes is larger in the central part and relatively small towards the surface. The mode frequencies are always smaller than in the pressure-driven case and with increasing node number n it gets even smaller; there are also infinitely many of them.

The *fundamental* or *f-mode* has an intermediate character; it has no radial nodes and its frequency is higher than the first g-mode but lower than the first p-mode.
When rotation is included, two kinds of fictitious forces have to be added to the hydrodynamical equations; the centrifugal and the Coriolis force. The first one may be written as a potential force an can be treated together with the gravitational potential. This new force will distort the spherical shape of the star and therefore lead to the question if the decomposition into spherical harmonics is still valid. However, for most stars the deviation from spherical symmetry is practically negligible so using the Y_{lm} is still a good approximation. This question will be more difficult to answer when we are talking about rapidly rotating neutron stars; more on that issue later. Apart from the minimal oblateness, the centrifugal force will also alter the frequencies of the f-, p- and g-mode but now new class of oscillation will follow from this force. This treatment is not possible with the Coriolis force though. It will also alter the frequencies of the already established modes but will also introduce a new class of oscillations.

3. *(i)nertial modes:* These modes are pushed back to equilibrium by the Coriolis force and therefore exist only in rotating stars; their frequency degenerates in the nonrotating case and is otherwise proportional to the angular velocity of the star, see [6] for example. They are mainly velocity perturbations and bear similarities to Rossby-waves which appear in the atmosphere and the oceans of the Earth. Non-axisymmetric inertial modes are therefore also called *r-modes*.

This last class also differs in another aspect from oscillations in nonrotating stars. Based on the spherical decomposition of the perturbation quantities one may ask how they behave under a space reflection around the origin, i.e. $r \to r$, $\theta \to \pi - \theta$ and $\varphi \to \pi + \varphi$. *Polar* or *even parity* harmonics change sign like $(-1)^l$ while *axial* or *odd parity* harmonics transform according to $(-1)^{l+1}$. While now p- and g-modes are of polar parity, the inertial modes are of odd parity. Therefore in the nonrotating Newtonian case there are no axial modes at all; it is rotation that adds the inertial modes as odd parity solution. In fact, this is not strictly true; if one considers a solid crust even in the nonrotating case there exist axial torsional modes (see [7]) but we will not consider them here. As some kind of closing remark about the rough sketch on stellar pulsation theory presented so far one may say that the study of star oscillations has turned out to be an outstandingly useful tool for investigating the internal structure of stars. The most famous example is of course our Sun. Nowadays thousands of individual modes can be observed and besides the detection of neutrinos it is the only possibility to probe the Solar interior. Pretty much like seismology on Earth can tell us about the various layers of the Earth this relatively new field of “helioseismology” helps to understand the composition of the Sun.

1.1.2 Relativistic Stellar Oscillations

When we move from ordinary stars to the final stages of stellar evolution the natural question is how one describes oscillations of the most compact objects known in the Universe, black holes and neutron stars. At such extreme conditions, Newtonian theory fails and has to be replaced by General Relativity. We will not discuss black hole perturbation theory here which was initiated by Regge and Wheeler in the late 1950s and continued by Zerilli ten years later; for a review see [8], [9]. Instead we focus on the study oscillations of nonrotating relativistic stars which started in the radial case with investigations by Chandrasekhar in 1964 [10] and were extended to the nonradial case in 1967 by a series of papers from Thorne and collaborators, see [11], [12], [13], [14], where they wanted to extend the well established Newtonian results to General Relativity. Since Einstein's theory predicts the existence of gravitational waves which are generated by periodic deformations of the compact star, a new dissipation mechanism occurred which removes energy from the perturbation and thereby damps the mode. Within the next 20 years or so the spacetime was thought to be a rather passive actor in this new field of research, only used as a medium on which the gravitational waves propagate. The relativistic counterparts of Newtonian polar perturbations were found, their frequencies were computed and the only additional feature was the calculation of damping times due to emission of gravitational waves. In 1986, Kokkotas and Schutz [15] constructed a simple toy model which showed the existence of a new family of modes, the *w-modes* and subsequent work [16], [17] confirmed their existence. In contrast to previously known fluid modes this new family hardly excite any fluid motion but it is the spacetime that now takes on a more active role and starts oscillating. Moreover they exist for both polar and axial parity so in contrast to Newtonian results for perfect fluids, also axial perturbations are possible for nonrotating stars. Soon, various sub-families of spacetime modes were found; some of them have very high damping rates, others only exist for very compact objects, see [18] for a survey. For a typical neutron star, p-mode frequencies are about $4-7$ kHz, the g-modes are in a regime below several 100 Hz and the classical w-modes can be found at around $5-10$ kHz.

Rotation affects the oscillation frequencies of relativistic stars in nearly the same manner as in classical Newtonian stars. Analogous to the Zeeman splitting in quantum mechanics the existence of a preferred direction in space (in our case the rotation axis of the compact object) leads to breaking of the degeneracy between counter- and corotating oscillations. Each nonrotating mode of index l is split into $2l+1$ different modes which in turn will affect their frequencies as well. Generally as seen from an inertial observer, frequencies of corotating modes will increase while those of counterrotating modes decrease with higher rotation rate. Additionally there is no clear distinction any longer between polar and axial perturbation; each 'polar' mode (i.e. polar in the limit of no rotation) is a sum of purely polar and axial terms and vice versa.

Another important effect of including rotation are rotational instabilities. While purely academic for ordinary stars they are extremely likely for compact objects like neutron stars. In the very simple case of a homogeneous Newtonian MacLaurin spheroid one can show analytically that a *dynamical instability* will set in once the ellipticity reaches a value of ~ 0.953 or equivalently at a ratio of rotational energy to gravitational energy $T/W \sim 0.27$ (see [1] for example). This instability will deform the star into a bar-like shape, therefore transforming it into a very good source of gravitational radiation. Fully relativistic simulations confirm this scenario with only a minor correction to T/W, see [19]. Another generic nonaxisymmetric instability in homogeneous relativistic bodies was found by Chandrasekhar [20] and later generalized to include all rotating, self-gravitating perfect fluids by Friedman and Schutz [21]; therefore called *CFS-instability*. It works with all dissipative mechanisms, so with gravitational waves as well as viscosity. Qualitatively, a mode which is seen retrograde in a coordinate system comoving with the rotating star carries negative angular momentum which is easy to see because the perturbed star apparently has less angular momentum than the unperturbed one. If the angular velocity of the star is high enough, this mode will be seen prograde for a distant observer in an inertial frame. It hence carries away positive angular momentum, decreasing the negative angular momentum of the mode even more. The critical value of T/W for the $l = m = 2$ fundamental polar mode on a polytropic background is roughly 0.14 and nearly independent of the polytropic index; see for example [22, 23]. This value for T/W already corresponds to angular velocities near the mass-shedding limit of a typical neutron star which limits the detection probability to a certain value. Most of todays known neutron stars do not come even close to this limit; the one with the fastest rotation rate (as of 2007) spins at about 1.1 kHz [24] which is only something like 30% of the Kepler limit for a typical neutron star and nearly all of the more than 700 discovered pulsars so far have rotation frequencies in the range $\sim 1 - 700$ Hz. From this point of view it would be nice to have an instability operating at very low rotation rate and indeed this is exactly what happens to r-modes in rotating neutron stars. These axial oscillations are unstable via the CFS-mechanism at all rotation rates which was first shown by Andersson [25] and Friedman, Morsink [26] for slowly rotating stars. Due to its generic nature, the r-mode instability was originally thought to be a very promising, persistent source of gravitational waves. But in the meantime more sophisticated and thorough studies which also included the influence of magnetic fields and bulk viscosity have turned the tide since both effects are able to prevent the growth of the instability. Still, r-modes may play an important role in limiting the spin of young neutron stars but further investigations are needed; more details specifically on r-modes can be found in [27] for example.

1.1.3 Gravitational Wave Asteroseismology

This richness in oscillation modes of relativistic stars may one day finally lead to what is generally called gravitational wave asteroseismology, i.e. similar to helioseismology in the case of the Sun to study internal properties of compact objects through the interpretation of their pulsations. Now all information that is collected from solar oscillations is based on the electromagnetic spectrum; the motion of hot gas is monitored by the Doppler shift in spectral lines of hydrogen. Seismology of compact object will rely on a type of radiation that is generated in a very different way. While electromagnetic radiation is produced incoherently by accelerated charged particles, the bulk motion of nonaxisymmetric matter distributions will lead to perturbations in the fabrics of spacetime that propagate with the speed of light; these are the gravitational waves.

This direct consequence of Einstein's Theory of General Relativity is one of the very few predictions that has not been directly verified yet. An indirect proof of their existence is the energy loss in compact binary systems, resulting in a decrease of separation between the two stars. This effects is being observed now for over 30 years in the pulsar system PSR1913+16 and the relative difference between theory and experiment are $\sim 10^{-3}$ [28, 29]; eventually Hulse and Taylor were awarded with the Nobel Prize in 1993 for its discovery. Still the first direct proof is missing and this is mostly due to the fact that gravitational radiation is extremely weak. Since matter couples very poorly to spacetime one needs enormous amounts of high density matter moving with very large velocities in order to produce a considerably amount of gravitational waves; these conditions are usually only met by neutron stars. And while electromagnetic waves are easily scattered and absorbed during their trip from source to detector, the perturbations of spacetime travel through the whole universe virtually unaffected. This leaves them in pristine condition, conserving the imprint of its generation. However, this rises the question how one would be able to detect those faint gravitational wave signals. General Relativity predicts that perturbations in spacetime will exert tidal forces on freely falling test particles which results in a periodic stretching and squeezing of its spatial separation in a plane perpendicular to the waves propagation direction. The strength of the wave is then usually quantified as relative change in the separation, i.e. $h = \Delta l/l$.

Historically the first attempts to use this feature for detector design were made by Weber in the 1960s. He constructed resonant bar detectors where piezoelectric sensors would monitor the deformation due to gravitational waves. Currently five such devices are in operation around the world (ALLEGRO, AURIGA, EXPLORER, NAUTILUS, NIOBE) with sensitivities of around 10^{-19} in a frequency band of $700 - 900$ Hz; this means that within that range a relative change in length of $h > 10^{-19}$ can be detected (see [30] for a general overview). There is yet another class of detectors which use laser interferometry to monitor the distance of test masses. Pretty much like the original Michelson-Morley experiment a change in the arm length of the interferometer induces a phase shift on the light that travels between these arms. When they interfere, this phase shift leads to an offset in the corresponding fringe pattern. Several of such detectors are operating worldwide (LIGO, VIRGO, GEO600, TAMA300) within a frequency range of about $10 - 1000$ Hz, limited by seismic noise in the low frequency regime and by photon shot noise for high frequencies. Their sensitivity is around 10^{-21} and further improvements for the second generation of interferometric detectors are on their way. Even a laser interferometer in outer space with armlengths of several million kilometers is planned (LISA) and first test missions are scheduled for the end of 2009.

With these advanced detectors it should finally be possible to verify a central prediction of general relativity directly and in the case of neutron stars this may lead to a whole bunch of possibilities for probing their internal structure. A first theoretical step in this direction has been done by Andersson and Kokkotas in 1996 [31]; see also [32]. There they computed frequencies and damping times for various oscillation modes and twelve different equations of state (EoS) and showed how the detection of corresponding gravitational wave signals can be used to accurately calculate the mass and the radius of the neutron star. From these measurements one will be able to actually deduce the correct form of the EoS at supernuclear densities; a problem that has not yet been solved due to the whole plethora of different theories in this extreme regime of nuclear physics. Of course there are several levels of sophistication; a lot of calculations are performed for nonrotating, perfect fluid stars. But we now that neutron stars can rotate rapidly (both uniform and differential), they have strong magnetic fields, most likely a solid crust followed by an intermediate superfluid region and maybe parts of exotic matter in the central regions. As we progress and include more and more of this realistic physics in our theoretical models of neutron star pulsations we will be able to extract even more information from this probably most extreme objects in the universe.

1.2 Methodology

This PhD-thesis will complement a series of projects at our Institute; all of them dealing with neutron star oscillations studied within certain approximations. As the full non-linear equations of general relativity are very difficult to solve there are several possibilities to simplify the initial setup of the problem. Linear perturbation theory by itself is already an approximation where one neglects all possible nonlinear influences; something which is justified and quite accurate as long as the perturbation of the time-independent equilibrium configuration is kept small. In the case of neutron star oscillations the equilibrium is given by a stationary (nonrotating or rotating) compact objects and the perturbations are given by small deviations of the velocity and pressure/density from their values in the stationary case. Even then one can simplify the problem considerably more. The most common approximations are

1. *The Cowling-approximation:* Already introduced by Cowling in 1941 for Newtonian stars, this approximation neglects the perturbation of the gravitational potential. Each change in pressure is connected to a corresponding change in density which then will alter the gravitational potential that enters the hydrodynamic equation of motion. Translated into general relativistic terms it means that one completely neglects the coupling of the matter perturbations to the spacetime. Since the metric of the stationary background is also time-independent, this means for example that one will not be able to generate gravitational waves within this approximation. The frequencies of p- and g-modes may slightly be different from their exact value, depending on their radial and angular behaviour, but one will never see w-modes.

2. *The slow-rotation approximation:* As already described earlier, rotation will lead to a deviation from the spherical symmetry of the star due to the centrifugal force. Since this is an $\mathcal{O}(\Omega^2)$-effect, it will become more dominant at higher rotation rates; for low angular velocities the shape of the compact object can still be considered as nearly spherical. In terms of general relativity again, rotation leads to an off-diagonal element in the line element that can be associated with the dragging of inertial frames in the direction of rotation. If this frame-dragging is small, so are deviations from spherical symmetry and nearly all mathematical and numerical tools originally developed for nonrotating stars can also be applied in this case. However, one won't get accurate results for rapidly rotating objects.

3. *The Inverse-Cowling–approximation:* Here, the perturbations of the fluid are completely neglected and only the metric perturbations are evolved; see [33] for example. Since most spacetime modes couple rather weakly to matter this is actually a quite good approximation if one only is interested in the various w-modes. Of course one won't see any fluid modes then.

There were already a couple of projects within the SFB/TR7 'Gravitational Wave Astronomy' founded in 2003 from active and former members of the theoretical astrophysics group in Tübingen which are shortly mentioned here. Kastaun wrote a general relativistic hydrodynamics code [34, 35, 36] and tested it successfully on neutron star oscillations in the Cowling approximation. Boutloukos used linear perturbation theory and the Cowling approximation to recast the oscillation equations into an eigenvalue problem with mode frequencies as eigenvalues and eigenfunctions as corresponding eigenvectors; see [37, 38]. Méndez worked in the slow-rotation approximation and linear theory to perform time-evolution of initial data and computed successfully mode frequencies and gravitational wave forms [39].

The work in this thesis can be described to be the time-evolution version of [37]. We will also use linear perturbation theory and the Cowling approximation but instead of assuming a harmonic time dependence in order to get rid of any temporal dependencies, the original linearized evolution equations have to be solved with various initial data. For obtaining mode frequencies and eigenfunctions, a spectral analysis has to be performed afterwards. It is also possible to excite only specific modes of oscillation with a method called *mode recycling* [40] which is also feasible with the code presented here. Since we are not working in the slow-rotation approximation where one neglects deviations from spherical symmetry, this is a two-dimensional problem to solve. It not only increases the computational costs but also requires a careful and proper treatment of the boundaries in order to be successful.
In the second chapter, the theoretical background of this work will be presented. We will shortly review the linear perturbation theory of the Einstein equations and introduce the Cowling approximation, which is one of several ways to simplify the problem. We then turn to the specific system of equations that are used here to study small oscillations on neutron stars, discuss some of their properties and derive the appropriate boundary conditions.
The third chapter deals with the numerical treatment of the time-evolution equations and will also describe some of the difficulties that arose during its implementation.
In the fourth chapter, we will present the obtained new results and compare it whenever possible with already published studies by other groups.
Appendix A will prove some of the statements that will be made in the second chapter about the properties of our system of partial differential equations.
In Appendix B follows a short description about the several computer programs used in this thesis; although the source code is supplied with many comments this will serve as some kind of official documentation.

1.3 Conventions

- We use the sum convention of Einstein. Latin indices denote spatial components and run from 1 to 3, greek indices denote spacetime components and run from 0 to 3 where the 0-component is the time component
- The signature of the metric is $(-,+,+,+)$; that is timelike vectors have negative norm.
- Unless otherwise stated, units are used in which $G = c = 1$.
- Covariant derivatives of an arbitrary quantity f with respect to x^μ are written as $D_\mu f$ or $f_{;\mu}$ and partial derivatives are abbreviated by $\partial_\mu f$ or $f_{,\mu}$.
- Scalar products like $g_{\mu\nu}u^\mu u^\nu$ sometimes are written as $\langle \mathbf{u}, \mathbf{u} \rangle$.
- We will assume a basic knowledge of General Relativity, see for example [41], [42].

2

The Perturbation Equations

In this chapter we will derive the time evolution equations for small perturbations on compact objects. The full nonlinear problem with the inclusion of all general-relativistic effects is very difficult to be treated so as a first step towards this ultimate goal we will study these perturbations under certain simplifying approximations. Nevertheless, we also want to present at least a slight glimpse of the whole picture and how well our assumptions fit in there.

2.1 The 3+1 Split in General Relativity

The field equations of General Relativity

$$G_{\mu\nu} = 8\pi\, T_{\mu\nu} \tag{2.1}$$

where $G_{\mu\nu}$ is the Einstein tensor and $T_{\mu\nu}$ represents the mass- and energy-content of the spacetime, in this particular form are not very well suited for a numerical implementation. They consist of 10 equations where 6 of them are dynamical equations of second order in time and 4 are constraint equations with no time derivatives at all. Following the work of Arnowitt, Deser and Misner (see [43]), we want to recast equations (2.1) into a Cauchy initial value problem of first order in time. For this we will need some prerequisites:

1. On a given a Riemannian manifold $\mathcal{M}$, we define a C^∞-function $f : \mathcal{M} \to \mathbb{R}$ that has the following properties
    - The differential $\mathrm{d}f$ of this function is defined everywhere on $\mathcal{M}$ and never vanishes there.
    - The surfaces $\mathcal{N}_t := \{x \in \mathcal{M} | f(x) = t\}$ are spacelike hypersurfaces.
2. There exists a timelike vector field $\boldsymbol{\xi}$ that also never vanishes and for which

$$\mathrm{d}f(\boldsymbol{\xi}) = 1$$

The rate of change of f along $\boldsymbol{\xi}$ therefore is constant which allows us to interpret f as a time coordinate when moving along the flow of $\boldsymbol{\xi}$. We therefore choose a coordinate system with $\partial_0 = \boldsymbol{\xi}$ and $\{\partial_1, \partial_2, \partial_3\}$ an arbitrary orthonormal coordinate system on $\mathcal{N}_t$.

Since the hypersurfaces $\mathcal{N}_t$ are defined by relations of the form $f = const$, the vector field orthonormal to that hypersurface is given by

$$\mathbf{n} = \frac{\nabla f}{||\nabla f||}$$

We now decompose the timelike vector field $\boldsymbol{\xi}$ into a component parallel to $\mathbf{n}$ and another one perpendicular to the orthonormal on $\mathcal{N}_t$,

$$\boldsymbol{\xi} = \alpha \mathbf{n} + \boldsymbol{\beta} \qquad \text{with} \qquad \langle \boldsymbol{\beta}, \mathbf{n} \rangle = 0$$

Here, the lapse-function α and the shift vector $\boldsymbol{\beta}$ have been introduced. The metric $g_{\mu\nu}$ of this spacetime foliation is given by the scalar product of its basis vectors $g_{\mu\nu} = \langle \partial_\mu, \partial_\nu \rangle$. More specifically, we have

$$\begin{aligned} g_{00} &= \langle \alpha \mathbf{n} + \boldsymbol{\beta}, \alpha \mathbf{n} + \boldsymbol{\beta} \rangle = -\alpha^2 + \beta_k \beta^k \\ g_{0i} &= \beta^i = g_{i0} \\ g_{ij} &= \gamma_{ij} \end{aligned}$$

where γ_{ij} is the 3-metric on the hypersurface $\mathcal{N}_t$. We arrive at the standard form of the metric in the ADM formalism

$$ds^2 = \gamma_{ij} \left(dx^i + \beta^i dt \right) \left(dx^j + \beta^j dt \right) - \alpha^2 dt^2 \,,$$

see also Figure 2.1 for the geometrical meaning of the $3+1$-variables.

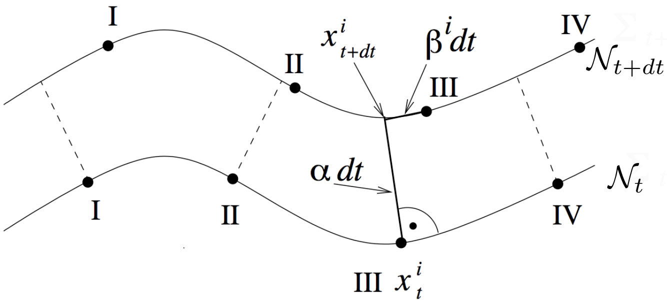

Figure 2.1: lapse function α and shift-vector $\boldsymbol{\beta}$ connecting two hypersurfaces; figure used with permission from [39]

The intrinsic geometry of the three-dimensional spacelike hypersurfaces is entirely determined by the 3-metric γ_{ij}. But there is still the freedom on how these hypersurfaces are embedded in the full four-dimensional spacetime, so we will need another quantity, the extrinsic curvature, that determines exactly this embedding. If we have two vector fields $\mathbf{X}$ and $\mathbf{Y}$ on $\mathcal{N}_t$, the extrinsic curvature is defined as

$$\mathbf{K}(\mathbf{X}, \mathbf{Y}) := \langle D_{\mathbf{X}} \mathbf{n}, \mathbf{Y} \rangle$$

The Einstein equations (2.1) can then be split according to

$$\begin{aligned}
\mathbf{G}(\mathbf{n},\mathbf{n}) &= 8\pi\,\mathbf{T}(\mathbf{n},\mathbf{n})\\
\mathbf{G}(\mathbf{n},\mathbf{X}) &= 8\pi\,\mathbf{T}(\mathbf{n},\mathbf{X})\\
\mathbf{G}(\mathbf{X},\mathbf{Y}) &= 8\pi\,\mathbf{T}(\mathbf{X},\mathbf{Y})
\end{aligned}$$

The first two equations are time independent and represent constraint equations that have to be fulfilled at any hypersurface. Once satisfied on the initial hypersurface, the Bianchi identities ensure that they will be satisfied throughout the evolution (of course only analytically and in general not numerically). They can be written as

$$S^N - K_{ij}K^{ij} + K^2 = 16\pi\,T_{\mu\nu}n^\mu n^\nu \qquad \text{(Hamiltonian Constraint)} \tag{2.2}$$

$$D_iK - D_jK^j_i = 8\pi\,T_{\mu i}n^\mu \qquad \text{(Momentum Constraint)} \tag{2.3}$$

where S^N is the scalar curvature on the hypersurface and $K = \gamma_{ij}K^{ij}$.

The constraint equations are complemented by the actual dynamical evolution equations which describe how 3-metric and extrinsic curvature change when going from one hypersurface $\mathcal{N}_t$ to another one $\mathcal{N}_{t+dt}$.

$$\partial_t\gamma_{ij} = -2\alpha K_{ij} + \partial_k\gamma_{ij}\beta^k + \gamma_{ki}\partial_j\beta^k + \gamma_{kj}\partial_i\beta^k \tag{2.4}$$

$$\begin{aligned}
\partial_t K_{ij} = {}& \alpha\left[R^N_{ij} + KK_{ij} - 2K_{ik}K^k_j - 8\pi\left(T_{ij} - \frac{1}{2}T\gamma_{ij}\right)\right]\\
&-D_iD_j\alpha + \partial_k K_{ij}\beta^k + K_{ik}\partial_j\beta^k + K_{jk}\partial_i\beta^k
\end{aligned} \tag{2.5}$$

where R^N_{ij} is the Ricci-tensor on $\mathcal{N}_t$ and $T = \gamma_{ij}T^{ij}$. This is the final first-order evolution system for the geometric variables γ_{ij} and K_{ij} in the ADM formalism. They are updated according to equations (2.4) and (2.5). But the matter variables which appear there have to be updated as well and this is done by the conservation law of energy-momentum

$$D_\mu T^\mu_\nu = 0 \tag{2.6}$$

which consists of four first-order equations for the independent variables in $T^{\mu\nu}$.

The system of equations (2.2) - (2.6) is still very difficult to numerically evolve in time. In some cases it is possible to study the evolution of this system as small perturbations on a stationary background. In this thesis we want to look at oscillations of neutron stars and as long as these oscillations remain finite and small we can neglect the nonlinear characteristics of the original Einstein equations and work within linear perturbation theory. Of course this decomposition is not always possible; if one wants to study for example the merger of binary neutron stars, one cannot separate the problem into a stationary part and small perturbations on this stationary background. In this case one has to deal with the original system (2.2) - (2.6).

In the next sections we will introduce the notions of linear perturbation theory and we will see how the Cowling approximation simplifies our problem even more.

2.2 Linear Perturbation Theory

We want to perturb the Einstein equations in their ADM form; this means that we will add "small" auxiliary contributions to our variables and write them as

$$\begin{array}{rcllr} \bar{\gamma}_{ij} & = & \gamma_{ij} + h_{ij} & \text{with} \quad |h_{ij}| \ll |\gamma_{ij}| & (2.7) \\ \bar{K}_{ij} & = & K_{ij} + k_{ij} & \text{with} \quad |k_{ij}| \ll | K_{ij}| & \\ \bar{\beta}_i & = & \beta_i + \delta\beta_i & \text{with} \quad |\delta\beta_i| \ll | \beta_i| & \\ \bar{\alpha} & = & \alpha + \delta\alpha & \text{with} \quad |\delta\alpha| \ll | \alpha| \, , & \\ & & & & (2.8) \end{array}$$

and all other quantities accordingly. With this approach we substitute into the system of equations (2.2) - (2.6) and include only the terms that are of linear order on the perturbation variables; higher order terms are discarded. We will end up with a linear system of equations which is valid for small deviations from equilibrium.

First, we agree to raise and lower the indices of our perturbations with the unperturbed 3-metric, so we have for example

$$\delta\beta^i = \gamma^{ij}\beta_j \qquad \text{and} \qquad \delta\beta_i = \gamma_{ij}\delta\beta^j$$

It follows directly, that we have

$$\bar{\gamma}^{ij} = \gamma^{ij} - h^{ij}$$

because only with this choice it is $\bar{\gamma}^{ij}\bar{\gamma}_{jk} = \delta^i_k$ in linear approximation. This also means that the components h_{ij} cannot be components of a tensor. Also lowering and raising indices becomes more complicated. The covariant components of the shift vector $\bar{\boldsymbol{\beta}}$ are for example given by

$$\begin{aligned} \bar{\beta}^i &= \bar{\gamma}^{ij}\bar{\beta}_j = \left(\gamma^{ij} - h^{ij}\right)\left(\beta_j + \delta\beta_j\right) \\ &= \beta^i + \delta\beta^i - h_{ij}\beta_j \end{aligned}$$

We will also need the perturbed Christoffel symbols in linear order. It is

$$\bar{\Gamma}^k_{ij} = \Gamma^k_{ij} + \delta\Gamma^k_{ij} = \frac{1}{2}\bar{\gamma}^{km}(\bar{\gamma}_{mj,i} + \bar{\gamma}_{mi,j} - \bar{\gamma}_{ij,m})$$

and this leads to

$$\delta\Gamma^k_{ij} = \frac{1}{2}\gamma^{km}(h_{mj,i} + h_{mi,j} - h_{ij,m} - 2\Gamma^l_{ij}h_{lm}) \tag{2.9}$$

Similarly the perturbed Ricci-Tensor on the hypersurface is given by

$$\delta R_{ij} = \delta\Gamma^k_{ij,k} - \delta\Gamma^k_{ik,j} + \Gamma^l_{ij}\delta\Gamma^k_{lk} + \Gamma^k_{lk}\delta\Gamma^l_{ij} - \Gamma^l_{ik}\delta\Gamma^k_{lj} - \Gamma^k_{lj}\delta\Gamma^l_{ik} \tag{2.10}$$

We now can perturb the ADM equations. As one can see already from the preparatory work we have done until now, although we will arrive at linear equations for the perturbation variables, these equations tend to become quite long.

The evolution equation for the 3-metric in its perturbed form is

$$\partial_t\bar{\gamma}_{ij} = -2\bar{\alpha}\bar{K}_{ij} + \partial_k\bar{\gamma}_{ij}\bar{\beta}^k + \bar{\gamma}_{ki}\partial_j\bar{\beta}^k + \bar{\gamma}_{kj}\partial_i\bar{\beta}^k$$

We insert (2.7) and find

$$\begin{aligned}\partial_t h_{ij} \quad = \quad & -2\alpha k_{ij} + \partial_k \gamma_{ij} \delta\beta^k + \gamma_{ki}\partial_j \delta\beta^k + \gamma_{kj}\partial_i \delta\beta^k - 2\delta\alpha K_{ij} - \partial_k \gamma_{ij} h^{kr}\beta_r \\ & -\gamma_{ki}\partial_j \left(h^{kr}\beta_r\right) - \gamma_{kj}\partial_i \left(h^{kr}\beta_r\right) + \partial_k h_{ij}\beta^k + h_{ki}\partial_j \beta^k + h_{kj}\partial_i \beta^k\end{aligned}$$

Luckily, at least this expression can be simplified and after some lengthy calculation one arrives at

$$\partial_t h_{ij} = \partial_i \delta\beta_j + \partial_j \delta\beta_i - 2\left(\alpha k_{ij} + \delta\alpha K_{ij} + \Gamma^k_{ij}\delta\beta_k + \delta\Gamma^k_{ij}\beta_k\right) \tag{2.11}$$

Unfortunately, the evolution equation for the perturbed extrinsic curvature cannot be brought into a similar short form. A straightforward calculation leads to

$$\begin{aligned}\partial_t k_{ij} \quad = \quad & \partial_k K_{ij}\delta\beta^k - h^{kl}\partial_k K_{ij}\beta_l + \partial_k k_{ij}\beta^k + K_{ik}\partial_j \delta\beta^k - h^{kl}K_{ik}\partial_j\beta_l \\ & +k_{ik}\partial_j\beta^k + K_{jk}\partial_i\delta\beta^k - h^{kl}K_{jk}\partial_i\beta_l + k_{jk}\partial_i\beta^k - \partial_i\partial_j\delta\alpha + \Gamma^l_{ij}\partial_l\delta\alpha \\ & +\delta\Gamma^l_{ij}\partial_l\alpha + \alpha\left(\delta R_{ij} + K k_{ij} + k K_{ij} - h^{rs}K_{rs}K_{ij} - 2k^k_j K_{ik}\right. \\ & \left. +2h^{kl}K_{lj}K_{ik} - 2K^k_j k_{ik} + 8\pi\left(\delta T_{ij} - 1/2\left(T\,h_{ij} + t\gamma_{ij} - h^{rs}T_{rs}\gamma_{ij}\right)\right)\right) \\ & +\delta\alpha\left(R_{ij} + KK_{ij} - 2K^k_j K_{ik} + 8\pi\left(T_{ij} - 1/2\,T\gamma_{ij}\right)\right)\end{aligned} \tag{2.12}$$

where δT_{ij} is the perturbation of the energy-momentum–tensor and furthermore $t = \gamma_{ij}\delta T^{ij}$ and $k = \gamma_{ij}k^{ij}$. The constraint equations also need to be linearized but we will skip it here since we will not need it in this work. As already mentioned earlier, one now has linear evolution equations which, in their general form (2.11) and (2.12), have a quite complicated form. They can be simplified once a specific background metric and energy-momentum–tensor has been chosen. For example in the case of a nonrotating neutron star described by a perfect fluid both γ_{ij} and T_{ij} are diagonal, so many terms in (2.11) and (2.12) are vanishing identically. Additionally, the gauge freedom in General Relativity allows also to set several components of h_{ij} and k_{ij} to zero, depending on the specific gauge one chooses. Still, the resulting equations are very difficult to solve.

We derived the linearized evolution equations for the geometric quantities, now we have to do the same for the matter variables. For this we will rewrite the unperturbed version of (2.6) to

$$D_\mu T^\mu_\nu = D_\mu(g^{\mu\kappa}T_{\kappa\nu}) = g^{\mu\kappa}D_\mu T_{\kappa\nu} = 0$$

The perturbed version of this relationship is therefore

$$\begin{aligned}\bar{D}_\mu \bar{T}^\mu_\nu \quad = \quad & (g^{\mu\kappa} - h^{\mu\kappa})((T_{\kappa\nu} + \delta T_{\kappa\nu})_{,\mu} - (\Gamma^\lambda_{\kappa\mu} + \delta\Gamma^\lambda_{\kappa\mu})(T_{\lambda\nu} + \delta T_{\lambda\nu}) \\ & -(\Gamma^\lambda_{\nu\mu} + \delta\Gamma^\lambda_{\nu\mu})(T_{\kappa\lambda} + \delta T_{\kappa\lambda})) = 0\end{aligned}$$

The now well-known procedure of neglecting all terms higher than first order finally leads to

$$\begin{aligned}& g^{\mu\kappa}(\delta T_{\kappa\nu,\mu} - \Gamma^\lambda_{\kappa\mu}\delta T_{\lambda\nu} - \Gamma^\lambda_{\mu\nu}\delta T_{\kappa\lambda} - \delta\Gamma^\lambda_{\kappa\mu}T_{\lambda\nu} - \delta\Gamma^\lambda_{\mu\nu}T_{\kappa\lambda}) \\ & -h^{\mu\kappa}(T_{\kappa\nu,\mu} - \Gamma^\lambda_{\kappa\mu}T_{\lambda\nu} - \Gamma^\lambda_{\mu\nu}T_{\kappa\lambda}) = 0\end{aligned} \tag{2.13}$$

In linear perturbation theory one thus has to solve equations (2.11), (2.12) and (2.13) in an appropriate gauge and preserve the two additional constraints for energy-density and

momentum on every hypersurface $\mathcal{N}_t$.
In the ADM-formalism, the gauge freedom is provided by the lapse-function α and the shift-vector $\boldsymbol{\beta}$, i.e. since the Einstein equations are covariant it is up to us to find the most convenient way of foliating spacetime (see Figure 2.1) so that the problem we want to study takes the simplest form. On the other hand, making a bad choice for α and $\boldsymbol{\beta}$ will easily lead to instabilities which are related to the poor choice of the coordinates on the various hypersurfaces. Depending on the specific problem setup, i.e. radial or nonradial perturbations in the case of neutron star oscillations, one can use this gauge freedom either to set lapse and shift directly to zero or to impose certain conditions on them which remove particular problematic terms in the equations, see [44] for an application to nonrotating stars.

2.3 The Cowling Approximation

This approximation was introduced by Cowling (see [4]), following Emden [45] and Rosseland [46] during the study of oscillating polytropic stars and there the variations of the gravitational potential were neglected. The justification for this approach was, that if the mass of the stellar model is concentrated towards the center then density variations will not produce large variations of the gravitational potential in the outer regions of the star which have a large influence on the mode frequencies. It is also a good approximation for high order modes since positive and negative density variations cancel out the perturbation of the gravitational potential. In addition it reduces the number of equations one has to deal with in Newtonian theory (this was the original reason for its introduction) and even more in General Relativity. In fact if we look at the perturbed Poisson equation for the gravitational potential

$$\nabla^2 \delta\Phi = 4\,\pi G \delta\rho$$

and decompose the perturbations according to

$$\delta\rho(r,\theta,\varphi,t) = \sqrt{4\pi}\tilde{\rho}(r) Y^l_m(\theta,\varphi) e^{-i\omega t} \quad \text{and} \quad \delta\Phi(r,\theta,\varphi,t) = \sqrt{4\pi}\tilde{\Phi}(r) Y^l_m(\theta,\varphi) e^{-i\omega t}$$

this will lead to

$$\frac{1}{r^2}\frac{d}{dr}\left(r^2 \frac{d\tilde{\Phi}}{dr}\right) - \frac{l(l+1)}{r^2}\tilde{\Phi} = 4\,\pi G \tilde{\rho}$$

The solution to this equation is given by

$$\tilde{\Phi}(r) = \frac{-4\pi G}{2l+1}\left[\frac{1}{r^{l+1}}\int_0^r \tilde{\rho}(r') r'^{l+2} dr' + r^l \int_r^R \frac{\tilde{\rho}(r')}{r'^{l-1}} dr'\right] \tag{2.14}$$

From equation (2.14) one can deduce that $|\tilde{\Phi}|$ is small compared to $|\tilde{\rho}|$ if either l is large or the radial order n is large since then $\tilde{\Phi}$ is a sum of integrals over rapidly varying functions which reduce the absolute value of the perturbed potential.
The validity of the relativistic Cowling approximation first introduced by McDermott (see [47]) depends very strong on the specific family of modes under study. As it has been shown in [48], many of the conclusions from the Newtonian Cowling approximation are also valid

in its relativistic counterpart. We therefore expect good agreement with a fully relativistic treatment in the case of large radial node numbers and high l-values of the spherical decomposition as it has been shown in [49], [50]. The errors are around 10% for low mode numbers and decrease monotonically for higher modes. Also g-modes can be computed very accurately within this approximation. Since r-modes are mainly perturbations of the azimuthal fluid-velocity, we also expect the Cowling approximation to provide valid results there. On the other hand as it has been shown in [51] and [52], the frequencies for the fundamental mode and their first overtones obtained by a full-relativistic treatment differ very strong from their counterparts when neglecting the metric perturbations.

Let us now examine what the Cowling approximation means to the ADM form of the linearized Einstein equations. Since the spacetime geometry described by the background metric in this case doesn't change in time, we neither have to deal with the evolution equations for 3-metric and extrinsic curvature nor the constraint equations on every hypersurface. Only the four equations governing the motion of the fluid (i.e. (2.13)) remain and in fact become even shorter because we can set $\delta\Gamma^{\lambda}_{\kappa\mu} = h^{\mu\kappa} = 0$ there. This leads to the final system to solve in this thesis.

$$g^{\mu\kappa}(\partial_\mu \delta T_{\kappa\nu} - \Gamma^{\lambda}_{\kappa\mu}\delta T_{\lambda\nu} - \Gamma^{\lambda}_{\mu\nu}\delta T_{\kappa\lambda}) = 0 \tag{2.15}$$

As one can see, the relativistic Cowling approximation has greatly reduced the number of equations to solve. Instead of dealing with a complicated set of hyperbolic differential equations and elliptic constraints, four fluid evolution equations need to be considered. Of course, we will not have any emission of gravitational waves in a self-consistent way, so energy and momentum conservation is no longer fulfilled here but as pointed out earlier the various mode characteristics will still be apparent. Of course one can still make a rough ad-hoc estimate about the amount of gravitational radiation emitted via the quadrupole formula but keep in mind that this is not a direct consequence of the dynamical evolution equations in the Cowling approximation.

For a numerical integration of equations (2.15), we need to specify a coordinate system in which we have to write down the metric and we have to choose the energy-momentum–tensor for our problem. Both will be discussed in the following section.

2.4 The Metric and the Energy-Momentum–Tensor

In the simplest case of a nonrotating spherical object in a spherical coordinate system (r, θ, ϕ), the line-element takes the form

$$ds^2 = e^{2\lambda(r)}dr^2 + r^2\left(d\theta^2 + r^2\sin^2\theta d\phi^2\right) - e^{2\nu(r)}dt^2$$

with the two unknown metric potentials $\lambda(r)$ and $\nu(r)$. For the energy-momentum–tensor we will neglect the effects of non-isotropic stresses, viscosity and heat conduction and use the perfect fluid representation

$$T_{\mu\nu} = (\epsilon + p)u_\mu u_\nu + p g_{\mu\nu} \tag{2.16}$$

Here ϵ and p are the energy density and the pressure and u_μ is the already familiar 4-velocity of the object, which in the nonrotating case only has a nonvanishing 0-component $u^0 = e^{-\nu}$.

When put into the Einstein equations this leads to the well-known TOV-equations

$$\begin{aligned}\partial_r \lambda &= \frac{1-e^{2\lambda}}{r} + 4\pi r e^{2\lambda}\epsilon \\ \partial_r \nu &= \frac{e^{2\lambda}-1}{2r} + 4\pi r e^{2\lambda} p \\ \partial_r p &= -\partial_r \nu (\epsilon + p)\end{aligned}$$

These are three equations for the four unknowns ν, μ, ϵ and p. The last relationship needed to make this problem well-posed is the Equation of State (EoS), which we will assume to be of barotropic form, i.e. the pressure depends only on the energy density $p = p(\epsilon)$ and not on additional thermodynamical variables like entropy or temperature etc. The simplest barotropic equation of state is a polytropic one and has the form

$$\begin{aligned}p &= K\rho^{1+1/N} \qquad (2.17)\\ \epsilon &= \rho + Np\end{aligned}$$

where ρ is the rest-mass density, K is the polytropic constant used for normalization and N is the polytropic index that determines whether a specific EoS is considered as soft (this means that in equilibrium gravity can compress the matter to small radii) or stiff (the pressure balances gravity already at large radii). The TOV-equations then are solved from the center of the star to the point where the pressure vanishes and this point defines the stellar radius.

A more difficult problem is the accurate numerical determination of rotating equilibrium configurations. With the same premises as above the metric now reads

$$ds^2 = -e^{2\nu}dt^2 + e^{2\psi}(d\phi - \omega dt)^2 + e^{2\mu}(dr^2 + r^2 d\theta^2) \qquad (2.18)$$

where we have an off-diagonal ϕt-component which is responsible for the dragging of inertial frames in the direction of rotation and all four unknown metric functions ν, ψ, ω and μ now depend on r and θ. Following Bardeen and Wagoner (see [53]) one writes

$$e^{\psi} = r \sin\theta B e^{-\nu}$$

and solves for B, ν, ω and μ. When writing down the field equations for this problem one has to take into account that the 4-velocity now has a nonvanishing ϕ-component. With the angular velocity Ω of the stellar object defined as

$$\Omega = \frac{u^\phi}{u^t}$$

and the additional normalization condition $\langle \mathbf{u}, \mathbf{u} \rangle = -1$, one gets

$$u^t = \frac{e^{-\nu}}{\sqrt{1-v^2}} \qquad \text{with} \qquad v = (\Omega - \omega)e^{\psi - \nu}$$

As one can see, going from a nonrotating to a rotating equilibrium configuration means to solve a more difficult system of equations in two dimensions. A successful numerical integration was obtained in [54] and an independent code was presented in [55] which was made

publicly available (see [56]).
In this thesis we will obtain the background metric from yet another implementation developed within the Transregio SFB/TR 7 "Gravitational Wave Astronomy" (see [57] for a detailed description) and this metric differs in one crucial point from the line elements discussed earlier. It is written in a cylindrical coordinate system (ρ, ζ, ϕ) and is split up into two parts; the interior of the object and the spacetime exterior to it. Since in the Cowling approximation we are neglecting the evolution of spacetime, we only have to consider the interior of the star. There the coordinate system is rotating with the fluid and the metric takes the form

$$ds^2 = e^{-2U}\left[e^{2k}\left(d\rho^2 + d\zeta^2\right) + W^2 d\varphi^2\right] - e^{2U}(dt + a d\varphi)^2 \tag{2.19}$$

where the unknown functions U, k, W and a depend on ρ and ζ. The potentials W and a have to fulfill certain asymptotic conditions; in particular we have

$$\begin{aligned} \lim_{\rho\to 0} |a\rho^{-2}| &< \infty \\ \lim_{\rho\to 0} |W\rho^{-1}| &< \infty \end{aligned} \tag{2.20}$$

which will become important later in Chapter 3 when discussing the stability properties of our evolution scheme.
One important point here is, that in this coordinate system at any rotation rate, the 4-velocity still has only one single nonvanishing component, i.e. $u^t = e^{-U}$ and this simplifies the linearized perturbation equations considerably as we will see in the next section. The angular velocity Ω in this description of a compact objects' spacetime is determined by matching the interior solution to the exterior one which is formulated in a coordinate system at rest. Proper boundary conditions have to be applied at the surface of the star and they determine the angular velocity; see [57] for details.

2.5 Derivation of the Linearized Perturbation Equations

For equations (2.15) we will need the perturbation of the energy-momentum–tensor. Linearizing (2.16) then leads to

$$\delta T_{\mu\nu} = (\epsilon + p)(u_\mu \delta u_\nu + u_\nu \delta u_\mu) + (\delta p + \delta\epsilon) u_\mu u_\nu + \delta p g_{\mu\nu} \tag{2.21}$$

Here we also introduced the perturbations of the 4-velocity δu_μ. These are not four independent quantities because $\langle \mathbf{u} + \delta\mathbf{u}, \mathbf{u} + \delta\mathbf{u}\rangle = -1$ and this leads to $\delta u_t = 0$ in our comoving coordinate system.
Also, as mentioned earlier, pressure and density are connected by an equation of state, which we will use to express the pressure perturbation as function of $\delta\epsilon$. Since the speed of sound is given by

$$c_s^2 = \frac{\partial p}{\partial \epsilon} \qquad \text{we have} \qquad \delta p = c_s^2 \delta\epsilon \tag{2.22}$$

For polytropic equations of state (2.17) it is (with $\Gamma = 1 + 1/N$ the polytropic exponent)

$$\epsilon = \left(\frac{p}{K}\right)^{1/\Gamma} + Np \tag{2.23}$$

so this means that

$$\frac{\partial \epsilon}{\partial p} = \frac{1}{\Gamma}\left(\frac{p}{K}\right)^{1/\Gamma - 1} \cdot \frac{1}{K} + N \tag{2.24}$$

Extending both sides of this equation with p/p followed by inversion of (2.24) finally leads to

$$c_s^2 = \frac{\Gamma p}{\epsilon + p} \tag{2.25}$$

2.5.1 The Equations

Equations (2.15) will then lead to four linear equations for our four independent perturbation variables δu_ρ, δu_ζ, δu_ϕ and $\delta\epsilon$ as function of ρ, ζ, ϕ and time t. It is common in the nonrotating case and even in the slow-rotation approximation, where one neglects the centrifugal deformation of the star, to decompose the angular part in spherical harmonics (for example [58], [59]). At least for rapid rotation this is not longer convenient since a highly flattened star obviously has lost its spherical symmetry. Instead we will only separate the azimuthal part in periodic functions. We write

$$\begin{aligned}
\delta u_\rho &= f_1(\rho,\zeta,t)e^{im\varphi} && (2.26)\\
\delta u_\zeta &= f_2(\rho,\zeta,t)e^{im\varphi} && (2.27)\\
\delta u_\varphi &= f_3(\rho,\zeta,t)e^{im\varphi} && (2.28)\\
\delta\epsilon &= H(\rho,\zeta,t)e^{im\varphi} && (2.29)
\end{aligned}$$

We will then get a system of complex partial differential equations and since our system is linear the real part will be the final solution of a given initial value problem.
When we put equations (2.26)-(2.29) straight into system (2.15), we end up with the follow-

ing set of equations

$$\frac{\partial f_1}{\partial t} = -\frac{c_s^2}{(\epsilon+p)} e^U \frac{\partial H}{\partial \rho} - \frac{e^U}{(\epsilon+p)} \left[(1+c_s^2) \frac{\partial U}{\partial \rho} + \frac{\partial c_s^2}{\partial \rho} \right] H - \frac{e^{4U}}{W^2} \frac{\partial a}{\partial \rho} f_3 \tag{2.30}$$

$$\frac{\partial f_2}{\partial t} = -\frac{c_s^2}{(\epsilon+p)} e^U \frac{\partial H}{\partial \zeta} - \frac{e^U}{(\epsilon+p)} \left[(1+c_s^2) \frac{\partial U}{\partial \zeta} + \frac{\partial c_s^2}{\partial \zeta} \right] H - \frac{e^{4U}}{W^2} \frac{\partial a}{\partial \zeta} f_3 \tag{2.31}$$

$$\begin{aligned}
\frac{\partial f_3}{\partial t} = {} & \frac{im}{F} \left(a c_s^2 e^{4U} f_3 + \frac{W^2 c_s^2 e^U}{(\epsilon+p)} H \right) + \frac{W^2 a c_s^2 e^{4U-2k}}{F} \left(\frac{\partial f_1}{\partial \rho} + \frac{\partial f_2}{\partial \zeta} \right) \\
& + \frac{W e^{4U-2k}}{F(\epsilon+p)} \left[a c_s^2 (\epsilon+p) \frac{\partial W}{\partial \rho} + W a c_s^2 (\epsilon+p) \frac{\partial U}{\partial \rho} \right. \\
& \left. + W a c_s^2 \frac{\partial}{\partial \rho}(\epsilon+p) - W(\epsilon+p) \frac{\partial a}{\partial \rho} \right] f_1 \\
& + \frac{W e^{4U-2k}}{F(\epsilon+p)} \left[a c_s^2 (\epsilon+p) \frac{\partial W}{\partial \zeta} + W a c_s^2 (\epsilon+p) \frac{\partial U}{\partial \zeta} \right. \\
& \left. + W a c_s^2 \frac{\partial}{\partial \zeta}(\epsilon+p) - W(\epsilon+p) \frac{\partial a}{\partial \zeta} \right] f_2
\end{aligned} \tag{2.32}$$

$$\begin{aligned}
\frac{\partial H}{\partial t} = {} & \frac{im}{F} (a c_s^2 e^{4U} H + (\epsilon+p) e^{3U} f_3) + \frac{W^2 (\epsilon+p)}{F} e^{3U-2k} \left(\frac{\partial f_1}{\partial \rho} + \frac{\partial f_2}{\partial \zeta} \right) \\
& + \frac{e^{5U-2k}}{F} \left[W^2 e^{-2U} \frac{\partial}{\partial \rho}(\epsilon+p) + W^2 (\epsilon+p) e^{-2U} \frac{\partial U}{\partial \rho} \right. \\
& \left. - a(\epsilon+p) e^{2U} \frac{\partial a}{\partial \rho} + W(\epsilon+p) e^{-2U} \frac{\partial W}{\partial \rho} \right] f_1 \\
& + \frac{e^{5U-2k}}{F} \left[W^2 e^{-2U} \frac{\partial}{\partial \zeta}(\epsilon+p) + W^2 (\epsilon+p) e^{-2U} \frac{\partial U}{\partial \zeta} \right. \\
& \left. - a(\epsilon+p) e^{2U} \frac{\partial a}{\partial \zeta} + W(\epsilon+p) e^{-2U} \frac{\partial W}{\partial \zeta} \right] f_2
\end{aligned} \tag{2.33}$$

where

$$F := a^2 c_s^2 e^{4U} - W^2 \tag{2.34}$$

At a first glance, this system looks rather complicated but in fact can be simplified quite a lot as we will see soon. As one can see, there a no terms proportional to the angular velocity Ω since we are working in a comoving reference frame; the very same equations for a metric of the form (2.18) would be even longer.
We now make the substitution

$$\tilde{f}_1 = (\epsilon+p) W e^U f_1 \tag{2.35}$$

$$\tilde{f}_2 = (\epsilon+p) W e^U f_2 \tag{2.36}$$

$$\tilde{f}_3 = (\epsilon+p) f_3 \tag{2.37}$$

$$\tilde{H} = c_s^2 e^U H \tag{2.38}$$

and arrive at our final system of equations for the time-evolution (we are omitting the tilde here)

$$\begin{aligned}
\frac{\partial f_1}{\partial t} &= -We^U\frac{\partial H}{\partial \rho} - \frac{e^{5U}}{W}\frac{\partial a}{\partial \rho}f_3 - \frac{W}{c_s^2}\frac{\partial U}{\partial \rho}e^U H && (2.39)\\
\frac{\partial f_2}{\partial t} &= -We^U\frac{\partial H}{\partial \zeta} - \frac{e^{5U}}{W}\frac{\partial a}{\partial \zeta}f_3 - \frac{W}{c_s^2}\frac{\partial U}{\partial \zeta}e^U H && (2.40)\\
\frac{\partial f_3}{\partial t} &= \frac{im}{F}\left(ac_s^2e^{4U}f_3 + W^2H\right) + \frac{Wac_s^2e^{3U-2k}}{F}\left(\frac{\partial f_1}{\partial \rho} + \frac{\partial f_2}{\partial \zeta}\right) && (2.41)\\
&\quad -\frac{e^{3U-2k}}{F}W\frac{\partial a}{\partial \rho}f_1 - \frac{e^{3U-2k}}{F}W\frac{\partial a}{\partial \zeta}f_2\\
\frac{\partial H}{\partial t} &= \frac{im}{F}\left(ac_s^2e^{4U}H + c_s^2e^{4U}f_3\right) + \frac{Wc_s^2e^{3U-2k}}{F}\left(\frac{\partial f_1}{\partial \rho} + \frac{\partial f_2}{\partial \zeta}\right) && (2.42)\\
&\quad -\frac{c_s^2e^{7U-2k}}{F}\frac{a}{W}\frac{\partial a}{\partial \rho}f_1 - \frac{c_s^2e^{7U-2k}}{F}\frac{a}{W}\frac{\partial a}{\partial \zeta}f_2
\end{aligned}$$

In fact, it is possible to simplify this already quite short system even more by combining f_3 and H into a new function. Then the last two equations (2.41), (2.42) can be written as

$$\begin{aligned}
W\frac{\partial f_3}{\partial t} - Wa\frac{\partial H}{\partial t} &= -imWH + e^{3U-2k}\left(\frac{\partial a}{\partial \rho}f_1 + \frac{\partial a}{\partial \zeta}f_2\right)\\
a\frac{\partial f_3}{\partial t} - \frac{W^2}{c_s^2e^{4U}}\frac{\partial H}{\partial t} &= imf_3 + We^{-U-2k}\left(\frac{\partial f_1}{\partial \rho} + \frac{\partial f_2}{\partial \zeta}\right)
\end{aligned}$$

There are no singular terms on the righthand side now but of course two additional functions have been defined on the lefthand sides. From a numerical point of view at each timestep one would have to invert

$$\begin{aligned}
A &:= Wf_3 - WaH && (2.43)\\
B &:= af_3 - \frac{W^2}{c_s^2e^{4U}}H
\end{aligned}$$

to obtain values f_3 and H for the next consecutive timestep. The inversion would introduce new singularities at least along the rotational axis $\rho = 0$, so although equations (2.41) and (2.42) can be recast into a very short form, we will use the original system (2.39)-(2.42) for time evolution. One still can think about trying out whether a new scheme based on the application of (2.43) can be implemented successfully. However, this was not a part of this thesis.

2.5.2 Some Properties of the Equations

The system (2.39)-(2.42) possesses a couple of interesting properties we will discuss here. Some of these features can be used to check the numerical implementation of our time evolution scheme as well as help us to understand and interpret our results. The proofs of the more mathematical statements in this subsection are postponed and discussed in appendix A.

- The complete set of four equations can roughly be separated into two groups with similar characteristics. The first group (2.39), (2.40) consists of the first two equations governing the temporal evolution of δu_ρ and δu_ζ. The second group (2.41)-(2.42) is made out of the remaining equations describing the behaviour of δu_φ and $\delta\epsilon$.

- Instead of being dependent on all four perturbation variables (and their derivatives), the first group only depends on the same set of two perturbation quantities and their derivatives, that is δu_φ and $\delta\epsilon$. Additionally, no derivatives with respect to φ show up there.

- The structure of the equations in the first group is nearly identical; one only has to replace all ρ-derivatives with ζ-derivatives. Due to the lack of any φ-derivative the first group forms a purely real system of partial differential equations.

- The equations in the second group are the only ones that depend explicitly on the m-value of the azimuthal decomposition; that means that we have φ-derivatives there. This also transforms the full set of four equations into a complex-valued system; starting with purely real initial data the equations in the second group will mix real and imaginary parts, leading to nonzero imaginary parts as well.

- Still, in the axisymmetric case (i.e. $m = 0$) the system is purely real since the derivatives with respect to φ have no effect then. In this case purely real initial data will not get mixed and the imaginary parts of all four perturbation variables will stay zero (granted that they were zero initially). If additionally the star is non-rotating then the metric potential a will also vanish since the line element is diagonal in this case. Then the evolution equation for δu_φ is identically zero as well, i.e. we have $\partial_t f_3 \equiv 0$ for $\Omega = 0$ and $m = 0$.

- Let us denote a complex valued solution of (2.39)-(2.42) to a given m-value m_0 with

  $$s_1 = (f_1^{real}, f_1^{im}, f_2^{real}, f_2^{im}, f_3^{real}, f_3^{im}, H^{real}, H^{im})_{m=m_0}$$

  then we will show in appendix A that

  $$s_2 = (f_1^{real}, -f_1^{im}, f_2^{real}, -f_2^{im}, f_3^{real}, -f_3^{im}, H^{real}, -H^{im})_{m=-m_0}$$

  is a solution of (2.39)-(2.42) with $m = -m_0$. So by simply applying a phase shift of $\varphi_0 = \pi$ to the imaginary parts of a solution yields another valid solution for the same absolute value of m, but sign-reversed.

- From there it follows that the actual solution is independent of the sign of m. This means that for example the power spectrum of s_1 will already contain information about the $m = -m_0$ solution as well. It is known that for a nonrotating star the frequencies of counter- and co-rotating modes are degenerate. Rotation breaks this symmetry and leads to a splitting of these frequencies. The above remark implies that we will see this splitting already when analyzing the solution s_1; there will be no need to run another simulation for $m = -m_0$.

2.5.3 Boundary Conditions

Our system gets well-posed with the correct boundary conditions that we want to derive now. As it will be described in 3, our numerical domain is confined by the rotation axis (i.e. (ρ, ζ) with $\rho = 0$) and the surface (i.e. (ρ, ζ) with $\epsilon = p = 0$) of the compact star. Generally, instead of performing an integration of the perturbation equations also for the points at the boundary one often is able to prescribe the behaviour of the perturbation variables at these special points. In our case, due to the construction, the conditions for f_1, f_2, f_3 and H is very simple at the surface. For polytropic equations of state (see (2.17)) pressure p and energy density ϵ vanish at the surface. But what happens to the speed of sound there? It is with $\Gamma = 1 + 1/N$ and $N \geq 0$ always $\Gamma \geq 1$. From (2.25) it follows that

$$c_s^2 = \frac{\Gamma}{\epsilon/p + 1}$$

When we insert (2.23) there and work in units where $K = 1$ for simplicity, we have

$$c_s^2 = \frac{\Gamma^2}{p^{1/\Gamma - 1} + \Gamma(N+1)}$$

But since $1/\Gamma - 1 < 0$ we arrive at

$$\lim_{p \to 0} c_s^2 = 0$$

as well. If we take a look at (2.35)-(2.38), we finally see that our evolution variables are factorized in terms of energy density, pressure and sound speed so it immediately follows that they have to vanish at the surface as well, i.e.

$$f_1|_{\text{surface}} = f_2|_{\text{surface}} = f_3|_{\text{surface}} = H|_{\text{surface}} = 0\,. \tag{2.44}$$

For non-polytropic EoS the boundary condition at the surface would be a little bit more complicated. Usually one then does not have such a sharp drop of ϵ and p to zero instead one ends up with some kind of “atmosphere” where energy density and pressure slowly fade away to the vacuum that surrounds the compact object. The difficulty then is to define where the neutron star actually ends and the vacuum starts; usually this is done by setting a threshold value for the pressure.

For the boundary condition along the rotation axis we have to discuss scalar and vectorial perturbation variables separately; it will become clear in a second what we mean by this. Clearly, the energy density perturbation variable H has scalar character as well as f_2 which represents the ζ-component of the perturbed four-velocity. They have to be unique along the rotation axis, in particular they have to be independent of the azimuthal angle φ. So sitting on a point along the rotation axis and changing φ should not affect the values of the scalar quantities. Since we decomposed them like $e^{im\varphi}$ this means that for all $m \neq 0$ they have to be zero along the axis. In the axisymmetric case (i.e. $m = 0$) we cannot make a similar statement; here the solution along the rotation axis has to be finite and continuous. Numerically this can either be done by actual integration of the time evolution equations or by some kind of extrapolation algorithm. The second equation of (2.20) states that the metric potential W drops to zero at least like ρ when approaching the rotation axis and since f_2 is factorized with W (see (2.36)) even for $m = 0$ this quantity is zero along the axis.

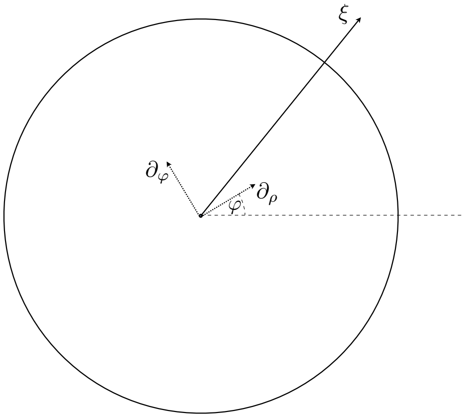

Figure 2.2: A nonzero vector ξ in the (ρ, φ)-plane as seen from a point at the rotation axis

The boundary condition for vectorial perturbations is a little bit different; see Figure 2.2 for more details.
It shows a vector ξ at some arbitrary point along the rotation axis together with the basis vectors ∂_ρ and ∂_φ for this point, i.e. $(\rho = 0, \zeta, \varphi)$. Due to the degeneracy of cylindrical coordinates at $\rho = 0$ the very same vector ξ will have different components (x^1, x^2) along the basis vectors depending on the value of φ, i.e.

$$\xi = x^1(\varphi)\partial_\rho + x^2(\varphi)\partial_\varphi$$

As it is clear from Figure 2.2 the components (x^1, x^2) will vary like $\cos(\varphi)$ or $\sin(\varphi)$; in our complex notation this is equivalent to $e^{\pm i\varphi}$. This means that in contrast to the scalar perturbations discussed earlier the vectorial perturbations are allowed to have nonzero values only for $m = \pm 1$. The time evolution variable f_1 is also factorized with the metric potential W which vanishes along the rotation axis (see (2.35)), so only f_3 can have a finite value there which can be obtained similar to the scalar case, i.e. direct integration or extrapolation.
As a summary the following Table 2.1 summarizes the boundary conditions for the perturbation variables along the rotation axis. For the astrophysical most relevant case, the $l = 2$, $m = 2$ quadrupolar deformation, all perturbation variables therefore have to vanish along the axis as well as at the surface.

m-value	$f_1\vert_{\text{axis}}$	$f_2\vert_{\text{axis}}$	$f_3\vert_{\text{axis}}$	$H\vert_{\text{axis}}$
0	0	0	0	finite and continuous
±1	0	0	finite and continuous	0
else	0	0	0	0

Table 2.1: Boundary condition for the perturbation variables along the rotational axis

This concludes the section about the derivation of the linearized perturbation equations. One can already guess that it is impossible to solve the full set of equations analytically. In the next chapter we will describe in more detail the setup and algorithms we were using to solve this problem numerically.

3

Numerical Implementations

Our goal is to solve the linear perturbation equations which govern the time evolution of small perturbations on compact objects in the form of system (2.39)-(2.42) derived in the last chapter. This cannot be done analytically; the equations are too complicated, they have nonconstant coefficients which are only given numerically so we also have to find a numerical algorithm that solves the equations in a stable way. During this PhD-thesis two conceptually very different attempts were made to implement a such a numerical scheme and only one of them finally led to a successful result. In this chapter we will describe and discuss both these methods.

3.1 A Brief Introduction to Spectral Methods

Since spectral methods are not so widely known as for example finite difference methods we will summarize the important points of this method here; for a more complete overview see for example [60], [61] or [62]. Speaking generally, spectral methods are a means to solve differential equations via a global approach by one high-order polynomial for the whole numerical domain. In contrast to this, finite difference schemes approximate the solution of differential equations by multiple overlapping low-order polynomials, mainly linear and/or quadratic ones. Each of these approaches has pros and cons we will cover here but as a first simple motivation for spectral methods let us look at an example. Consider the following linear time-independent ordinary differential equation on $\mathcal{A} = [-1, 1]$

$$u_{xx} - (x^6 + 3x)u = 0 \tag{3.1}$$

$$u(-1) = u(1) = 1$$

and let us approximate the solution of this equation by the fourth-order polynomial

$$u_4(x) = 1 + (1 - x^2)(a_0 + a_1 x + a_2 x^2)$$

With this approach we are already satisfying the boundary conditions. The three unknown coefficients a_0, a_1 and a_2 can be determined by demanding that the residual

$$R(x, a_0, a_1, a_2, a_3) = u_{4,xx} - (x^6 + 3x)u_4$$

has to vanish at three different points; this will eventually lead to a linear system of equations for the coefficients. If we for example set $x_{1,2,3} = (-1/2, 0, 1/2)$ then we end up with

$$a_0 = -\frac{784}{3807} = a_2, a_1 = 0$$

while the correct solution of (3.1) is given by

$$u(x) = e^{(x^4-1)/4}$$

Figure 3.1 shows a comparison between the exact solution and our simple approximation.

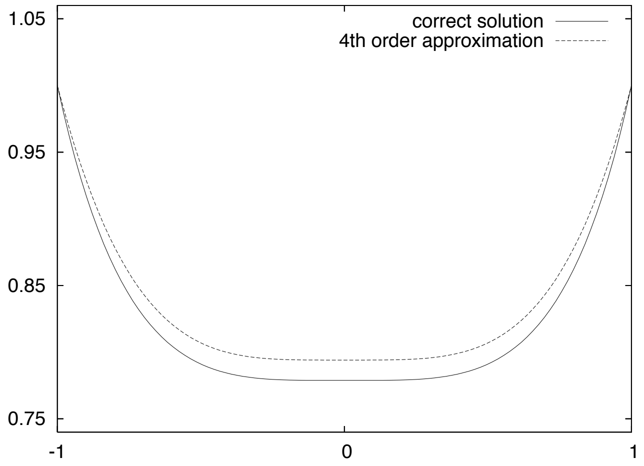

Figure 3.1: The solution of (3.1) and its 4th-order approximation on $\mathcal{A}$

As one can see, already this 4th-order polynomial catches the characteristic behaviour of the exact solution very well and of course as one increases the order of the approximating polynomial their relative difference will become smaller and smaller. Already with $N = 18$ so-called *collocation points* one can virtually see no difference.

This little example motivates the following more formal procedure (for the sake of simplicity we will restrict ourselves to time-independent, linear ordinary differential equations in one variable). If we have a differential equation of the form

$$\begin{aligned} \mathcal{L}u(x) &= f(x) \qquad x \in U \\ \mathcal{B}u(y) &= 0 \qquad\quad\ y \in \partial U \end{aligned} \tag{3.2}$$

we will approximate the solution u by a set of $N+1$ global basis functions ϕ_n

$$u(x) \approx u_N(x) = \sum_{n=0}^{N} a_n \phi_n(x) \tag{3.3}$$

and define the residual R by

$$R(x, a_0, a_1, \ldots, a_n) = \mathcal{L}u_N - f \tag{3.4}$$

For the exact solution u the residual vanishes identically; this of course is no longer true for its approximation. The various flavours of spectral methods now differ in their method to minimize the residual R for the unknown function u_N.

Keep in mind, that up to now we were not talking any further about how to treat the boundary conditions. In principle one can also make a global approach for the solution at the boundaries of the computational domain and minimize the corresponding residual. This will lead to additional constraints on the coefficients $a_0, a_1, \ldots, a_n$ but the correct handling of these constraints will lead us too far astray for this little introduction so we refer to the references for further details.

An elegant classification of the different spectral methods can be done with the help of the *mean weighted residual* method (MWR). In general, the approximate solution u_N will not make the residual vanish (unless of course u_N is already the exact solution). The MWR determines the unknown coefficients $a_0, a_1, \ldots, a_n$ by the requirement that

$$(w_i, R) = 0 \quad \forall\ i \in \{1, \ldots, N\}$$

for a set of $N + 1$ test functions w_i. with the inner product

$$(u, v) = \int\limits_a^b \omega(x)u(x)v(x)dx$$

and a non-negative weighting function ω on $[a, b]$. The various spectral methods now differ in their choice of the test functions. We distinguish for example

- pseudospectral or collocation methods $\quad w_i = \delta(x - x_i)$
- method of moments $\quad w_i = x_i$
- Galerkin method $\quad w_i = \phi_i(x)$

As an example we want to solve a differential equation with the Galerkin method. We then have

$$\begin{aligned}
(\phi_i, R) = 0 \quad &\Longleftrightarrow \quad (\phi_i, \mathcal{L}u_N - f) = 0 \\
&\Longleftrightarrow \quad (\phi_i, \mathcal{L}\sum_{n=0}^{N} a_n\phi_n) - (\phi_i, f) = 0 \\
&\Longleftrightarrow \quad \sum_{n=0}^{N} \mathcal{L}_{in}a_n = (\phi_i, f)
\end{aligned}$$

with

$$\mathcal{L}_{in} := (\phi_i, \mathcal{L}\phi_n)$$

The factors $\mathcal{L}_{in}$ in front of the unknown coefficients $a_0, a_1, \ldots, a_n$ are obtained by an integration with the Galerkin method which makes it a so-called *non-interpolating* method. In contrast to this, the AKM-Code used for computing the stationary background configuration of a rotating compact object we use in this thesis utilizes a pseudospectral algorithm. There it is

$$\begin{aligned}(\delta(x-x_i),R)=0 \quad &\Longleftrightarrow \quad R(x_i)=0 \\ &\Longleftrightarrow \quad \mathcal{L}u_N(x_i)=f(x_i) \\ &\Longleftrightarrow \quad \sum_{n=0}^{N}\mathcal{L}_{in}a_n=f(x_i)\end{aligned} \tag{3.5}$$

with

$$\mathcal{L}_{in} := \mathcal{L}\phi_n(x_i)$$

Here, no integration is needed; the coefficients $a_0, a_1, \ldots, a_n$ are determined by the requirement that the approximate solution u_N solves the differential equation exactly at the collocation points x_i. Of course at points other than the collocation points one has to interpolate appropriately to obtain a valid approximation to the exact solution. This is why pseudospectral methods are also called *interpolating* methods. One therefore has to take special care about the correct way of interpolation. The most simple way would be a polynomial interpolation on equidistant nodes. The following Figure 3.2 shows what will happen in this case.

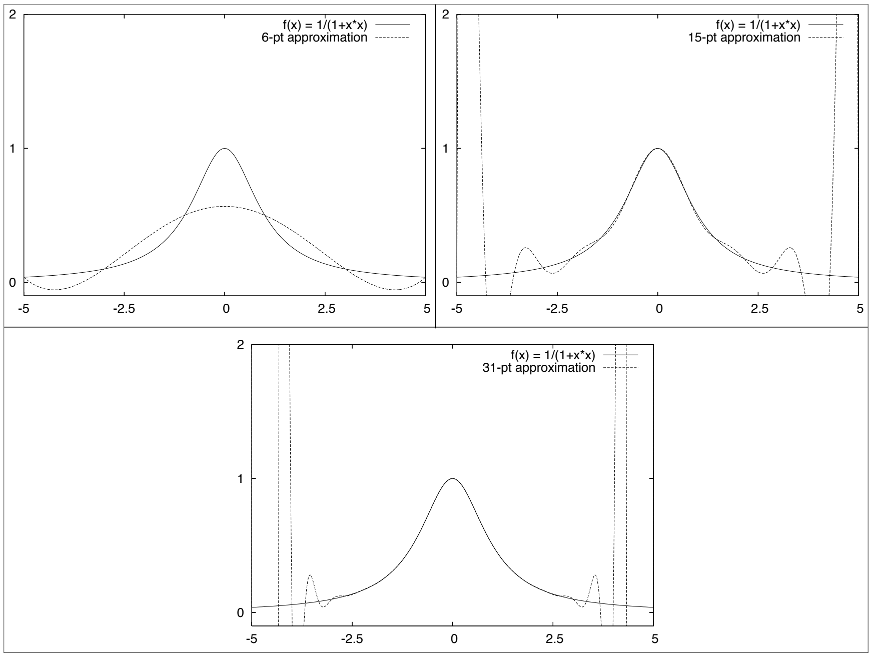

Figure 3.2: The function $f(x) = 1/(1+x^2)$ and some interpolating polynomials of different order

While the central part of the function is approximated quite well as the order of the polynomial increases, large deviations can be seen at the boundaries of the domain. It can be shown generally that this sequence of interpolating polynomials does not converge uniformly towards f, even if one increases the number of equidistant nodes. More specifically, if p_N interpolates a function f in $[a,b]$ where $p_N(x_j) = f(x_j)$ for $j = 1,\dots N$, the error $e(x)$ is given by

$$\begin{aligned} e(x) = f(x) - p_N(x) &= \prod_{j=0}^{N}(x - x_j)\frac{f^{(N+1)}(\zeta)}{(N+1)!} \ , \ \zeta \in [a,b] \\ &\leq \max_{t\in[a,b]} \omega(x)\frac{|f^{(N+1)}(t)|}{(N+1)!} \end{aligned}$$

with

$$\omega(x) = \prod_{j=0}^{N}(x - x_j)$$

It then can be shown that the roots and the extreme points of the so-called Chebyshev polynomials minimize the remainder function $\omega(x)$; they are defined by

$$\begin{aligned} T_n(x) &= \cos(n \arccos x) \quad , \ x \in [-1,1] \\ T_{n+1}(x) &= 2xT_n - T_{n-1} \\ T_n(x) = 0 &\rightarrow x_{root} = \cos\left(\pi\frac{2k-1}{2n}\right) \ , \ k = 1,\dots,n \\ ||T_n|| = 1 &\rightarrow x_{max} = \cos\left(\pi\frac{k}{n}\right) \ , \ k = 0,\dots,n \end{aligned} \tag{3.6}$$

The Chebyshev polynomials are only defined on $\mathcal{I} = [-1,1]$, however this is not a general problem since every interpolation interval can be rescaled to $\mathcal{I}$. The pseudospectral method then consists of solving (3.5) with either $\{x_{root}\}$ or $\{x_{max}\}$ as collocation points.

3.2 Pros and Cons of Spectral Methods

Here we shortly want to compare the spectral methods with the finite differences algorithm commonly used to solve differential equations. As already discussed above, spectral methods approximate the exact solution of such an equation by a global approach $u_N(x)$. In contrast to this finite differences schemes use local overlapping, low-order polynomials to compute derivatives. If we take again nodes with equidistant spacing h and perform a local quadratic 3-point interpolation of a function f, it turns out that the derivative of this interpolating polynomial is the standard second order stencil used for finite differences

$$\frac{df}{dx} = \frac{f(x+h) - f(x-h)}{2h} + O(h^2) \tag{3.7}$$

Due to this locality of finite difference methods, the solution of a given differential equation can be written as a matrix equation where the matrix that describes the differentiation process is sparse, i.e. most of the entries in this matrix are zero.

In contrast to this, spectral method approaches can be also converted to a corresponding matrix equation but in this case the differentiation matrix is full (this is of course due to the global character of the approximating function). From a numerical point of view there are very efficient methods to solve a set of linear equations with sparse matrices; they can be inverted in a fraction of the time that is needed to solve the equivalent problem with full matrices.

Another point is that the global approximating functions of spectral methods are not very well suited for the study of discontinuities which for example may appear in hydrodynamics in the form of shocks. Spectral methods work best when the problem to solve is smooth and regular. They are also more difficult to program than finite difference algorithms and irregular computational domains in more than one dimension affect the accuracy of spectral approaches more than their finite difference counterparts.

On the other hand, spectral methods are far more accurate than finite differences or stated differently, to achieve a certain level of accuracy far less nodes are needed in a spectral approach than in finite difference scheme. Consider for example a pseudospectral method with N nodes. As discussed in 3.1 the best choice of collocation points are either $\{x_{root}\}$ or $\{x_{max}\}$. If we increase the number of nodes N we have two effects working here. First, the (non-constant) grid spacing h decreases; this will increase the accuracy of our method even if its order would be fixed. But in contrast to local finite differences the order of the global interpolating polynomial is not fixed; it also increases with N. We already saw in (3.7) that a quadratic interpolation leads to an $O(h^2)$-error in the derivative. Correspondingly an N-point interpolation will have an error in the $O(h^N)$ range. But remembering our first remark the characteristic grid spacing is $O(1/N)$ so we have in the end for the pseudospectral error e

$$e \approx O[(1/N)^N]$$

The error is therefore decreasing faster than any finite power of N which is called *exponential* convergence. So it is no coincidence that in areas where very high accuracy is needed (meteorology and quantum chemistry for example) pseudospectral methods are used widely. There have been of course applications of spectral methods to neutron star oscillations as well; see [63] and references therein.

Also the numerical code we are using to compute the background model for our perturbation simulations utilizes pseudospectral methods. We already described in 2.4 the metric and coordinate system used for this computation; in the next section we will look at it from a numerical point of view and extend it to suit our particular needs.

3.3 Layout of the Computational Domain

The solution of the Einstein equations for a uniformly rotating perfect fluid object possesses several symmetry attributes that one can take advantage of for the numerical computation. It is not only symmetric with respect to the rotation axis but also with respect to the equatorial plane. It is therefore sufficient to consider the physical domain (keep in mind that we are working in comoving cylindrical coordinates, see [57] for a more detailed description).

$$\mathcal{D}_+ = \left[(\rho, \zeta)\,, \rho \geq 0, \zeta \geq 0\right]. \tag{3.8}$$

By means of a coordinate transformation

$$\mathcal{T}_+ = [(\sigma,\tau) \in [0,1] \times [0,1]\,, (\rho = \rho(\sigma,\tau), \zeta = \zeta(\sigma,\tau)) \in \mathcal{D}_+] \tag{3.9}$$

this part of the neutron star interior is mapped onto the unit square $\mathcal{U} = [0,1] \times [0,1]$ and the Einstein equations are solved there with a highly accurate pseudospectral method. The coordinate transformation is not entirely arbitrary; the coordinates used within the numerical domain feature some interesting properties.

Figure 3.3 shows the pseudospectral distribution of grid points with a total number of 18×18. There one can see the way the roots of the Chebyshev polynomials $\{x_{root}\}$ are arranged over the numerical domain; they actually never reach the boundaries, it is only the set $\{x_{max}\}$ (also known as *Gauss-Lobatto* points) that hold points directly on the boundary (see (3.6)). One also notices immediately the typical clustering of the collocation points there; an observation we can make plausible with a look at Figure 3.2. The largest error of the interpolating Lagrange polynomial can be seen near the boundaries of the interpolation interval. By distributing more grid points there as it is done by the Chebyshev roots one exactly counteracts this behaviour.

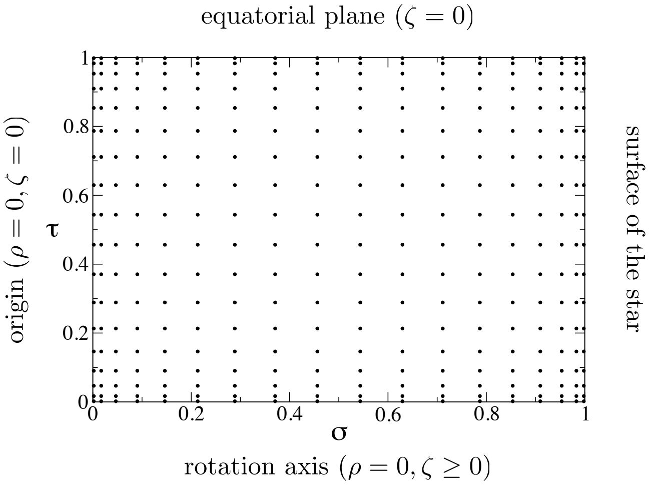

Figure 3.3: Layout of the numerical grid used to solve the TOV-equations for the stationary neutron star background model

Some properties of the coordinate transformation $\mathcal{T}_+$ are labelled in Figure 3.3. One can see, that the surface of the neutron star gets mapped onto $\sigma = 1$; this is independent of the rotation rate, even for rapidly rotating neutron stars this coordinate line always corresponds to the stellar surface. This is a big advantage over codes that use spherical-like coordinates and where the surface of the star lies somewhere in between different grid points for fast rotation. Direct time evolution as well as imposing boundary conditions is much more difficult then.

Additionally, $\tau = 0$ corresponds to the rotation axis above the equatorial plane and $\tau = 1$ to the equatorial plane itself. As mentioned earlier, since the background star is axisymmetric

as well as symmetric with respect to the equatorial plane, this computational domain suffices in order to construct the background model. Note also, since we have four boundaries in our computational domain, but only three physical boundaries (i.e. rotation axis, equatorial plane and stellar surface), one single point gets smeared into a coordinate line; in our case, $\sigma = 0$ corresponds to the origin of the star (i.e. $\rho = \zeta = 0$).
The coordinates (σ, τ) are similar to their spherical coordinates counterparts (r, θ) in the sense that moving from $\tau = 0$ to $\tau = 1$ on an arbitrary $\sigma = const.$-line means to start from a point at the rotation axis and move somewhat 'parallel' to the surface to a point at the equatorial plane. Vice versa if one moves along an arbitrary $\tau = const.$-line then one starts from the center of the star to the surface. The following Figure 3.4 depicts this situation for a rapidly rotating stellar model where the ratio of polar coordinate radius to equatorial coordinate radius is about $r_p/r_e = 0.6$. Clearly this neutron star model is non-spherical and in fact is rotating near its Kepler-limit, i.e. the critical angular velocity where it is torn apart by centrifugal forces; one can also see the formation of a bulge near the equatorial plane.

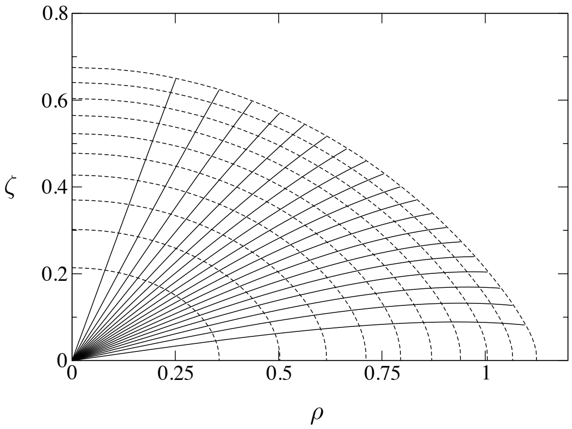

Figure 3.4: Some $\tau = const.$ (solid) and $\sigma = const.$ (dotted) coordinate lines in the (ρ, ζ) coordinate system

Nevertheless the surface of the stellar model is described by $\mathcal{S} = [(\rho(1,t), \zeta(1,t)), \tau \in [0,1]]$. While this computational domain is sufficient for computing stationary equilibrium configurations of rotating compact objects it is no longer adequate for studying linear perturbations which are not necessarily symmetric which respect to the equatorial plane. There are practically two ways to handle this additional freedom. The first one is the observation that any perturbation can be decomposed into a symmetric and an anti-symmetric part. To make this point clear let us look at a simple example in one dimension. If $\mathcal{A}_+ = [x\,, x \geq 0]$ is the computational domain, $f(x,t)$ is an arbitrary perturbation with values in $\mathcal{A}_- = [x\,, x < 0]$

too and $x = 0$ corresponds to the axis of symmetry, we have

$$f(x,t) = f_s(x,t) + f_a(x,t)$$

with

$$f_s(x,t) = \frac{f(x,t) + f(-x,t)}{2} \quad \text{and} \quad f_a(x,t) = \frac{f(x,t) - f(-x,t)}{2}\,.$$

If we now want to perform a time-evolution of an arbitrary initial perturbation $f(x,t_0)$ on $\mathcal{A} := \mathcal{A}_+ + \mathcal{A}_-$ we would decompose $f(x,t_0)$ into its symmetric and anti-symmetric part, apply our time-evolution scheme on $\mathcal{A}_+$ to them, complement the individual solutions according to their symmetry behaviour for $x < 0$ and finally add them up to get the overall solution. In this case two different boundary conditions have to be imposed at $x = 0$. For the symmetric part we have $\partial_x f_s(x,t)|_{x=0} = 0$ while for the anti-symmetric solution $f_s(x,t)|_{x=0} = 0$ has to hold. Of course, in order to study eigenfrequencies and eigenfunctions of specific modes it is sufficient to restrict these computations on either symmetric or anti-symmetric perturbation; in this case there is no need for a general purpose code that can handle arbitrary initial data.

However, the goal of this thesis is to write a code that can deal with arbitrary initial data and so we choose the second option for solving the problem of non-symmetric initial data; we extend our physical and computational domain to include also the region

$$\mathcal{D}_- = [(\rho,\zeta)\,, \rho \geq 0, \zeta < 0]\,. \tag{3.10}$$

Practically this is done by taking two copies of $\mathcal{D}_+$ and 'glue' them together along the equatorial plane. The computational domain therefore increases in the τ-dimension, i.e. the θ-direction if we refer again to the analogy with spherical coordinates we discussed earlier.

$$\mathcal{T} = [(\sigma,\tau) \in [0,1] \times [0,2]\,, (\rho = \rho(\sigma,\tau), \zeta = \zeta(\sigma,\tau)) \in \mathcal{D} := (\mathcal{D}_+ + \mathcal{D}_-)] \tag{3.11}$$

Since the computational domain now is the rectangle $[0,1] \times [0,2]$ and no longer the unit square $[0,1] \times [0,1]$ we will have to reorder the gridpoints. Clearly by just joining two samples of the computational domain $\mathcal{D}_+$ along the equator the overall gridpoints do not longer distribute according to the requirements of spectral methods, see Figure 3.3 for example. We have to rearrange them in order to fit our new domain. Since we also explicitly want to have boundary points where we apply the conditions derived in 2.5.3, this is a good point to switch to the Gauss-Lobatto points, i.e. the extreme points of the Chebyshev polynomials (see (3.6)). The Chebyshev polynomials are already minimizing the global interpolation error and since the AKM code uses a pseudospectral representation of all necessary equilibrium quantities we take this representation to interpolate the background values to our new computational domain. In this domain there are no other boundary conditions to impose than described in Section 2.5.3; the equatorial plane now lies in the interior of our numerical grid and its boundaries are given by the origin ($\sigma = 0$), the surface ($\sigma = 1$), the part of the rotation axis above the equatorial plane ($\tau = 0$) and the corresponding part underneath the equatorial plane ($\tau = 2$). Of course we have to pay a price for studying arbitrary perturbations: Our grid is now twice as large as before; this means for a 2D-code an increase in computation time by a factor of 4. The final computational domain for a resolution of 10×16 gridpoints can be seen in Figure 3.5.

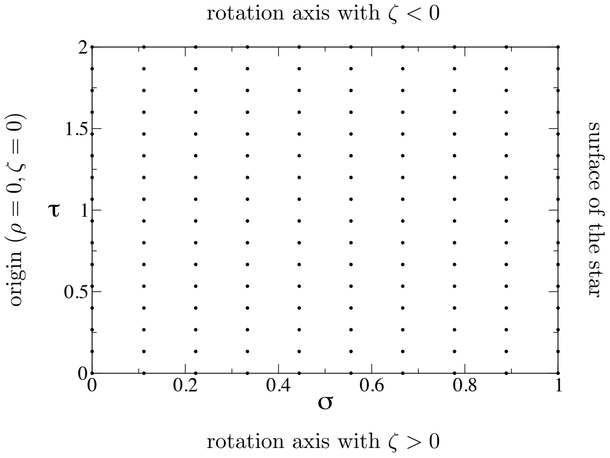
rotation axis with $\zeta < 0$
origin ($\rho = 0, \zeta = 0$)
surface of the star
rotation axis with $\zeta > 0$
τ
σ
0
0.5
1
1.5
2
0
0.2
0.4
0.6
0.8
1

Figure 3.5: Complete numerical domain $\mathcal{T}$ for the time-evolution code

Special care has to be taken of the correct transformation behaviour of our various background quantities which we, up to now, only know in $\mathcal{D}_+$. In addition to simply mirror all necessary quantities along the equatorial plane (i.e. along $\tau = 1$), some derivatives need to be multiplied by a factor of -1. Derivatives with respect to ρ are no problem; if (σ, τ) denotes a grid point in $\mathcal{D}_+$ (i.e. $\tau \leq 1$) and g is an arbitrary background quantity, we can write

$$\frac{\partial g}{\partial \rho}|_{(\sigma,\tau)} = \frac{\partial g}{\partial \rho}|_{(\sigma,2-\tau)} . \tag{3.12}$$

It is easy to see, that this no longer holds true when we look at ζ-derivatives. Suppose that we take values of a background quantity g at two different ζ-locations ζ_1, ζ_2 in $\mathcal{D}_+$ with $\zeta_1 < \zeta_2$. We can then write the derivative as

$$\frac{\partial g}{\partial \zeta}|_{\mathcal{D}_+} = \frac{g(\zeta_2) - g(\zeta_1)}{h} + O(h) \quad \text{with} \quad h = \zeta_2 - \zeta_1$$

When we now extend g to $\mathcal{D}_-$ it is $-\zeta_1 > -\zeta_2$ and $g(-\zeta_i) = g(\zeta_1), i = 1, 2$ and we arrive at

$$\frac{\partial g}{\partial \zeta}|_{\mathcal{D}_-} = \frac{g(-\zeta_1) - g(-\zeta_2)}{h} + O(h) = \frac{g(\zeta_1) - g(\zeta_2)}{h} + O(h) = -\frac{\partial g}{\partial \zeta}|_{\mathcal{D}_+}$$

So considering ζ-derivatives we generally have

$$\frac{\partial g}{\partial \zeta}|_{(\sigma,\tau)} = -\frac{\partial g}{\partial \zeta}|_{(\sigma,2-\tau)} . \tag{3.13}$$

Yet another transformation behaviour has to do with the fact, that the equations we want to solve (i.e. system (2.39)-(2.42)) are written in (ρ, ζ)-coordinates but we use as numerical domain our extended (σ, τ)-system. For our perturbation variables we have to switch between these systems. So in addition to all background quantities and their derivatives with respect to ρ and ζ, also the transformations coefficients $\partial\sigma/\partial\rho$, $\partial\sigma/\partial\zeta$, $\partial\tau/\partial\rho$ and $\partial\tau/\partial\zeta$ are available in $\mathcal{D}_+$. With these coefficients it is possible to compute for any perturbation quantity f given on the numerical domain $\mathcal{T}$ the values of

$$\begin{aligned} \frac{\partial f}{\partial\rho} &= \frac{\partial f}{\partial\sigma}\frac{\partial\sigma}{\partial\rho} + \frac{\partial f}{\partial\tau}\frac{\partial\tau}{\partial\rho} \\ \frac{\partial f}{\partial\zeta} &= \frac{\partial f}{\partial\sigma}\frac{\partial\sigma}{\partial\zeta} + \frac{\partial f}{\partial\tau}\frac{\partial\tau}{\partial\zeta} \end{aligned} \tag{3.14}$$

we need to know for the righthand-sides of (2.39)-(2.42).

Equations (3.14) are of course also valid for the background quantities and this helps us to find the correct transformation behaviour for the transformation coefficients when going from $\mathcal{D}_+$ to $\mathcal{D}_-$. We know how the ρ- and ζ-derivatives transform in $\mathcal{D}_-$ as well what happens to their σ- and τ-derivatives there. Similar to the argumentation above we don't have a sign flip in $\partial f/\partial\sigma$ but we will have one in $\partial f/\partial\tau$. Comparing then the lefthand-sides of (3.14) with their corresponding righthand-sides finally leads to

$$\begin{aligned} \frac{\partial\sigma}{\partial\rho}|_{(\sigma,\tau)} &= \frac{\partial\sigma}{\partial\rho}|_{(\sigma,2-\tau)} \\ \frac{\partial\sigma}{\partial\zeta}|_{(\sigma,\tau)} &= -\frac{\partial\sigma}{\partial\zeta}|_{(\sigma,2-\tau)} \end{aligned} \tag{3.15}$$

and

$$\begin{aligned} \frac{\partial\tau}{\partial\rho}|_{(\sigma,\tau)} &= -\frac{\partial\tau}{\partial\rho}|_{(\sigma,2-\tau)} \\ \frac{\partial\tau}{\partial\zeta}|_{(\sigma,\tau)} &= \frac{\partial\tau}{\partial\zeta}|_{(\sigma,2-\tau)} \end{aligned} \tag{3.16}$$

Now the extended computational domain $\mathcal{D} = \mathcal{D}_+ + \mathcal{D}_-$ is adequately prepared for the actual time-evolution. In the following section we will describe our approach for integrating the perturbation equations.

3.4 The Time-Evolution Scheme

The utilization of spectral methods for time dependent problems is mostly done for the spatial part of the differential equations while standard finite difference techniques are applied for the actual time integration; see for example [61] for references. Generally this kind of algorithm is easier to implement and there is already a lot of experience about stability and convergence of the various finite difference time integrators. Computation-wise it is also much cheaper to advance from one time-level to the next; in a full-fledged spectral code one would make a global approximation to the exact solution not only in space like we described here so far but in the time-coordinate as well. This means to solve the differential equation instantly for all times within the desired interval. Recently a first step towards this kind of approach with applications to General Relativity was performed in [64], however we followed the more traditionally path and used pseudospectral methods solely for computing spatial derivatives. Let us look how this works again in one dimension where we will take the roots of the N-th Chebyshev polynomial $\{x_k, k = 1, \dots, N\}$ as collocation points. Our goal is to write an arbitrary function f with known values on the x_k as

$$u(x) = \sum_{j=0}^{N-1} a_j \, T_j(x)$$

so that $u(x_k) = f(x_k)$. We will then have for all $i = 0, \dots, N-1$

$$T_i(x_k)u(x_k) = T_i(x_k)f(x_k) = \sum_{j=0}^{N-1} a_j \, T_i(x_k)T_j(x_k)$$

Summation over k yields

$$\sum_{k=1}^{N} T_i(x_k)f(x_k) = \sum_{k=1}^{N} a_0 \, T_i(x_k)T_0(x_k) + \sum_{k=1}^{N} \sum_{j=1}^{N-1} a_j \, T_i(x_k)T_j(x_k) \tag{3.17}$$

The Chebyshev polynomials form a orthogonal set of basis function, so if we have M roots of the M-th Chebyshev function the orthogonality relation

$$\sum_{l=1}^{M} T_a(x_l)T_b(x_l) = \begin{cases} 0 & a \neq b \\ M/2 & a = b \neq 0 \\ M & a = b = 0 \end{cases} \tag{3.18}$$

holds. We now set $i = 0$ in (3.17) and the last term of its righthand-side will vanish due to the first case in (3.18) and we end up with

$$a_0 = \frac{1}{N} \sum_{k=1}^{N} f(x_k)T_0(x_k)$$

Similarly, for $i \neq 0$ the first term on the righthand-side of (3.17) and we rewrite the remaining part as

$$\sum_{k=1}^{N} \sum_{j=1}^{N-1} a_j \, T_i(x_k)T_j(x_k) = \sum_{j \neq i}^{N-1} \sum_{k=1}^{N} a_j \, T_i(x_k)T_j(x_k) + \sum_{k=1}^{N} a_i \, T_i(x_k)T_i(x_k)$$

Since $i \neq 0$ the first term on the righthand-side again is zero and we arrive at

$$a_i = \frac{2}{N} \sum_{k=1}^{N} f(x_k)T_i(x_k)$$

We now define for all $j = 0, \dots, N-1$

$$c_j := \frac{2}{N} \sum_{k=1}^{N} f(x_k)T_j(x_k)$$

and then it follows that

$$\begin{aligned} u(x) &= \frac{1}{2}c_0 T_0(x) + \sum_{j=1}^{N-1} c_j\, T_j(x) \qquad (3.19) \\ &= \sum_{j=0}^{N-1} c_j\, T_j(x) - c_0 + \frac{1}{2}c_0 \\ &= \sum_{j=0}^{N-1} c_j\, T_j(x) - \frac{1}{2}c_0 \end{aligned}$$

Due to the fact that these coefficients c_j need to be evaluated for all necessary quantities after each timestep it is crucial to find a fast and efficient numerical algorithm for their computation. Luckily this is not a major problem; if one does the substitution $x = \cos\alpha$ in (3.6) one recognizes that the decomposition (3.19) is just a Fourier cosine series and the coefficients c_j can be calculated very fast using standard Fast Fourier Transform (FFT) techniques.

Given the coefficients c_j it is also straightforward to calculate the derivative of the approximating function $u(x)$. If we write

$$u'(x) = \sum_{j=0}^{N-1} c'_j T_j(x) - \frac{1}{2}c'_0 \qquad (3.20)$$

we have the recurrence equation

$$c'_{j-1} = c'_{j+1} + 2jc_j \quad (j = N-1, \ldots, 1) \quad \text{with} \quad c'_N = c'_{N-1} = 0$$

We then have to evaluate (3.19) and (3.20) on the collocation points $\{x_k, k = 1, \ldots, N\}$ which also can be done very efficiently.

As actual time-integration scheme we chose the popular 4th-order Runge-Kutta method (RK4). Although this algorithm requires the fourfold evaluation of the righthand-sides of our perturbation equations per timestep we didn't want to spoil the high accuracy of our spatial differentiation with a low order time integration. If we have a differential equation of the form

$$\dot{y} = f(y)$$

where the dot denotes the time derivative and we denote $y_n = y(t_n)$ we then can write

$$y_{n+1} = y_n + \frac{h}{6}(k_1 + 2k_2 + 2k_3 + k_4) \qquad (3.21)$$

with

$$\begin{aligned} k_1 &= f(y_n) \\ k_2 &= f(y_n + h/2\, k_1) \\ k_3 &= f(y_n + h/2\, k_2) \\ k_4 &= f(y_n + h\, k_3) \end{aligned}$$

and $t_{n+1} = t_n + h$. Since RK4 is an explicit scheme, that is the righthand-side of (3.21) does not depend on y_{n+1}, the maximum allowed timestep h cannot be arbitrarily high (Courant-Friedrichs-Lewy criterion). An order of magnitude estimation for h in our specific case is given by

$$h \approx \frac{\Delta x}{c_s}$$

where Δx is the average grid spacing and c_s is the speed of sound.
Now everything has been set up for numerically integrating the perturbation equations. We presented the formulation of our linearized problem in 2.5 and described the numerical approach we took initially in 3.3 and in this section. Now we can turn to the results we achieved with this method.

3.5 Results with the Pseudospectral Approach

Unfortunately with this kind of algorithm we were not able to get a stable evolution code. Very soon, i.e. after a couple of timesteps high frequency oscillations of exponentially growing modes showed up at the origin of our computational domain, destroying our simulation almost immediately. The series of pictures in Figure 3.6 on the following page shows a typical result of a simulation in this case. As initial condition a Gaussian distribution in both σ- and τ-direction was chosen for the ρ-component of the perturbed 4-velocity and then evolved according to the linearized perturbation equations for $m = 0$. This initial velocity profile can be seen in the very first picture of the sequence in Figure 3.6 where also the coordinates (σ, τ) of the computational domain are indicated. In this simulation we only show the $\mathcal{D}_+$-part of the computational domain so $\tau \in [0, 1]$. As one can see when following the snapshots, a small wave is travelling from the center of the Gauss distribution towards the surface, i.e. towards larger σ. It then gets reflected there and starts to move inward while one can see additional oscillatory motion especially at the equatorial plane. As soon as these waves reach the vicinity of the origin (i.e. $\sigma = 0$) high frequency oscillations both in space and in time emerge there, ultimately leading to a failure of the time integration.
Now of course the obvious question is what the reason for this behaviour might be. In fact it is not very difficult to spot several weak points in our formulation of the problem. First of all if we go back and take a closer look at the perturbation equations (2.39)-(2.42) then especially in the last to equations governing the evolution of δu_φ and $\delta\epsilon$ singular terms of high order appear in the denominator of some coefficients; most striking the factor $1/F$ and $1/(FW)$. Since F is defined by (2.34) and the two metric potentials a and W behave near the rotation axis of the star according to (2.20) it is not difficult to see that we have

$$\begin{aligned} \lim_{\rho\to 0} |F\rho^{-4}| &< \infty \qquad (3.22) \\ \lim_{\rho\to 0} |FW\rho^{-5}| &< \infty \end{aligned}$$

Of course this singular behaviour partially gets absorbed by similar factors in the numerator of the perturbation equations but in any case we have to deal with coefficients that grow very strong towards the rotation axis. This does not mean that numerical algorithms will fail a priori as soon as they encounter singular terms. For example when rewritten in spherical

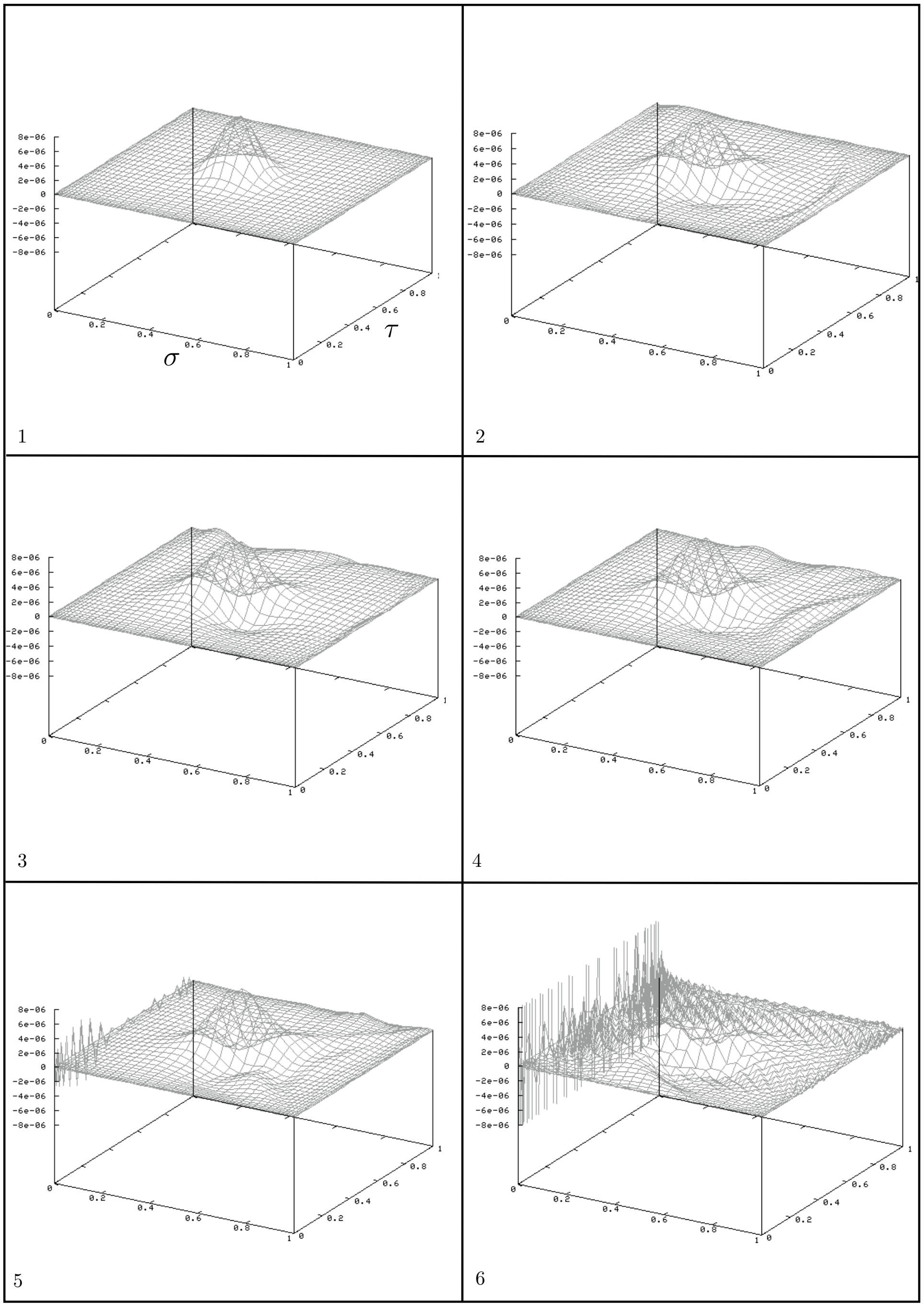

Figure 3.6: Snapshots of the u_ρ-time evolution with our pseudospectral/RK4 algorithm; the numbers label the temporal order

coordinates, the one-dimensional wave equation $\ddot{f} = v^2 f_{xx}$ also possesses a singular factor which behaves like $1/r$ but nevertheless numerical algorithms usually have no difficulties to solve the wave equation in a spherical system. Therefore also the order of the singular terms matter and in our case they simply grow too strong towards $\rho = 0$. As soon as small irregularities show up near the origin in Figure 3.22 there is no hope to save the simulation. As already discussed in Section 3.2 spectral methods are a very effective tool as long as the solution stays smooth and regular. While finite difference schemes due to their locality can handle the development of divergences to some degree, spectral methods are a global approach. Irregularities in one part of the computational domain will immediately affect the derivatives all-over the numerical grid; they are therefore generally more fragile to instabilities due to singular behaviour of some coefficients.

Hence we chose to abandon this type of implementation and turned to the more traditional way of using a finite difference approach. In practice this means basically just a change in the distribution of gridpoints and in the computation of derivatives since most of the procedures we presented in this chapter (especially in Section 3.3) are equally applicable for the finite difference case. In the next section we will briefly describe the modifications we incorporated.

3.6 The Finite Difference Algorithm

The layout of the computational domain is identical to the pseudospectral case. The only difference is that instead of covering $\mathcal{T}$ with unequally distributed Chebyshev collocation points we will interpolate to a uniformly arranged finite difference grid where we can write

$$\sigma[i] = \frac{i}{M1-1}\,, \quad i = 0,\ldots,M1-1$$

$$\tau[i] = 2.0\frac{j}{2\cdot M2-1}\,, \quad j = 0,\ldots,2\cdot M2-1$$

Here the resolution of the original numerical domain $\mathcal{T}_+$ is $M1 \times M2$. As described in Section 3.3 we patch to copies of $\mathcal{T}_+$ together at the equatorial plane. The number of gridpoints in σ-direction therefore does not increase but in the τ-dimension we get twice the number of nodes. The entire grid $\mathcal{T}$ hence has a resolution of $M1 \times 2 \cdot M2$.

We use standard second order central difference stencils for computing derivatives in both spatial dimensions. For a given function $u(x)$ we make a Taylor expansion around $x = x_0$ and truncate it after the linear term; we then get

$$\begin{aligned} u(x_0+h) &= u(x_0) + u'(x_0)h + \mathcal{O}(h^2) \\ u(x_0-h) &= u(x_0) - u'(x_0)h + \mathcal{O}(h^2) \end{aligned}$$

If we subtract these two equations we arrive at the well-known relationship

$$u'(x_0) = \frac{u(x_0+h) - u(x_0-h)}{2h} + \mathcal{O}(h^2)$$

If h is sufficiently small we can take the first part of the righthand-side as an approximation for the derivative of u at x_0. As a side note and for a little interconnection to the pseudospectral methods discussed above if we define $x_1 = x_0 + h$ and $x_2 = x_0 - h$ the uniquely defined interpolating Lagrange polynomial of second order is given by

$$I_3(x) = -u(x_0)\frac{(x-x_1)(x-x_2)}{h^2} + u(x_0+h)\frac{(x-x_0)(x-x_2)}{2h^2} + u(x_0-h)\frac{(x-x_0)(x-x_1)}{2h^2}$$

It then follows immediately that

$$I_3'(x_0) \approx u'(x_0) = \frac{u(x_0+h)-u(x_0-h)}{2h}$$

If we apply this relationship to both of our spatial dimensions σ and τ we will make an error which is of second order in the grid spacing h; i.e. doubling the resolution will lower the truncation error by a factor of four. To achieve higher accuracy one could use higher order stencils which also include grid points at $x_0 - 2h$, $x_0 + 2h$ etc. but this leads to several weak points. First of all it will increase the computational costs significantly if one has to perform these kind of computations very frequent which will be the case in our time evolution. Second, with central differences we don't have to worry about points near the boundary. As an example let us consider the surface of the star, i.e. $\sigma = 1$. For gridpoints directly at the boundary we apply the appropriate boundary condition but the value of a particular perturbation quantity at the gridpoint closest to the surface has to be determined by direct time evolution. With central differences we need to read out the corresponding value to the "right" (at the surface) and to the "left" (in the interior) of this particular point which can be done without problems. However if we choose a higher order scheme for spatial differentiation we would have to know the value of a particular quantity at points beyond our actual computational domain. Usually this is done by introducing so-called *ghost-points* and combined with some symmetry considerations one is able to assign reasonable values to them. There are also high order one-sided difference approximations one can use there; however this will also complicate the treatment of border-zone areas. None of the points discussed here is really crucial; one could implement high order stencils and the additional computational expenses can be solved by parallelization but we decided to keep things simple so we won't follow this way here and stay with our second order accurate scheme.

Our argument for using a fourth order Runge-Kutta method in Section 3.4 was that we didn't want to combine a highly accurate method for spatial differentiation with a low order finite difference time integrator. While this certainly holds true in the pseudospectral case it is not strictly necessary here. Since our central difference approach is accurate up to second order we don't need a fourth order time integration scheme which is computationally very expensive. In the end the accuracy of our complete algorithm is determined by the accuracy of the lowest order subroutine which in our case is second order up to now.

Based on this considerations we implemented another time integrator which has become quite popular in numerical relativity; the iterated Crank-Nicholson method.

3.6.1 Crank-Nicholson Methods

For simplicity consider an ordinary differential equation of the form

$$\frac{\partial y}{\partial t} = f(y,t)$$

When discretizing this equation for numerical integration the original Crank-Nicholson method is applied by taking the average of the righthand side between the beginning and end of a given timestep. If we write y_n for $y(t_n)$ and $t_{n+1} = t_n + \Delta t$ this means

$$\frac{y_{n+1} - y_n}{\Delta t} = \frac{f(y_{n+1}, t_{n+1}) + f(y_n, t_n)}{2} \tag{3.23}$$

This is an implicit scheme; the righthand side also contains values of the unknown function at the time t_{n+1} and it is not possible to write down an explicit formula for y_{n+1} just in terms of y_n and t_n. However, let us suppose that the resolution of our one-dimensional domain in this example is N. Then for a given discretization of $f(y, t)$ we can write down the N equations corresponding to (3.23) for the N unknown values of y_{n+1}; eventually this leads to a coupled system of equations one has to solve at each time step.

While implicit schemes are more difficult to implement than explicit schemes where one can write y_{n+1} entirely in terms of y_n and t_n they also have several advantages. Generally they are much more stable then explicit algorithms. At least in the case of constant coefficients one can perform a von Neumann stability analysis which then will show that the amplitude of spurious Fourier modes does not increase over time and is independent of a CFL constraint; i.e. there are practically no restrictions on the timestep one has to choose to get a stable evolution (in contrast to explicit schemes, see 3.4). But as already mentioned the need of solving a coupled system of algebraic equations each timestep is computationally very expensive and becomes even more complicated in two dimensions.

There is an explicit version of the Crank-Nicholson algorithm based on the idea of averaging solutions of different timesteps to an intermediate solution (see [65] for example) which has been implemented in our code and which we will present now. Consider the 1D advection equation

$$\dot{u}(x, t) = u'(x, t)$$

and let us denote $u_j^n = u(j\Delta x, n\Delta t)$. The first iteration consists of computing an intermediate variable ${}^{(1)}\bar{u}$ by using central differences on the righthand-side for time integration followed by an averaging process, i.e.

$$\frac{\tilde{u}_j^{n+1} - u_j^n}{\Delta t} = \frac{u_{j+1}^n - u_{j-1}^n}{2\Delta x} \qquad \text{and} \qquad {}^{(1)}\bar{u}_j^{n+1/2} = \frac{1}{2}(\tilde{u}_j^{n+1} + u_j^n) \tag{3.24}$$

The iteration is finished by applying the very same time integration scheme but this time with ${}^{(1)}\bar{u}$ on the righthand-side and we get

$$\frac{u_j^{n+1} - u_j^n}{\Delta t} = \frac{{}^{(1)}\bar{u}_{j+1}^{n+1/2} - {}^{(1)}\bar{u}_{j-1}^{n+1/2}}{2\Delta x} \tag{3.25}$$

Any number of iterations can then be carried out in the same way but not all of them are stable. A stability analysis shows an alternating behaviour; while the zeroth and first iteration are unstable (where zeroth iteration means no averaging at all) the second and third iteration are stable, given that a certain Courant constraint is fulfilled, then the fourth and fifth iteration again are unstable and so on. The amplitude a of a single Fourier mode oscillates around $a = 1$ and converges to this value in the limit of infinite iterations. From this point of view it makes no sense to perform more than two iterations since the accuracy

of the method will stay second order.
The iterated Crank-Nicholson scheme belongs to a larger class of so-called *θ-methods*. The averaging which is applied to the intermediate solution in (3.24) with a factor of 1/2 can be generalized to

$$^{(1)}\bar{u}_j^{n+1/2} = \theta\tilde{u}_j^{n+1} + (1-\theta)u_j^n$$

with $0 < \theta < 1$; for $\theta = 1/2$ we again obtain the auxiliary solution of (3.24). This numerical scheme has been implemented successfully for relativistic hydrodynamical simulations on ideal an viscous fluids with $\theta = 0.6$; see [66],[67] and it has been observed that the unequal weighting leads to an improved stability of the code. In [68] a new generalization to these θ-methods was introduced; the weight terms are being swapped between subsequent averaging processes. If we have in iteration N

$$^{(N)}\bar{u}_j^{n+1/2} = \theta\tilde{u}_j^{n+1} + (1-\theta)u_j^n$$

then the average needed for the next iteration is given by

$$^{(N+1)}\bar{u}_j^{n+1/2} = (1-\theta)\tilde{u}_j^{n+1} + \theta u_j^n$$

It can be shown that as long as the number of iterations is even, the sequence in which the averages are computed is irrelevant so that θ can be replaced by $1-\theta$ without any implications. Yet another advantageous effect of using unequal weights is that they add an explicit numerical dissipation term into the discretized evolution equations. Usually an extra amount of dissipation is often desired since it helps to suppress the growth of spurious and unstable modes. Additionally the swapping of the weights decreases the dispersion of the numerical solution. The downside is that using values $\theta \neq 1/2$ will reduce the accuracy of this time integrator to first order; however we chose to adopt this scheme with a value of $\theta = 0.6$ as well. The way in which the actual evolution code is written makes it very easy to change this weight though so we are not constrained to use only this particular value.

3.7 Results with the Finite Difference Approach

In analogy to the test case we investigated in Section 3.5 for the pseudospectral approach we will use an initial Gaussian velocity distribution for δu_ρ here as well. The snapshots in Figure 3.7 show a typical result of a simulation for $m = 0$ with our implementation of the iterated Crank-Nicholson scheme and swapped weights. Several points are worth mentioning here. First of all the chronology of the various pictures in the figure is not identical to the temporal progression in the corresponding Figure 3.6; in both cases we chose the pictures to depict some of the characteristic behaviour of the numerical solution rather than create figures at certain predefined timesteps. Also with the finite difference approach the simulation becomes unstable although the perturbation equations can be evolved for a longer period of time than in the pseudospectral case. In Figure 3.7 one again finds the outgoing wave travelling towards the surface of the neutron star. And again an instability occurs but this time not directly along the degenerated origin (i.e. $\sigma = 0$) but in its close vicinity which then takes over most parts of the numerical grid. The late time evolution is dominated by exponentially growing modes with an ever increasing amplitude. However in contrast to the

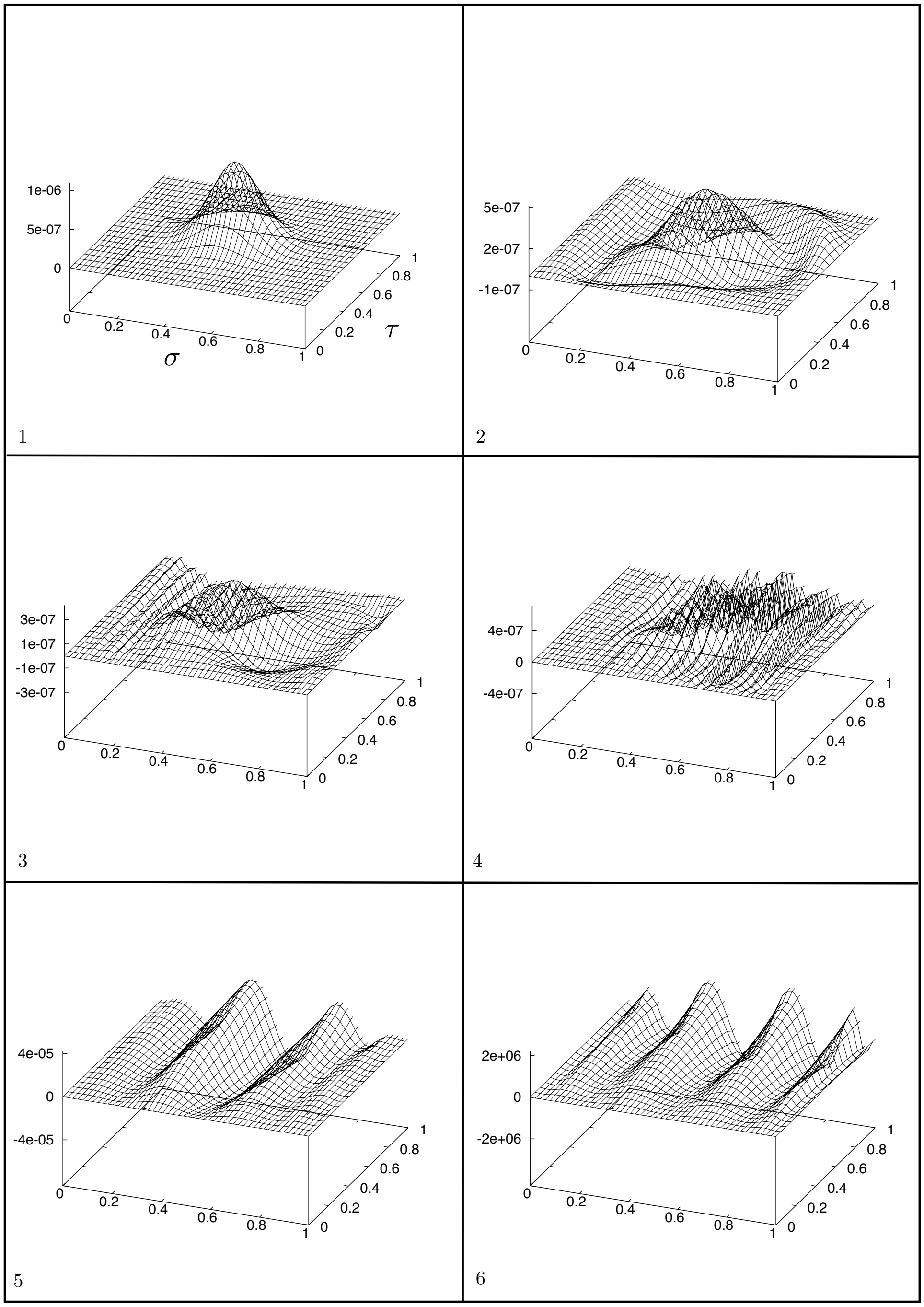

Figure 3.7: Snapshots of the u_ρ-time evolution with the iterated Crank-Nicholson algorithm and swapped weights; the numbers label the temporal order

corresponding pseudospectral simulation, the time integration though exponentially growing still remains smooth particularly along the rotation axis whereas in the spectral case the behaviour of the solution shows many discontinuities especially at or near the origin; i.e. compare the last sub-picture of Figure 3.7 with the equivalent picture in 3.6.
So there is reasonable hope that if we can control the spurious, exponentially growing modes in this formulation we eventually may be able to perform a stable time evolution. As already described in 3.6.1 the use of unequal weights in the iterated Crank-Nicholson algorithm introduces a small amount of dissipation; however as we have seen here it is not enough to suppress the unstable modes. The next logical step is the introduction of an explicit dissipation term in the evolution equations in order to gain control over the instabilities. Of course we are then solving a slightly different set of equations but if the additional contribution of this *artificial viscosity* can be kept as small as needed for a stable evolution then the overall effect of this auxiliary term may be negligible.

3.8 Artificial Viscosity

Consider a partial differential equation of the form

$$\frac{\partial u}{\partial t} = \mathcal{P}\left(\frac{\partial}{\partial x}\right) u = \sum_{\nu} A_{\nu} \frac{\partial u}{\partial x^{(\nu)}}$$

Numerically this equation is solved typically by the method of lines; the same method we use with the iterated Crank-Nicholson scheme. We approximate the spatial part by a finite difference representation $\mathcal{Q}_1$ and obtain an ordinary differential equation

$$\frac{dw}{dt} = \mathcal{Q}_1 w \tag{3.26}$$

to solve with time integrators like Runge-Kutta. In general, equation (3.26) is not stable; it allows solution that grow like $\exp(at/h)$, where $a > 0$ and h is the average grid spacing. This exponentially growing solutions can be suppressed by altering the system slightly and consider the equation

$$\frac{dw}{dt} = \mathcal{Q} w \quad \text{with} \quad \mathcal{Q} = \mathcal{Q}_1 + \alpha \mathcal{Q}_2\,, \quad \alpha = const. \tag{3.27}$$

and

$$\mathcal{Q}_2 = \sum_{\nu} D^r_{+x^{(\nu)}} D^r_{-x^{(\nu)}}$$

Here, the value of r depends on the accuracy of the original finite difference operator $\mathcal{Q}_1$ but is usually set to $r = 1$ and D_+, D_- are the standard one-sided differences for each of the ν dimensions of the problem; in one dimension and as usual with $w_j = w(x_j)$ we would have

$$D_{+x} w_j = \frac{w_{j+1} - w_j}{h} \qquad \text{and} \qquad D_{-} w_j = \frac{w_j - w_{j-1}}{h}$$

So effectively we are adding an explicit diffusion term of the form αw_{xx} to system (3.26) and it can be shown that for sufficiently large α the modified equation (3.27) is stable and has certain dissipative properties (see [69] for details). Of course we are now looking for solutions of a modified differential equations and the larger the dissipation coefficient α the larger we expect the deviations from the original solution. Generally there are no a priori estimations on the discrepancy between the solution of (3.26) and the solution of the modified system (3.27) when varying α; it depends on the particular problem. Our strategy is to use the smallest amount of artificial viscosity that is needed for a stable evolution. We will introduce four different dissipation coefficients $\alpha_1, \dots, \alpha_4$; one coefficient for each of our four perturbation equations (2.39)-(2.42). The finite difference operator representing the additional artificial viscosity has the form

$$\mathcal{V} = (D_{+\sigma}D_{-\sigma} + D_{+\tau}D_{-\tau}) \tag{3.28}$$

where σ and τ are the coordinates of the computational domain. With this scheme we were finally able to evolve the time evolution equations in a stable way. The most expensive step in this computation is to find the necessary amount of dissipation; since we have four viscosity coefficients we have a four-dimensional parameter space that has to be checked for the smallest combination of $\alpha_1, \dots, \alpha_4$ needed for a stable evolution. Experience shows that one can start with a rather high prediction for these coefficients and then successively lower them as far as possible. With a low resolution of 50×40 gridpoints we check the first 3 milliseconds of an evolution for the occurrence of instabilities and adjust the viscosity parameters if necessary. This procedure is repeatedly applied until a further decrease in the amplitudes of the dissipation coefficients would destroy the stability. However it turned out that there is not a very strong dependence of the eigenmode frequencies on the amount of artificial viscosity used. Once the optimum coefficients were found using the procedure described above we could generically use up to 5 times higher dissipation without observing a significant change in the oscillation frequencies. Of course the higher the dissipation the stronger the solutions are being damped which will result in a broadening of the frequency peaks in the Fourier transform. The crucial point here is that the peaks itself practically only change within their error bounds which shows us that we don't have to exactly pinpoint a certain set of viscosity coefficients in order to get reliable results within this approach.
According to Figures 3.6 and 3.7 the following Figure 3.8 shows again snapshots of the time evolution of an initial Gaussian velocity perturbation on the ρ-component of the 4-velocity. The last two pictures are taken from a very late stage of the time evolution and still the code runs very stable; typical evolution times are around 50 milliseconds. Since the perturbation we applied is not an eigenmode, we expect that several modes were excited by this particular choice of initial condition. The corresponding oscillation pattern therefore will not look like a simple sinusoidal waveform but will feature a more complex shape. This is somewhat different from the way these studies usually are performed; generally we will use approximations of particular eigenfunctions to excite only this specific mode. The method shown here is for demonstration purposes only. Figure 3.9 shows in the left panel the real part of the complex solution of the time evolution equations(2.39)-(2.42) for $m = 0$.

In fact, in this case the system stays real when starting with purely real initial data as already mentioned in 2.5.2. The complete evolution interval mounted up to 50 milliseconds and was covered by roughly 10^5 timesteps. As expected the waveform looks rather intricate, indicating that a huge number of modes is excited by the Gaussian initial perturbation. The right panel shows the corresponding power spectral density or more specifically its logarithm and confirms this observation. Over a dozen different frequencies can be identified

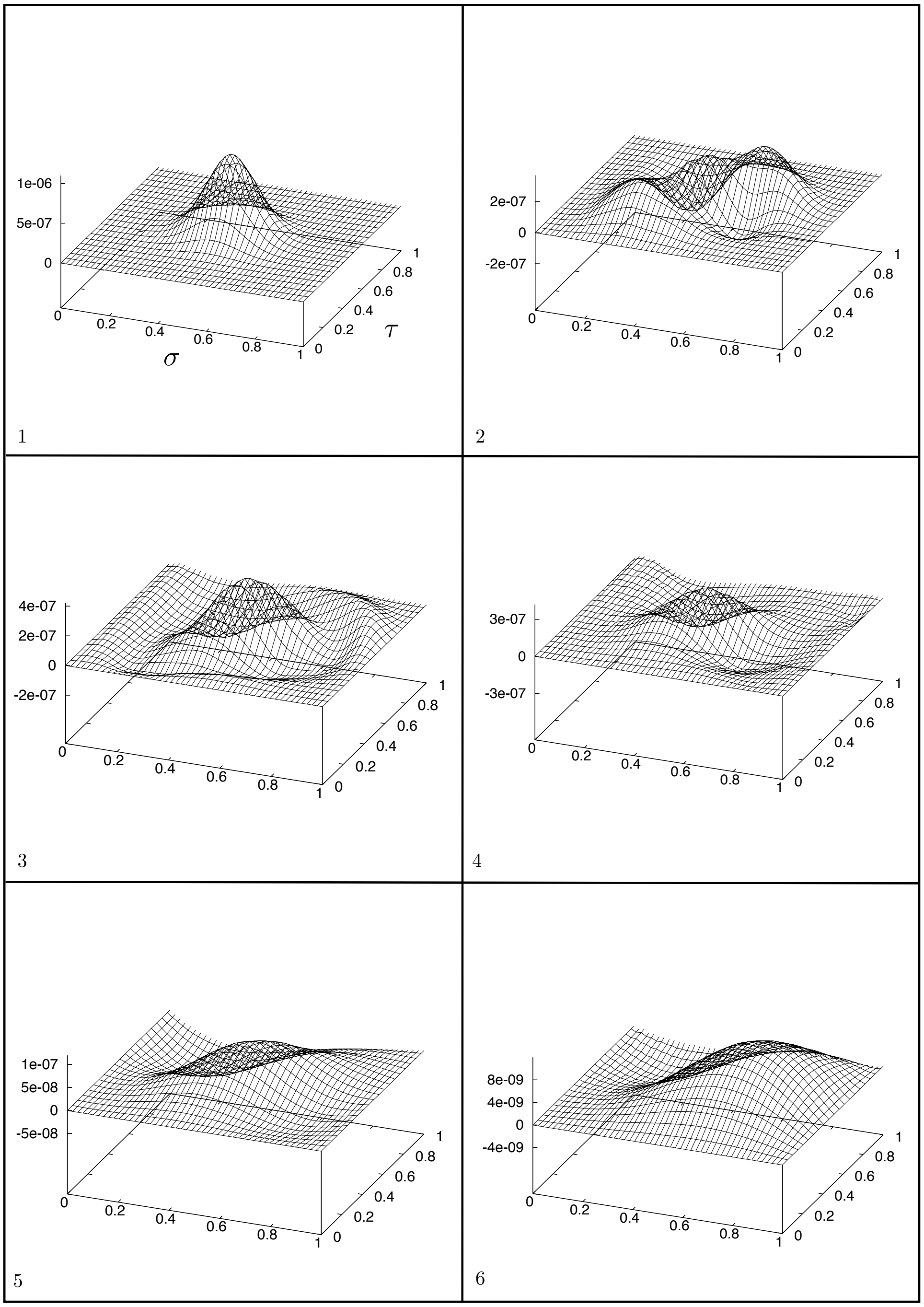

Figure 3.8: Snapshots of the u_ρ-time evolution with additional artificial viscosity; the numbers label the temporal order

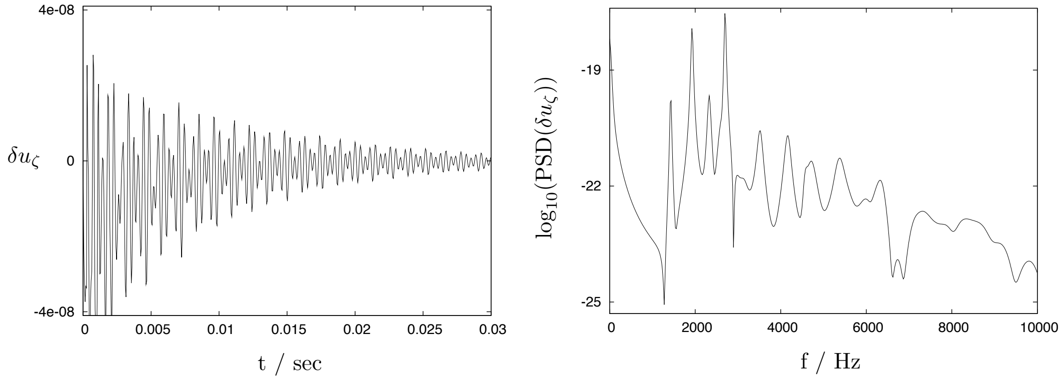

3.9.1: Section of the time series for δu_ζ

3.9.2: Power spectral density of the time series

Figure 3.9: Time evolution of δu_ζ and corresponding frequency analysis for a Gaussian perturbation on δu_ρ

immediately; the most strongest at 2.7 kHz belongs to the fundamental quasi-radial oscillation mode, the so-called F-mode and we will discuss our results in more detail in the next chapter.

Finally we were able to provide a stable numerical algorithm for solving the linearized perturbation equations derived in Chapter 2. After appropriately extending the computational domain supplied by the background code we solve the system (2.39)-(2.42) by an iterated Crank-Nicholson scheme with unequal weights and an explicit dissipation operator of Kreiss-Oliger type.

Before we present the code comparison results we will briefly review the way we are obtaining the frequency spectrum, compute its peaks and use this information for a method called *mode recycling*.

3.9 Post-Processing Routines

3.9.1 Discrete Fourier Transforms and Data Windowing

After a successful time evolution we take the real part of the complex data and want to extract the mode frequencies. For a continuous time-series $h(t)$ its corresponding Fourier representation $H(f)$ is given by

$$H(f) = \int_{-\infty}^{\infty} h(t) e^{2\pi i f t} dt \tag{3.29}$$

The total power of the signal can be computed in both of this views because we have

$$P_t = \int_{-\infty}^{\infty} |h(t)|^2 dt = \int_{-\infty}^{\infty} |H(f)|^2 df$$

We will be more interested in how strong a specific mode at a given frequency is, that is we want to know the power contained in a narrow frequency range. For this reason one defines the one-sided power spectral density (we will often write PSD for it) as

$$P_h(f) = |H(-f)|^2 + |H(f)|^2 \qquad 0 < f < \infty \tag{3.30}$$

For a purely real time-series we also have $H(-f) = H(f)^*$ so in this case it is $P_h(f) = 2|H(f)|^2$.
Now our signal is discrete; it is sampled at multiples of the chosen timestep Δt. Of course we don't have to sample the signal after every timestep; especially for simulations with a very high spatial resolution we need a rather small Δt in order to satisfy the Courant condition for numerical stability. It would be impractical to store the data after every timestep because the amount of memory needed is too much; usually it suffices to sample every 100 timesteps or so. We will denote our actual sampling interval with δt in this section so normally we have $\delta t \approx 100\Delta t$. The real part of our numerical solution then is given at the temporal points

$$h_n = h(n\delta t) \qquad n = 0, 1, \ldots, N-1$$

Suppose now a situation depicted in the following Figure 3.10 where we have three sampling points $\delta t_i, i \in \{0, 1, 2\}$ and two oscillation modes. The signal function drawn solid in the figure takes its extreme points at the sampling points during one wavelength λ; when we denote the signal speed with c_s we have

$$2c_s\delta t = \lambda$$

The corresponding frequency is then given by

$$f_c = \frac{1}{2\delta t} \tag{3.31}$$

and is called the Nyquist-frequency. Due to the finite temporal resolution of the time-series, this is the highest frequency we are able to identify in h_n. All of the power spectral density that lies outside of the range $f < f_c$ is falsely aliased into that range. The time-series with a higher frequency drawn dotted in Figure 3.10 is an example of this aliasing effect. At the three discrete sampling points it takes the same values as the solid curve so just from looking at the time-series h_n we are not able to distinguish between these two oscillation modes. This also means that in these cases the power spectral density near the Nyquist frequency will contain contributions of all the aliased modes as well. A simple check would then to determine whether the PSD approaches zero as the frequency approaches f_c; if not there is a certain probability that modes outside the critical range have been aliased back into this range. On the other hand, if the continuous time-signal $h(t)$ is bandwidth-limited,

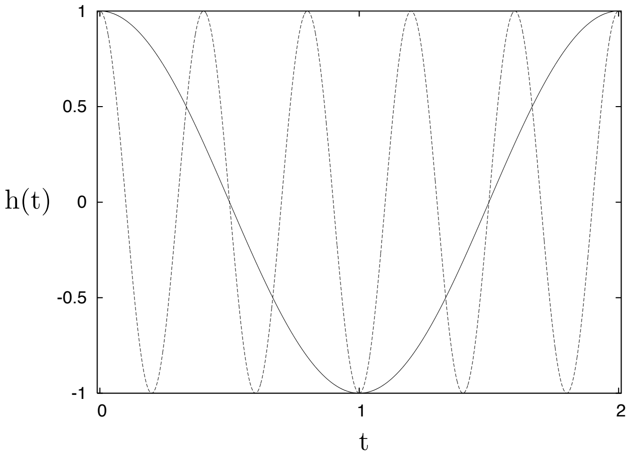

Figure 3.10: Example of aliasing effects for oscillations with a frequency higher than the critical Nyquist-frequency

i.e. $H(f) = 0$ for $f > f_c$ then the sampling theorem states that $h(t)$ is already completely determined by its samples and we have (see [70] for example)

$$h(t) = \delta t \sum_{n=0}^{\infty} \frac{\sin(2\pi f_c(t - n\delta t))}{\pi(t - n\delta t)}$$

We now have to find a discrete version of equation (3.29). In the continuous case the frequency goes from $-\infty$ to $+\infty$ and we have just seen that in the discrete case the Nyquist frequency f_c is the critical limit. If the time-series h_n takes N values we discretize the interval $\mathcal{I}_t = [-f_c, +f_c]$ evenly into

$$f_k = \frac{k}{N\delta t} \qquad k = -\frac{N}{2}, \ldots, \frac{N}{2} \tag{3.32}$$

This are actually $N + 1$ numbers but we will see that two of them are not independent. We then discretize equation (3.29) by

$$H(f_k) = \int_{-\infty}^{\infty} h(t) e^{2\pi i f_k t} dt \approx \delta t \sum_{n=0}^{N-1} h_n e^{2\pi i f_k t_n} = \delta t \sum_{n=0}^{N-1} h_n e^{2\pi i n k/N}$$

and write

$$H(f_k) = \delta t H_k \qquad \text{with} \qquad H_k = \sum_{n=0}^{N-1} h_n e^{2\pi i n k/N} \tag{3.33}$$

Since $H_{N-k} = H_{-k}$ we also have $H_{N/2} = H_{-N/2}$ and therefore only N independent values. It is convenient to vary k also from 0 to $N - 1$; with this choice we then have positive frequencies for $1 \leq k \leq N/2-1$ and negative frequencies for $N/2+1 \leq k \leq N-1$. The zero frequency is for $k=0$ and $k=N/2$ corresponds to both $+f_c$ and $-f_c$. The one-sided PSD is defined accordingly to its continuous counterpart as

$$\begin{aligned} P(0) &= \frac{1}{N^2}|H_0|^2 \\ P(f_k) &= \frac{1}{N^2}(|H_k|^2+|H_{N-k}|^2) \qquad k=1,\ldots,\frac{N}{2}-1 \\ P(f_c) &= \frac{1}{N^2}|H_{N/2}|^2 \end{aligned} \tag{3.34}$$

The discrete Fourier transforms that have to be performed on various datasets are implemented using the free FFTW library [71] which uses some of the worlds fastest routines for computing the frequency representation of a given time-series h_n. The Fourier decomposition is of course not the bottleneck of our code but especially for applying the mode recycling technique which we will describe later we have to perform a frequency analysis for every gridpoint of the computational domain. In special cases this amounts to $1.3 \cdot 10^5$ single Fourier transforms, each with roughly 10^6 datapoints to process.
The next point to address is how accurate equation (3.34) approximates the continuous version (3.30) for the power spectral density. We can not expect for $P(f_k)$ to be exactly equal to the continuous $P_h(f)$ for $f=f_k$; rather it will be some average of $P_h(f)$ over an interval centered at f_k and extending to both sides of this frequency. This also means that we will have some leakage of the signal into neighbouring frequency bins and in fact a simple argument gives us the weighting or window function in this case. Consider an infinitely sampled signal h_n which we multiply by the unity window function during the total sampling time $N\delta t$. By the convolution theorem, the Fourier transform of a product of function in just the convolution of both separate Fourier transforms and for the unity window function we have

$$\sum_{n=0}^{N-1} e^{2\pi i s k/N} = \frac{\sin(\pi s)}{\sin(\pi s/N)}$$

The PSD is determined by taking the square of the Fourier transform and normalize it by the total number of data points; we therefore arrive at the window function for the discrete power spectral density

$$W(s) = \frac{1}{N^2}\left|\frac{\sin(\pi s)}{\sin(\pi s/N)}\right|^2$$

where s is the frequency offset in bins. As one can see, $w(s)$ shows on oscillatory behaviour and leaks a significant part of the signal even for high offsets s. The reason for this is of course the highly discontinuous behaviour of the unity step-function which Fourier transform hence has also high frequency components. The whole purpose of data windowing is to find another functional form of the window functions which changes more smoothly from zero to a maximum value and then back to zero during the total sampling time and therefore substantially cutting down the high frequency leakage in its Fourier transform. In the literature (see [70] for example) one can find several examples of such window functions;

popular choices are

$$\begin{aligned} w_j &= 1 - \left| \frac{j - 1/2N}{1/2N} \right| && \text{Bartlett window function} \\ w_j &= \frac{1}{2}\left(1 - \cos\left(\frac{2\pi j}{N}\right)\right) && \text{Hann window function} \\ w_j &= 1 - \left(\frac{j - 1/2N}{1/2N}\right)^2 && \text{Welch window function} \end{aligned}$$

Instead of calculating $H(f_k)$ with H_k defined in (3.33) we now use

$$H_k = \sum_{n=0}^{N-1} h_n w_n e^{2\pi i n k/N}$$

with some weight function w_n. From a practical point of view there is only little difference in choosing one window function over the other; the corresponding power spectral density plots are virtually identical. The following Figure 3.11 compares the common choices for w_n with the unity step function one effectively uses without any data windowing.

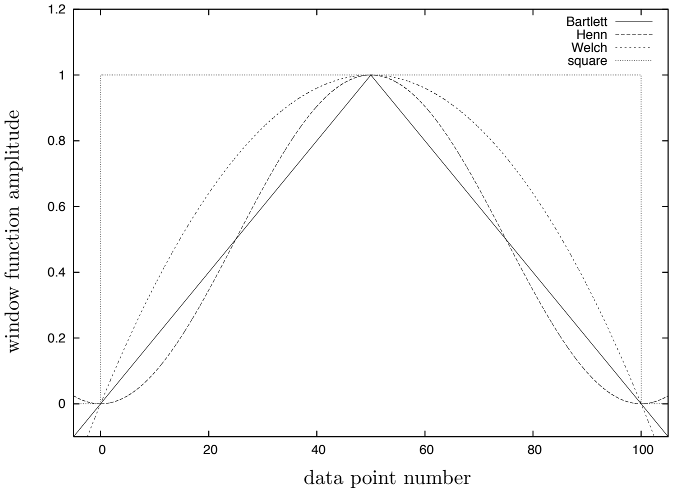

Figure 3.11: The most popular choices of window functions compared to the unity step function for $N = 100$ data points

For the post-processing routines in this thesis we use the Welch function to modify the sampled data. However, this is not a tight restriction and can be changed at any time.

3.9.2 Peak Localization and Mode Recycling

By determining the location of frequency peaks in the power spectral density graphs we are limited by the sampling time δt. According to equation (3.32) the frequency resolution is given by

$$\Delta f = \frac{1}{N\delta t}$$

One can therefore refine the frequency resolution by either using more samples, i.e. increasing N, or by using a higher sampling interval δt. Of course, the latter choice will also affect the critical Nyquist frequency f_c in a way that a better resolution is achieved but only in a very narrow low frequency range; see equation (3.31). So generally we will use longer evolution time to increase the resolution; in particular for the low-frequency inertial modes these longer evolution times are needed in order to obtain an appropriate number of oscillation cycles for a proper frequency peak analysis. Probably the most obvious way of implementing such a peak finding algorithm is to monitor the difference in Fourier amplitude of two adjacent grid-points in the frequency space. If we denote the amplitude of the PSD at a given frequency f_k with $P(f_k)$ then the task is to look for a change in sign of $P(f_{i+1}) - P(f_i),\ i = 0, \ldots, N-1$. This value will be positive when approaching a peak and gets negative when moving away from it; we therefore can pinpoint a local maximum of the PSD to a specific discrete frequency gridpoint $f_k,\ k \in \{0, \ldots, N-1\}$. We can improve this scheme by using first-order finite-difference approximations for derivatives of the power spectral density. If f_k denotes the frequency of a peak determined by searching for a sign change as described above, we can use $(P(f_{k-1}) - P(f_k)/\Delta f$ as an approximation for dP/df at $f = f_{k-1}$ and correspondingly $(P(f_{k+1}) - P(f_k)/\Delta f$ as an estimate for dP/df at $f = f_{k+1}$. For a peak of the PSD, the derivative with respect to the frequency has to vanish and we can simply perform a linear interpolation on the numerically obtained derivatives to find this point. In the case of $P(f_{k-1}) = P(f_{k+1})$ this scheme will provide the expected result, i.e. a peak at $f = f_c$; for all other cases it will give a more accurate estimation of the peak location than the previously presented routine.

With this algorithm implemented in our code we can finally tackle the unintentional excitation of additional modes during time evolution. The standard approach for the simulations will be to put in a trial eigenfunction as initial data and let it evolve in time. Since we were not starting with an exact eigenmode of the system the corresponding power spectral density recorded at an arbitrary point in the interior of the star will typically consist of a main peak, representing the dominant oscillation mode of this run, and several smaller subpeaks. Especially when going to very high rotation rates it gets difficult to track a specific frequency peak as the various amplitudes and locations change. It is therefore desirable to find a mechanism which will suppress unwanted modes and enhance other modes of particular interest; this mechanism is called *mode recycling*. Since for a given oscillation mode, the amplitude of its Fourier transform correlates with its eigenfunction one has to take the power spectral density not only at a single point of the computational domain but at many points and track the behaviour of the PSD amplitude at a given mode frequency, see [40]. A simple example may illustrate this. Consider a one-dimensional string that is fixed at its ends and oscillates with a specific eigenfrequency. One then puts observers at different locations in space to record the time evolution of amplitude and perform a Fourier transformation. At the nodes of the oscillations, the observer would see no oscillation at all so the amplitude of the Fourier transform is zero there as well. In contrast to this at the lobes of the oscillation pattern the observer would record a very high Fourier amplitude at the specific eigenfrequency and this amplitude will of course decrease towards the nodes. With this technique one can extract the eigenfunctions of oscillation modes and put it back as initial data in a new simulation.

Since one no longer uses a trial eigenfunction, other modes will usually be suppressed by several orders of magnitude and typically this procedure is repeated two or three times. We also will use it frequently first of all to demonstrate that mode recycling works in our case as well and then to damp ambiguous modes especially at high rotation rates.

4

Results

After we implemented a stable evolution code we have to validate its results against published work in order to see if we can reproduce it. Our work will be pointless if the algorithm we implemented is stable but does not confirm the findings of other publications. We mainly will compare our results with the work published in [72] and [52]. In [72] a non-linear relativistic hydrodynamics code is used to study axisymmetric modes of relativistic stars in the Cowling approximation while in [52] also the spacetime is taken into account by a conformal flatness approach. Both papers use the same series of background models to put the perturbations on so we will briefly review them here.

4.1 The Background Models

For polytropic equations of state of the form (2.17) it is convenient to work in gravitational units; i.e. where $G = c = 1$. There, the dimension of $K^{N/2}$ is length so it can be used to set the fundamental length scale of the system and to define dimensionless quantities; see for example [73], [74]. We then have for instance

$$\begin{aligned} \bar{M} &= K^{-N/2} M \quad \text{for mass} \\ \bar{R} &= K^{-N/2} R \quad \text{for radius} \\ \bar{\rho} &= K^{N} \rho \quad \text{for rest-mass density} \end{aligned}$$

Setting also the solar mass $M_\odot$ to zero will already turn K into a dimensionless scaling factor and the BU background model series used in [72] and [52] is defined as a sequence with $\Gamma = 2$, $K = 100$ and a fixed central rest-mass density of $\rho_c = 1.28 \cdot 10^{-3}$ in these units. In the conventional cgs-system this means a rest-mass density of $\rho_c = 0.79 \cdot 10^{15}$ g/cm^3 and a corresponding energy density of $\epsilon_c = 0.891 \cdot 10^{15}$ g/cm^3. In the nonrotating limit this leads to a stellar model with a gravitational mass of $M = 1.4\ M_\odot$ and a radius of $R = 14.16$ km and is labelled as BU0. Starting from there the angular velocity is subsequently increased in a way that the ratio of polar to equatorial radius r_p/r_e decreases by a constant factor of 0.05 for every new equilibrium configuration until the Kepler limit is reached. This will happen for $r_p/r_e = 0.58$ and model BU9; increasing the angular velocity even more will not lead to a stable equilibrium and the star will eventually be torn apart by centrifugal forces. In the following Table 4.1 we give an overview about several stellar parameters; here M is the gravitational mass and R the equatorial circumferential radius. One can see that the higher the rotation rate for fixed central rest-mass density the higher the gravitational mass of the equilibrium configuration.

model	Ω (kHz)	r_p/r_e	M ($M_\odot$)	R_e (km)
BU0	0.0	1.0	1.4	14.16
BU1	2.182	0.95	1.43	14.52
BU2	3.062	0.9	1.47	14.92
BU3	3.712	0.85	1.5	15.39
BU4	4.229	0.8	1.54	15.91
BU5	4.647	0.75	1.59	16.53
BU6	4.976	0.7	1.63	17.27
BU7	5.214	0.65	1.67	18.16
BU8	5.344	0.6	1.69	19.29
BU9	5.361	0.58	1.7	19.96

Table 4.1: BU model parameters

This is of course due to the fact that the centrifugal force supports the pressure against the gravitational pull so that higher masses can be achieved for rotation than in the nonrotating case. Figure 4.1 shows the mass-radius relationship for all rotation rates listed in the second column of Table 4.1. The sequence starts with zero angular velocity for the most left curve and terminates with the Kepler velocity on the far right; the dots represent the actual BU models from the first column of this table.

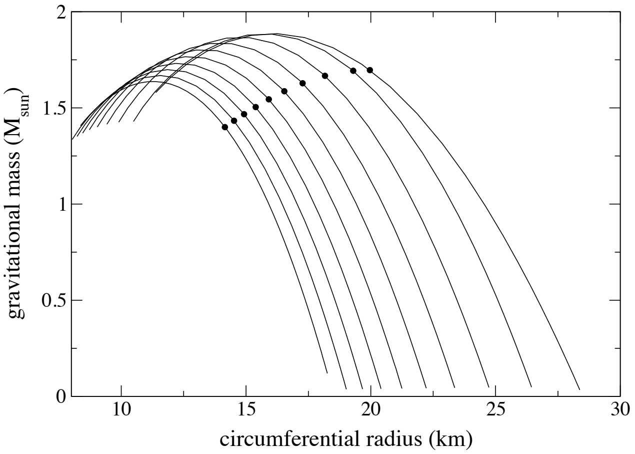

Figure 4.1: Mass-Radius diagrams for different rotation rates; the dots represent the actual BU models

Initially one can start with a very low mass and then follow the mass-radius curve up to the maximum mass M_{max} for this rotation rate. Going further would reduce the mass again as one can see from the figure but while models on these sections of the curve are still solutions of the equilibrium equations they are unstable to radial perturbations. The slightest displacement would either lead to a collapse or to a expansion of the star unless a stable equilibrium is reached. This is the reason why all the background configurations have larger radii than their corresponding $M = M_{max}$-model.

From a numerical point of view experience shows that a rather small number of Chebyshev polynomials is needed to generate very accurate equilibrium configurations. The accuracy can be either checked by monitoring general relativistic generalizations of virial theorems (see [75]) or by a comparison of different methods for obtaining mass and angular momentum that have to yield identical results. The mass for example can be calculated by observing a specific metric potential at infinity (we call this mass M_a) and alternatively by an integration of metric and fluid variables in the interior of the compact object (labelled as M_i). With a resolution of 18×18 gridpoints in $\mathcal{D}_+$ (see Section 3.3 for reference) we already achieve an accuracy of

$$\left|1 - \frac{M_i}{M_a}\right| = 3.8 \cdot 10^{-13} \quad \text{and} \quad \left|1 - \frac{J_i}{J_a}\right| = 3.5 \cdot 10^{-9}$$

for the angular momentum. We therefore chose this resolution as default value for our background model generation.

4.2 First Axisymmetric Validation Runs

Since we do not know the correct eigenfunction of a pressure mode in advance, we have to start with a trial perturbation that typically will also excite various other modes. Depending on how accurate the first guess was the eigenfunction of the dominant mode will come very close to the shape of the initial approximation. If the corresponding peak in the power spectral density is too broad one can use successive mode-recycling runs to suppress the additional modes and to sharpen the frequency peak of the strongest mode. For exciting axisymmetric ($m = 0$) modes we will perturb the equilibrium rest-mass density according to

$$\delta\rho = A\rho_c \sin\left(\frac{\pi r}{r_s(\theta)}\right) \tag{4.1}$$

where A is the perturbation amplitude (typically around 10^{-3}), (r, θ) denote spherical coordinates and $r_s(\theta)$ is the coordinate radius of the star (which is not independent of θ when the star is rotating). Since we use pressure or energy density as perturbation variable we also have

$$\delta p = \frac{\Gamma p}{\rho}\delta\rho$$

for polytropic EoS. A graphical representation of this type of initial data can be seen in Figure 4.2

As already extensively discussed in Section 3.3, σ can be interpreted as radial coordinate while τ corresponds to the θ-coordinate in a spherical system. The initial perturbation described by equation (4.1) shows a $l = 0$-characteristics since for a given σ the perturbation amplitude is independent of τ. All of the simulations in this thesis are performed with a

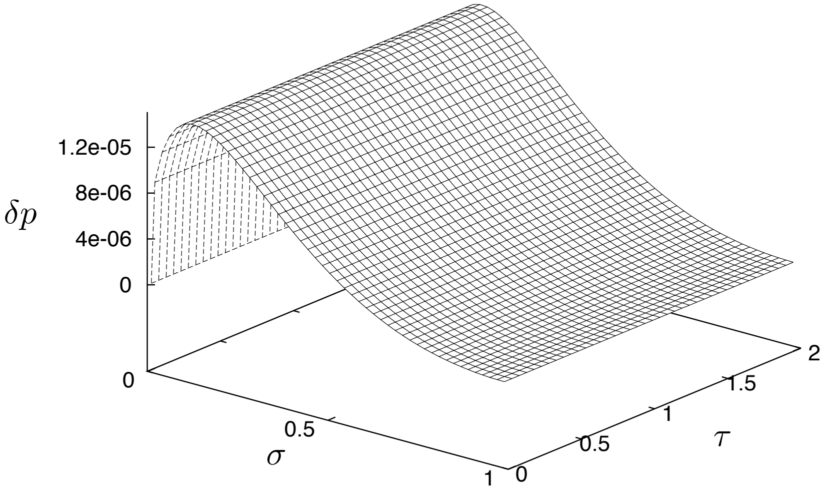

Figure 4.2: Axisymmetric initial pressure perturbation for the BU0 model

grid-resolution of 200 × 160; additionally several other resolutions like 50 × 40, 75 × 60, 100 × 80 and 400 × 320 were also used, mostly for convergence tests. However, it turned out that the most dramatic improvement in the frequencies was obtained when going from the lowest resolution to the medium one with 100×80 gridpoints. Increasing the number of nodes in the computational domain beyond these numbers will generally also improve the accuracy of the mode frequencies but not as rigorously as before. We can take this as an indication, that a grid resolution of 200 × 160 is sufficient to determine the characteristic oscillation frequencies to an admissible accuracy. A section of such a test run is depicted in Figure 4.3. The complete simulation is stable for at least 50 ms but we only show here the first 20 milliseconds. We also write δp and δu_ζ for the perturbation variables that are presented in the figures of this thesis (e.g see figures 4.2 and 4.3 for example) but what is really shown there are the modified time evolution quantities we introduced in Section 2.5.1; see equations (2.26)-(2.29) and (2.35)-(2.38). For simplicity we will stay with this notation; the eigenfrequencies of oscillation modes are not altered when multiplying a perturbation variable with a function that is constant in time. One though has to bear in mind that the eigenfunctions we will present here are the eigenfunctions of the modified evolution quantities, although we will still label them with δu_ζ instead of the correct f_2 in this example.

The time-series recorded in Figure 4.3 is taken at the point $\mathcal{P} = (\sigma_0, \tau_0) = (0.5, 0.5)$ inside the computational domain and for all simulations in this thesis $\mathcal{P}$ is the default location for the extraction of data. For a real eigenmode the oscillation frequency has of course to be independent of the data extraction point and this has also been tested. The easiest way to check this is to compute the actual eigenfunction of this mode as a first preparatory step for a mode recycling run.

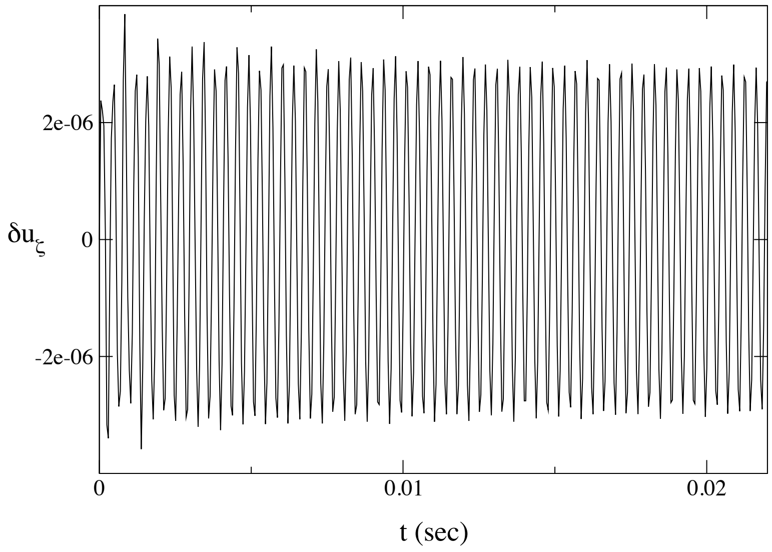

Figure 4.3: Time-evolution of δu_ζ for a nonrotating BU star and an initial $m = 0$ pressure perturbation

If the frequency of a given mode changes significantly throughout the star, the corresponding eigenfunction will show strong discontinuities; for all the results presented here, this behaviour can be excluded. As already mentioned earlier, a typical simulation will cover a time interval of roughly 50 ms. For the high resolution of 200 × 160 gridpoints approximately 2×10^5 timesteps are needed for this evolution and every 200 timesteps the updated perturbation quantities were saved to a file for post-processing. Hence the actual timestep is given by $\Delta t \approx 5 \times 10^{-5}$ sec and we usually have a frequency resolution of $\Delta f \approx 20$ Hz and a Nyquist frequency of $f_c \approx 10^4$ Hz. We explained in Section 3.8 that we had to include Kreiss-Oliger like dissipation terms in order to get the numerical implementation stable over a certain period of time. We chose four independent viscosity coefficients for each of the perturbation equations and tried to make them as small as possible while still maintaining a stable evolution scheme. Based on experience, the actual value of the dissipation coefficients depends on at least two parameters. First of all when increasing the rotation frequency of the background star one usually has to increase the artificial viscosity as well. Typical values are one order of magnitude when going from no rotation to the Kepler limit. Second, increasing the resolution of the simulation in many cases leads to a decrease in the amount of additional viscosity needed for a stable evolution. This time however the dependence is

not so strong as in the previous case, one can usually lower the coefficients by $60-70\%$. For the nonrotating BU0 model we discuss so far, the dissipation coefficients fall in the range of $\alpha_i \approx 10^{-4}$, $i = 1, \ldots 4$.
The following Figure 4.4 shows the power spectral density of the time series presented in Figure 4.3. For better visibility of the various oscillation modes actually the logarithm of the PSD was taken and one can clearly see different frequency peaks in this spectrum.

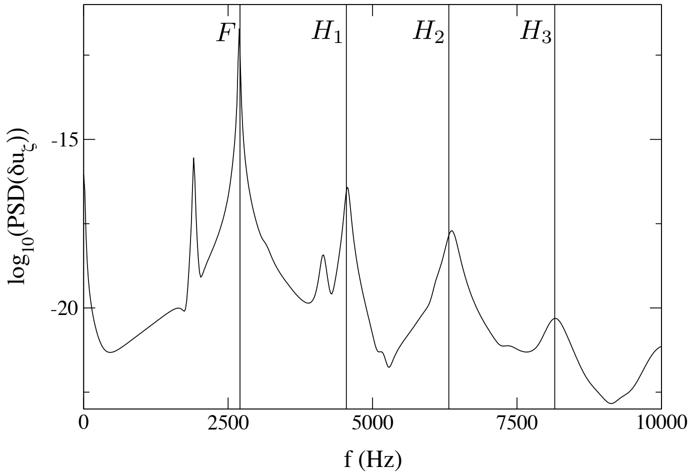

Figure 4.4: Logarithm of the power spectral density for the δu_ζ oscillation

The most dominant one at $f = 2.706$ kHz belongs to the fundamental quasi-radial oscillation mode (F-mode) with no nodes of the corresponding eigenfunction in the radial direction. Alongside, several other modes were excited as well; this is due to the fact that we started with a trial eigenfunction of the form (4.1). However, the second most strongest mode is already three orders of magnitude weaker than the F-mode. The vertical lines in Figure 4.4 denote the reference values from [72] of the fundamental mode and its first three overtones. The eigenfunctions of overtones show the same angular behaviour as the fundamental mode but in contrast to the F-mode they exhibit nodes in the radial direction. The corresponding eigenfrequencies can be roughly approximated by an integer multiple of the fundamental frequency. As one can see from the figure the frequencies we found in the nonrotating case agree very well with the literature values; more specifically

$$\begin{array}{rclllll} f^F_{ref} & = & 2.706\,\mathrm{kHz} & f^{H_1}_{ref} = 4.547\,\mathrm{kHz} & f^{H_2}_{ref} = 6.320\,\mathrm{kHz} & f^{H_3}_{ref} = 8.153\,\mathrm{kHz} \\ f^F & = & 2.679\,\mathrm{kHz} & f^{H_1} = 4.561\,\mathrm{kHz} & f^{H_2} = 6.380\,\mathrm{kHz} & f^{H_3} = 8.178\,\mathrm{kHz} \end{array}$$

where the first line denotes the reference values and the second line shows our results; the errors are less than 1%. To test the mode recycling module we developed, the Fourier amplitude of the F-mode and its first three overtones was extracted from all gridpoints of the computational domain. As explained in subsection 3.9.2 the amplitude traces the shape of the eigenfunction so one should actually see whether H_1, H_2 and H_3 are really the overtones of the fundamental mode. The result of such an extraction is depicted in the following Figure 4.5 where the amplitude is colour-coded and projected onto the computational domain.

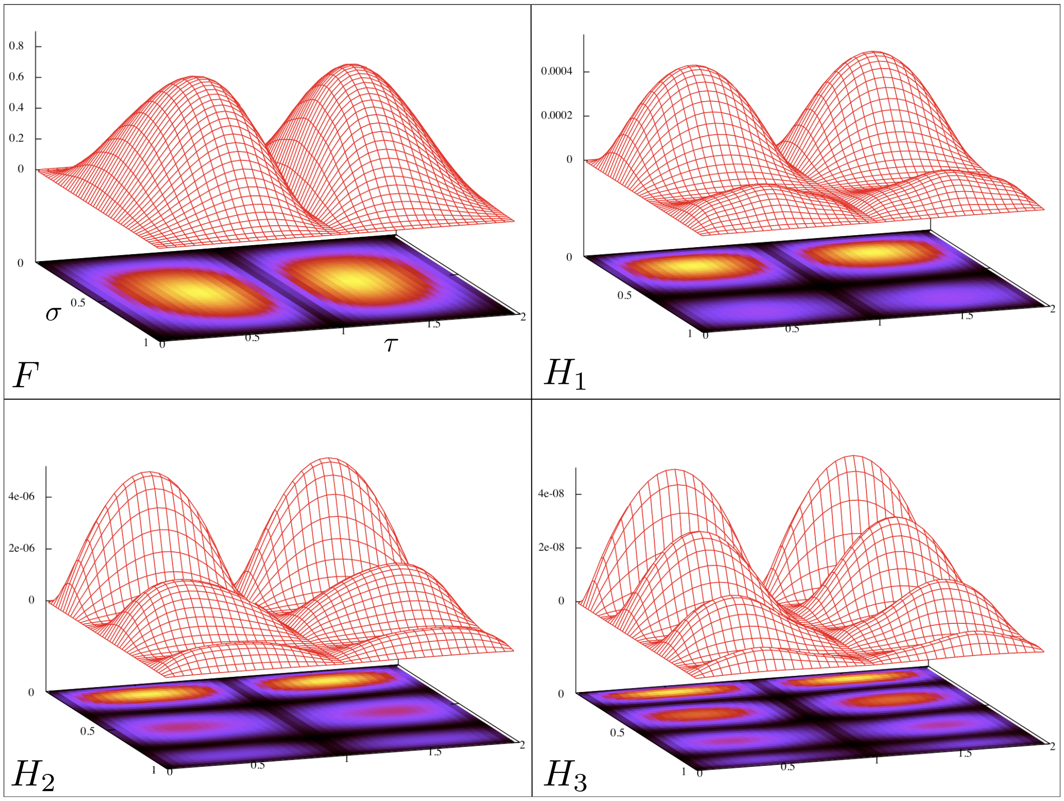

Figure 4.5: Spatial variation of the Fourier amplitude for the fundamental mode and its first three overtones extracted from δu_ζ in the nonrotating case

Indeed one can see very clear that the number of nodes in the radial direction increases with higher overtones (keep in mind that the grid variable σ can be interpreted as a radial coordinate which varies from $\sigma = 0$ at the center of the star to $\sigma = 1$ at the surface). One point worth mentioning here is that the angular dependence of the eigenfunctions in Figure 4.5 is quite different from the angular behaviour in Figure 4.2 although they both describe a spherically symmetric ($l = 0$, $m = 0$)-perturbation. The explanation is quite simple: First of all, Figure 4.2 depicts a scalar perturbation and moving along a $\sigma = const.$-line there shows immediately that this is a $l = 0$-perturbation. In contrast to this, Figure 4.5 shows a vector perturbation; even if the spherical harmonic $Y_0^0(r, \theta)$ is a constant we have to transform it into our cylindrical coordinate system. For a purely radial perturbation of the 4-velocity we expect a modulation of $\sin\theta$ for δu_ρ and $\cos\theta$ for δu_ζ. Second, according to the boundary conditions we derived for the rotation axis (see Table 2.1) the perturbation variable δu_ζ is always equal to zero along $\rho = 0$. Taking these two points into account, one concludes that the shape of the eigenfunctions in Figure 4.5 is in fact in agreement with an ($l = 0$, $m = 0$)-perturbation. The maximum amplitude of the eigenfunctions depicted there also shows their relative strength in the time-series of Figure 4.4. The F-mode is the strongest one with a normalized amplitude of roughly 1. Already three orders of magnitude less powerful, the first overtone H_1 can be identified in the data. The H_2-mode is again weaker by a factor of 100 and the part of the time-series which is due to the H_3-mode is once more a hundred times weaker.

There are still some unidentified frequency peaks left over in Figure 4.4, most notably the second most strongest one at roughly 1.9 kHz and a minor one near 4.1 kHz. Since we already demonstrated the reliability of the Fourier amplitude extraction technique that was used to correctly identify the F-mode overtones, we now apply the very same algorithm to the yet unknown peak at 1.9 kHz. Figure 4.6 shows the energy-density eigenfunction obtained from this procedure. Again the amplitude is colour-coded and one can clearly see that this perturbation is no longer independent of the polar angle θ, i.e. of τ in terms of the numerical domain.

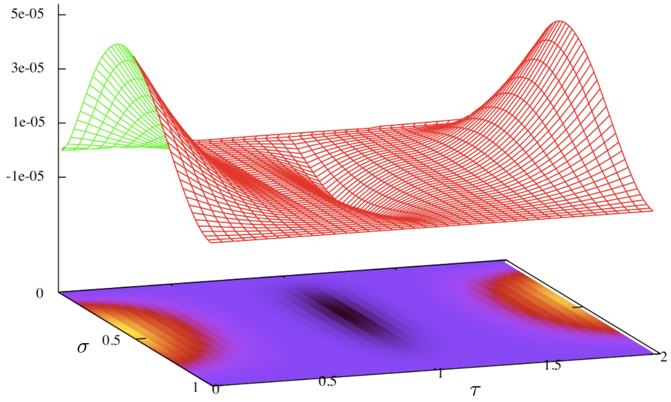

Figure 4.6: Eigenfunction of $\delta\epsilon$ for the frequency peak at 1.9 kHz

Figure 4.6 shows a scalar perturbation so there is no confusion about transforming a vector quantity from spherical to cylindrical coordinates (see the above discussion). The energy-density perturbation has a maximum value along the rotation axis ($\rho = 0, \zeta > 0$), then goes through a minimum along the equatorial plane and again reaches a maximum along the parts of the rotation axis which are below the equatorial plane, i.e. ($\rho = 0, \zeta < 0$). The only spherical harmonic function that matches this behaviour is $Y_2^0 \sim (3\cos^2\theta - 1)$ so the depicted eigenfunction features a ($l = 2$, $m = 0$) characteristic and indeed can be identified with the fundamental axisymmetric quadrupolar oscillation, the ${}^2f$-mode. Since we already extracted the eigenfunction we can put it back as initial data for a second run;

this is what mode-recycling is all about. As discussed in Section 3.9.2 one expects to enhance this specific modes and to suppress the others. The following Figure 4.7 shows the power spectral density of a simulation with an initial energy-density perturbation that resembles the ${}^2f$-mode eigenfunction.

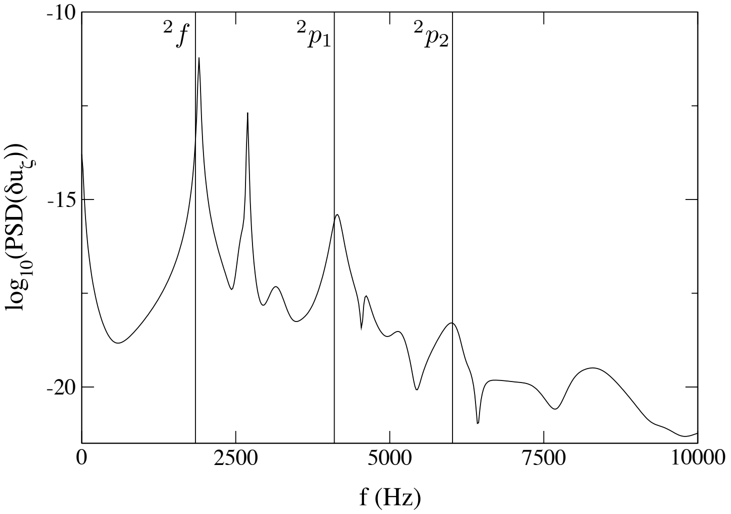

Figure 4.7: Logarithm of the power spectral density for the ${}^2f$-mode recycling run

As one can see there, the oscillation at 1.9 kHz is now considerably enhanced. We still have contributions from other modes as well but the second most dominant one which is the fundamental F-mode this time is weaker by a factor of 100. Again, the vertical lines denote literature values for several oscillation patterns like the ${}^2f$-mode and its first two overtones; the direct comparison yields

$$\begin{aligned} f_{ref}^{^2f} &= 1.846\,\mathrm{kHz} \qquad f_{ref}^{^2p_1} = 4.100\,\mathrm{kHz} \qquad f_{ref}^{^2p_2} = 6.019\,\mathrm{kHz} \\ f^{^2f} &= 1.890\,\mathrm{kHz} \qquad f^{^2p_1} = 4.130\,\mathrm{kHz} \qquad f^{^2p_2} = 6.007\,\mathrm{kHz} \end{aligned}$$

This time the errors are less than 2.4% with the largest deviation for the fundamental quadrupolar mode. Again we can ask for the shape of the eigenfunctions belonging to the overtones of the ${}^2f$ oscillation; similar to what we have done in the quasi-radial case (see discussion above) we expect to see an increasing number of nodes in the radial direction. Figure 4.8 shows the result of a Fourier amplitude tracking over the complete computational domain, locked onto the ${}^2p_1$- and ${}^2p_2$-frequency. We can see that the angular dependence is the same as for the ${}^2f$-mode which shows that indeed the overtones also belong to an ($l = 2$, $m = 0$) perturbation. However in contrast to the fundamental mode radial nodes appear for the high order harmonics; one for the ${}^2p_1$-mode and two for the second overtone. In reality these additional features were present but very small so that they were not visible on the scale of Figure 4.8; we enhanced them artificially in this plot.

The output of our simulations presented up to now are for a nonrotating BU star so far and already very promising. We demonstrated that we are able to reproduce published results in the literature to a very good accuracy.

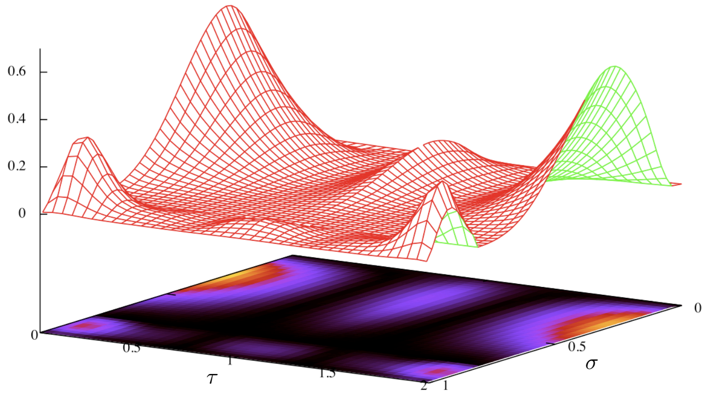

4.8.1: Shape of the ${}^2p_1$ eigenfunction

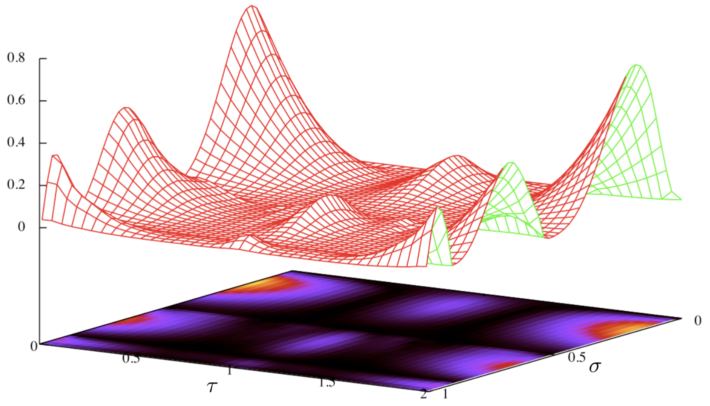

4.8.2: Shape of the ${}^2p_2$ eigenfunction

Figure 4.8: Spatial variation of the energy-density Fourier amplitude for the quadrupolar overtones

The mode recycling algorithm and, as a preparatory step, the tracing of the eigenfunction for a given frequency works excellent and is a helpful tool to identify ambiguous modes. In the next section we will briefly discuss the convergence behaviour of the numerical scheme before we continue to describe our results for rotating configurations.

4.3 Convergence Tests

The finite difference operators we are using to approximate the righthand side of the perturbation equations are only accurate up to a certain order. As already mentioned in Section 3.6, the central difference scheme we apply for computing derivatives is equivalent to the use of a local, second order interpolating Lagrange polynomial and evaluating its spatial variation at every gridpoint. The higher the resolution of the computational domain the better the local approximation and therefore the smaller the truncation error. For a quadratic interpolation it is of second order, i.e. doubling the number of gridpoints will result in a four times smaller error. The θ-ICN algorithm with swapped weights is generally only first-order accurate in time which is due to the temporal discretization of all implicit Crank-Nicholson methods (e.g see equation (3.24)). One can however show that for $\theta = 1/2$ the scheme becomes second order in time as well since the leading term proportional in the truncation error is given by (see [68])

$$e_T \sim (1/2 - \theta)\Delta t + \mathcal{O}(\Delta x^2, \Delta t^2) \tag{4.2}$$

Since we decided to use an intrinsically dissipative scheme with unequal weights (keep in mind that for all simulations we use $\theta = 0.6$) as well as explicit Kreiss-Oliger viscosity this order of accuracy certainly does not apply to our situation; we expect to observe first-order convergence in time. This is however nothing we want to study here; of course one can investigate the effects of decreasing the temporal resolution but there are certain limitations. First of all one cannot start with an arbitrary large time step. At least with an explicit time-integrator the CFL-criterion sets a threshold on Δt for a stable evolution. Second, as one decreases the timestep the Nyquist frequency increases and the frequency resolution will decrease. In order to maintain a definitive resolution in the frequency domain one has to increase the number of samples which normally means to evolve the system for a longer period of time. But this can be difficult if the code does not possess longterm stability properties. So speaking of convergence behaviour usually means to investigate the effects of increasing the number of spatial gridpoints. From equation (4.2) this decrease in grid spacing should lead to a second-order effect. There is still a minor complication in the formulation presented here: As described in the previous Section 4.2, when changing in the resolution of the numerical domain one usually also has to adjust the various viscosity coefficients for the Kreiss-Oliger dissipation. Using the same values generally leads to an unstable scheme again; a rule of thumb is that higher resolution requires less artificial viscosity. This behaviour puts some restrictions to the convergence checks. The usual procedure is to take a differential equation (for example the wave equation), run some simulations with increasing resolution, compute the eigenfrequencies and monitor its variation with respect to the number of gridpoints. In our case though, the time evolution equations are not independent of the resolution; the artificial viscosity coefficients depend on them so for each new resolution we are actually studying a slightly different set of equations than in the previous run. It is therefore not as straightforward as described previously with the simple wave equation example to make statements about convergence in this case. But as it turns out we can see a second order accurate behaviour. The following Figure 4.9 depicts this observation for the fundamental quasiradial and quadrupolar oscillation mode.

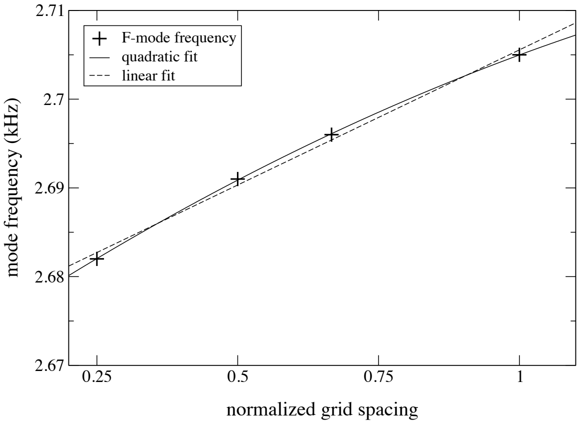

4.9.1: F-mode convergence

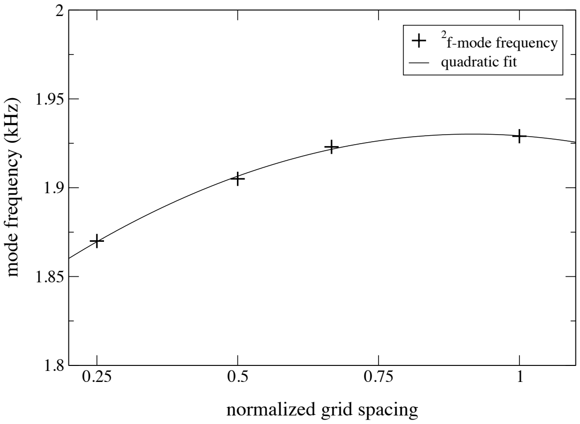

4.9.2: ^2f-mode convergence

Figure 4.9: Convergence behaviour and numerical fits of the fundamental quasiradial and quadrupolar modes

As already mentioned in Section 4.2, we mainly performed simulations for four different resolutions 50×40, 75×60, 100×80 and 200×160. The grid spacing variable in the plots of Figure 4.9 is normalized to the lowest of this resolution; i.e. the frequencies for the

50×40 resolution indicated by a plus-sign are located at a normalized grid spacing of 1.0. Doubling the resolution will lead to a decrease in the distance of the grid points by a factor of two; accordingly the results for the two fundamental mode frequencies in simulations with a 100×80 resolution are highlighted as plus-signs at a normalized grid spacing value of 0.5 and similar considerations apply for the other cases. One can clearly see, especially for the quadrupolar oscillation, that the convergence behaviour is non-linear. For the F-mode, we did both a quadratic fit and a linear one for comparison to the calculated frequencies; the result is depicted in subfigure 4.9.1 where the linear fit is drawn in dashed lines. It is evident from there that the frequencies obtained from the simulations are much better in accordance with a quadratic convergence than with a linear one; this is even more obvious for the ${}^2f$-mode in subfigure 4.9.2 where there is no possibility to fit the data properly with a single straight line. So it seems that neither the actual form of the dissipation operator (see equation (3.28)) nor the resolution dependent viscosity coefficients do show a critical impact on the expected convergence properties of the implemented θ-ICN with unequal and swapped weights; the scheme stays second order in space.

4.4 The Axisymmetric Case

In Section 4.2 we already studied axisymmetric pressure modes for a nonrotating, spherically symmetric BU0 star. Since the perturbation equations are formulated in a comoving frame of reference, their structure remains the same in the rotating case. This is a great advantage over a stationary coordinate system where supplementary terms proportional to the angular velocity Ω enter the righthand sides of the equations; making them both more complicated and prone to any numerical instabilities. In addition we can save some computer time in the axisymmetric case since the complex perturbation equations reduce to a purely real system for $m = 0$; see Section 2.5.1. From the nonrotating and slow-rotation limit it is well known that one can decompose fluid and metric perturbations in terms of spherical, vector and tensor harmonics which split into two distinct classes, depending on their behaviour under space reflection (i.e. $\mathbf{r} \to -\mathbf{r}$). The polar parity perturbations change sign like $(-1)^l$ while the axial parity variables transform like $(-1)^{l+1}$. The pressure modes studied so far belong to the polar class; we will continue to discuss their properties when the compact objects starts rotating faster and faster before we turn to inertial modes which are of axial parity.

4.4.1 Polar Perturbations

For investigating the effects of rotation on polar modes we will use the same trial initial data as in the nonrotating case; see equation (4.1). In the nonrotating case, its denominator is actual independent of the polar angle θ since the star is spherically symmetric. This changes when the angular velocity becomes nonzero. Due to centrifugal forces the compact object gets flattened along the rotation axis; correspondingly the factor $r_s(\theta)$ in equation (4.1) is larger for gridpoints near the equatorial plane; see for example Figure 3.4. This will slightly alter the shape of the trial pressure perturbation from a purely $l = 0$-like dependence.

The following Figure 4.10 shows the results obtained by the numerical scheme presented in this thesis and compares it to values found in the literature [72] for various axisymmetric pressure modes. The dashed lines represent our simulations performed on a 200×160 grid while the solid lines are the reference frequencies. The agreement between them is very good, most notably the first overtone of the quadrupolar fundamental mode, i.e. the ${}^{2}p_1$ oscillation is matched perfectly. We are also nicely consistent with both the $l = 0$ and the $l = 2$ fundamental modes. The difference in the frequencies for the quasiradial overtones is a little bit larger, especially when going to higher rotation rates near the Kepler limit, but they never exceed the 5%-level. And while the reference curves often show some kind of step-like behaviour where the frequencies go up then down and up again our dashed graphs are generally quite smooth throughout the whole range of angular velocities.

There are two cases where we don't agree with the published results at rotation rates near the Kepler frequency; it is the second and third quasiradial overtones. While in [72] they observe a decrease of the mode frequency when approaching the critical angular velocity we cannot confirm this behaviour. The frequencies we compute increase monotonically after approaching a local minimum at around 2.5 kHz. Since we know the radial and polar dependence of the nonrotating eigenfunctions, see Figure 4.5, we can also extract them in the rapidly rotating case and carry out a comparison. Especially for rotation frequencies near the Kepler limit it is sometimes difficult to pick the correct peak of a specific oscillation mode; the power spectral density plots are not always as unambiguous as in the previously presented examples. To identify a certain mode without any doubt one has to take a look at its eigenfunction and this is what we did in Figure 4.11. We took the frequencies of Figure 4.10 for the most rapidly rotating model BU9 in Table 4.1 and computed the shape of the corresponding eigenfunctions.

As one can clearly see, again the eigenfunctions can be related to the quasiradial fundamental mode and its first three overtones. If we compare Figure 4.11 with its counterpart in the nonrotating case, i.e. Figure 4.5, we observe that the non-vanishing regions of the eigenfunctions are pushed towards the rotational axis. Also the radial nodes for the BU0 model are truly radial, i.e. they can be described by an equation of the form $\sigma = const.$ in the coordinate system of the computational domain which practically translates to a $r = const.$-relationship in spherical coordinates. In the rapidly rotating case, the location of the nodal regions is no longer independent of θ. As one moves along a node towards the equatorial plane (i.e. $\tau = 1$) one also approaches the surface of the star.

Table 4.2 summarizes our results for the first four quasiradial and the first two quadrupolar axisymmetric pressure modes; angular velocity and the mode frequencies are given in units of kHz.

In summary we can say that our code is able to reproduce oscillation mode frequencies of axisymmetric polar perturbation both for nonrotating and rapidly rotating compact stars to a very good accuracy. Since the background model used in this thesis uses a polytropic equation of state and the fluid perturbations obey the very same relationship, these pressure modes are the only polar modes we are able to simulate; for gravity- or g-modes one needs buoyancy which is absent in our setup. Let us hence now turn to the description of axial perturbations and the results obtained there.

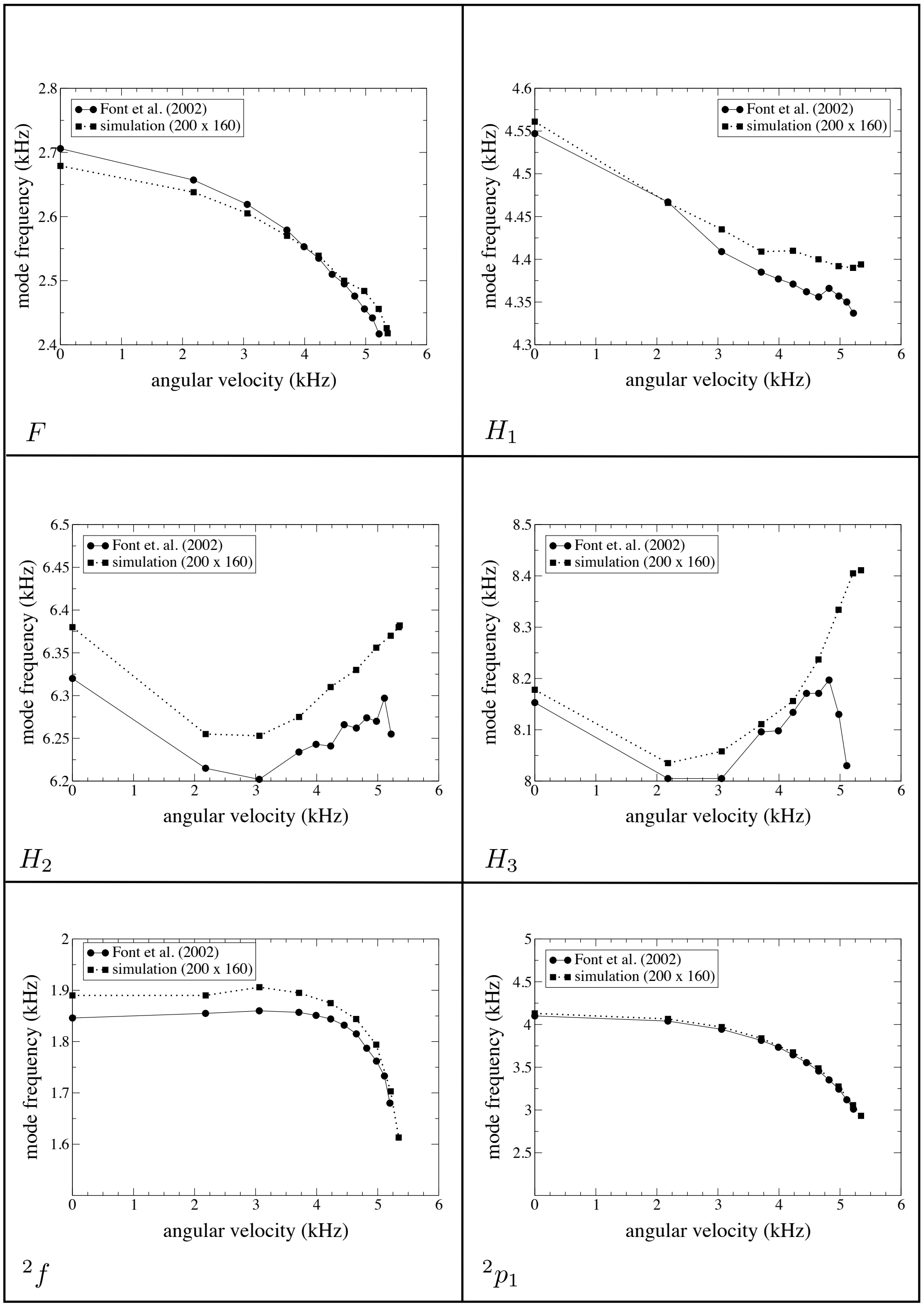

Figure 4.10: Comparison of the simulation results against published values for several oscillation modes

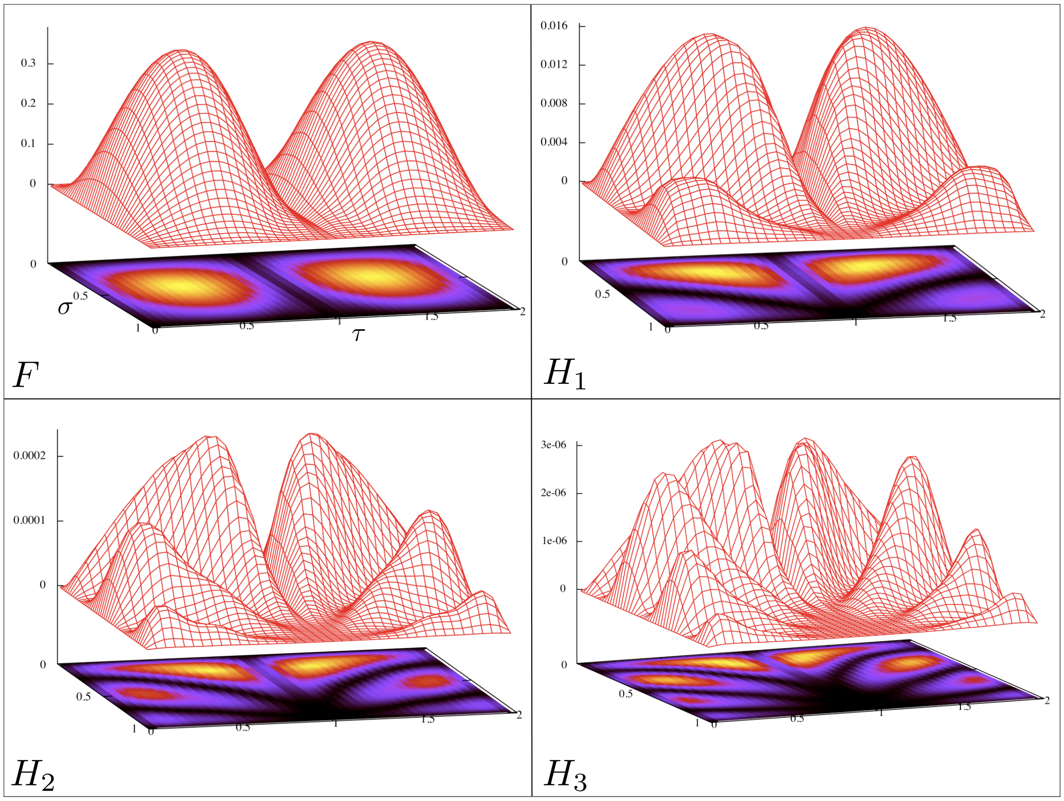

Figure 4.11: Spatial variation of the Fourier amplitude of δu_ζ for the quasiradial mode and its overtones with the BU9 model as background

Ω	F	H_1	H_2	H_3	${}^2f$	${}^2p_1$
0.0	2.679	4.561	6.380	8.178	1.890	4.130
2.182	2.638	4.466	6.255	8.035	1.890	4.065
3.062	2.605	4.435	6.253	8.058	1.906	3.970
3.712	2.570	4.409	6.275	8.111	1.895	3.838
4.229	2.539	4.410	6.310	8.156	1.875	3.674
4.647	2.500	4.400	6.330	8.237	1.844	3.487
4.976	2.484	4.392	6.356	8.334	1.794	3.275
5.214	2.456	4.390	6.370	8.405	1.703	3.056
5.344	2.426	4.394	6.380	8.411	1.613	2.932
5.361	2.418	4.391	6.382	8.435	1.604	2.873

Table 4.2: Frequencies of several polar pressure perturbations for the BU model series; units are kHz

4.4.2 Axial Perturbations

While pressure is the restoring force for p-modes and buoyancy tries to pull back fluid perturbations in g-modes, the Coriolis force takes this part for the so-called inertial modes, i.e. axisymmetric axial perturbations. Therefore they only exist in rotating stars with frequencies that are proportional to the angular velocity. This makes them somewhat difficult to compute accurately since the numerical code needs to be stable for a sufficient long time in order to record as many oscillation cycles as possible. As already mentioned in several sections, the algorithm implemented during this thesis is both implicitly and explicitly dissipative. Due to truncation errors when using a finite difference scheme we introduced an implicit viscous term which in our case is of order $\mathcal{O}(\Delta t)$. In addition, the artificial viscosity needed to get rid of exponentially growing modes is the explicit dissipation term that is present here. Both these effects will remove energy out of the modes and damp them; how strong this will happen depends on the evolution time (longer time-evolution runs mean a larger decrease in the amplitude of the mode) and the value of the Kreiss-Oliger dissipation coefficients (the higher they are the stronger obviously the damping). Eventually the decrease in amplitude will become so large that roundoff-errors destroy the numerical stability at a certain point. Luckily this has not been the case in our simulations; typical time evolutions for axial perturbations were stable at least for 60 ms which usually is enough for an adequate frequency determination. In most cases there was no need to supply special initial data or to perform many mode recycling iterations; the axisymmetric inertial modes were excited as a byproduct of the initial data (4.1). Only for very rapid rotation several recycling runs were necessary to get a cleaner signal. The following Figure 4.12 depicts the typical outcome of such a simulation for a BU3 compact object.

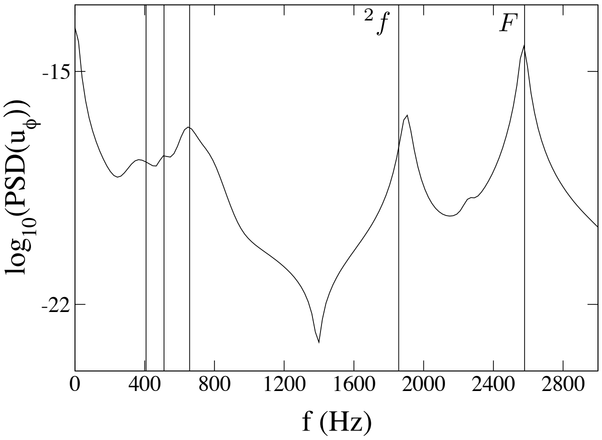

Figure 4.12: Axisymmetric inertial modes for a BU3 model; solid vertical lines denote literature values

Since the very same initial conditions are used as in the axial case, it is no surprise that the two most dominant peaks can be identified with the fundamental quasiradial and quadrupolar mode. Keep in mind that the F-mode frequencies agree very well with published results while we slightly overestimate the ${}^2f$-mode frequency; see Figure 4.10 and Table 4.2 where one can infer an error of 2% for the quadrupolar oscillation in this specific case. More interesting is the low-frequency part of the power spectral density; there three distinct modes are visible. The vertical lines denote published results from [52] where the so-called conformal flatness approximation was used to study non-linear axisymmetric perturbations. This approach also includes perturbations of the metric under the assumption that spacetime can be conformally rescaled to be Euclidian at spatial infinity. Despite the use of the Cowling approximation it is remarkable how well we are able to reproduce the results of [52]; it is obvious that the coupling to the spacetime does not play such a significant role as it is the case for the fundamental pressure mode which were discussed in the last section. However, for the oscillation mode with the lowest frequency in Figure 4.12 and which is labelled i_{-2} in the literature we find stronger deviations than for the intermediate (i_1) and largest (i_2) frequency mode. This is already evident from looking at Figure 4.12; the lowest peak clearly doesn't match the corresponding vertical line which denotes the published value. Especially very low frequencies require long evolution times to determine them accurately; this can explain the observed discrepancy. Similar to Figure 4.10 we show in the following Figure 4.13 a graphical representation of the differences between the results obtained with the linear code and the published values in the conformal flatness approximation for angular velocities up to the Kepler limit.

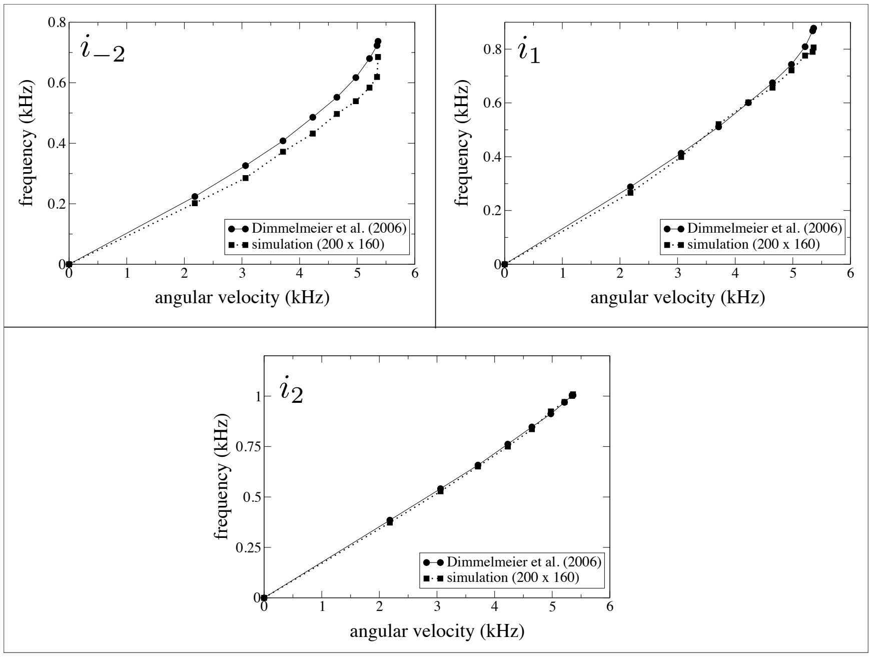

Figure 4.13: A comparison between the literature values and our results for the i_1, i_2 and i_{-2} inertial mode

As already noticed, the relative differences are most strongly pronounced for the lowest frequency oscillation, the i_{-2} inertial mode. However the overall agreement especially for the higher frequency modes is quite remarkable, considering the different approximations and numerical schemes of the codes that are compared here. In the Newtonian limit one can show, e.g. [76], that the inertial mode frequencies for a given angular velocity Ω are confined within the range $0 < \omega < 2\Omega$. Surely this estimation will be altered by general relativistic effects but it tells us roughly that for a BU9 star rotating at its breakup limit of 5.361 kHz we should expect to see no inertial modes beyond a frequency of about 1.7 kHz and indeed the i_1, i_2 and i_{-2} mode are all lying well within this range. The following Table 4.3 shows a tabulated overview of the mode frequencies obtained with the linear code.

Ω	i_{-2}	i_1	i_2
0.0	0.0	0.0	0.0
2.182	0.202	0.266	0.373
3.062	0.285	0.399	0.528
3.712	0.372	0.521	0.651
4.229	0.432	0.602	0.750
4.647	0.497	0.657	0.836
4.976	0.539	0.721	0.924
5.213	0.584	0.776	0.971
5.344	0.619	0.790	1.001
5.361	0.685	0.806	1.009

Table 4.3: Frequencies of the three inertial modes i_1, i_2, i_{-2} for the BU series at different rotation rates

The results presented here show that we are able to successfully excite axisymmetric axial modes which agree very well with eigenfrequencies obtained by more sophisticated codes which do not necessarily rely on the Cowling approximation. This concludes the section about the $m = 0$-type oscillations; in the second part of this chapter we will turn to non-axisymmetric perturbations which in principle, due to the so-called *CFS-mechanism*, are able to drive a neutron star unstable.

4.5 The CFS-Instability

Since the CFS-instability is a generic feature of rotating perfect fluid stars, we will spend some time in sketching the fundamentals on how this instability works. This also includes the notion of counter- and corotating modes and how their frequencies change when transforming from the comoving frame of reference(in which the perturbation equations (2.39)-(2.42) are formulated) to an inertial observer.

Due to the azimuthal decomposition of the time-evolution quantities proportional to $e^{im\varphi}$ and the subsequent Fourier-decomposition which is performed on the numerically obtained time-series, any perturbation variable f is actually split up into

$$f \sim e^{i\sigma t} e^{im\varphi} = e^{i(\sigma t + m\varphi)} \tag{4.3}$$

To track a specific constant phase in time one therefore has to move on by an angle

$$\varphi_0^{\text{comov}} = -\frac{\sigma}{m} t_0$$

after a time t_0. This means that if $\sigma > 0$ and we look at an oscillation mode with $m > 0$, its wave crests will propagate in the opposite direction of rotation and are therefore called retrograde. In contrast, modes with $m < 0$ will move in the direction of rotation and hence are called prograde modes. This holds true in a coordinate system rotating with the star; the question now is how the frequencies change when switching to an inertial frame which is at rest with respect to infinity. The only coordinate that receives a different meaning is the azimuthal angle φ and the relation connecting the two coordinate systems simply is

$$\varphi_{\text{comov}} = \varphi_{\text{in}} - \Omega t \tag{4.4}$$

If one inserts (4.4) into (4.3) the final relationship between mode frequencies in the comoving and inertial frame reads

$$\sigma_{\text{in}} = \sigma_{\text{comov}} - m\Omega \tag{4.5}$$

For axisymmetric perturbations (i.e. $m = 0$) the two frequencies are identical; this is why this discussion was not necessary in the previous Section 4.4. To track a surface of constant phase in the stationary frame a similar calculation like the one above yields

$$\varphi_0^{\text{in}} = -\frac{(\sigma_{\text{comov}} - m\Omega)}{m} t_0$$

This means that if the frequency σ_{comov} is larger than $m\Omega$, then the mode is also travelling in retrograde direction in the stationary system. For $\sigma_{\text{comov}} = m\Omega$ the frequency becomes degenerate in this system while for $\sigma_{\text{comov}} < m\Omega$ a mode travelling retrograde in the comoving frame is seen prograde in the stationary coordinate system. Keep in mind though that this behaviour has nothing to do with general relativistic frame dragging effects; it is a mere consequence of observing the same physical quantities in different coordinate systems. The region in which an oscillation switches from retrograde to prograde in the inertial frame is exactly the instability range of the CFS mechanism.

Originally discovered by Chandrasekhar [20] it was thoroughly investigated by Friedman and Schutz [21], [77] which developed a formal proof for the generic behaviour of this new class of rotational dragging instabilities. They introduced the notion of a canonical energy E_c associated to a perturbation which in the Newtonian case often is described in terms of a displacement vector ξ that connects the position of each fluid element before and after applying the perturbation. Then E_c can be computed in the inertial frame via (see [78])

$$\begin{aligned} E_c \;=\; & \frac{1}{2}\int \Big[\rho|\dot{\boldsymbol{\xi}}|^2 - \rho|v\cdot\nabla\cdot\ \boldsymbol{\xi}|^2 + \Gamma p|\nabla\cdot\boldsymbol{\xi}|^2 + \boldsymbol{\xi}^*\cdot\nabla p\nabla\cdot\boldsymbol{\xi} + \boldsymbol{\xi}\cdot\nabla p\nabla\cdot\boldsymbol{\xi}^* \\ & + \xi^{i*}\xi^j(\nabla_i\nabla_j p + \rho\nabla_i\nabla_j\Phi) - \frac{1}{4\pi}|\nabla\delta\Phi|^2\Big]\, dV \end{aligned} \tag{4.6}$$

Here p, ρ and Γ are as usual pressure, rest-mass density and polytropic exponent and v, Φ and $\delta\Phi$ represent the fluid velocity, the Newtonian gravitational potential and its perturbation respectively. From equation (4.6) it is clear that $E_c = 0$ for an equilibrium configuration. Now the canonical energy can be written as a surface integral of a conserved quantity so any change in E_c from one hypersurface to another one at a later time has to be the energy radiated away by gravitational waves; this also means that E_c is a decreasing function in time. Now if a nonaxisymmetric perturbation is unstable, it will grow unlimited and thereby emit an infinite amount of energy; on the other hand if it is stable it will only radiate away finite energy till it settles back to an equilibrium configuration. This makes the canonical energy a helpful tool in studying instabilities in the following sense:
If $E_c(\xi) \geq 0$ for *all* initial data at some time t then no perturbation radiates infinite energy; the maximum amount of energy available is given by the initial value of E_c at t.
If otherwise $E_c < 0$ for *some* initial data then the configuration is unstable; E_c is a decreasing function of time and therefore can never return to zero, i.e. to equilibrium.
Correspondingly to the canonical energy, a canonical angular momentum J_c can also be defined in the inertial frame. If we consider normal modes of oscillation where $\xi^i \sim e^{i(m\varphi+\sigma t)}$, one can show that

$$\frac{E_c}{J_c} = \omega_p \tag{4.7}$$

where $\omega_p = -\sigma/m$ is the pattern speed of the mode. In contrast to the discussion above we will now restrict m to be strictly positive but allow σ to become negative in return. With this agreement one can obtain an inequality for J_c that reads

$$m^2(\omega_p - \Omega - \frac{\Omega}{m}) \leq \frac{J_c}{C(\xi)} \leq m^2(\omega_p - \Omega + \frac{\Omega}{m}) \tag{4.8}$$

where $C(\xi) > 0$. Now we want to look at a sequence of background models that begin with no rotation and end with the Kepler-limit. As we have already seen, nonaxisymmetric perturbations can be separated into prograde ($\omega_p > 0$) and retrograde ($\omega_p < 0$) modes. For oscillations whose frequencies remain finite as Ω goes to zero, i.e. small rotation, it is clear from equation (4.8) that prograde modes have $J_c > 0$ and for retrograde modes it is similarly $J_c < 0$. By virtue of equation (4.7) the canonical energy is therefore nonzero and positive; the perturbations are stable according to the stability criterion stated above. Consider now a retrograde mode that, for a specific angular velocity of the compact star, enters the region in which $\omega_p \approx 0$. Again from equation (4.8) it follows that $J_c < 0$ then; but the pattern speed ω_p becomes positive in this region and so the canonical energy gets negative which is the indication of a growing instability. As a side note this result also agrees with the weak stability theorem by the same authors in [79] where they proved that instability can only set in for modes whose frequency vanishes along a sequence of equilibrium models. The generic behaviour of this new class of rotational dragging instabilities is evident since all that is needed for them to work is a coupling mechanism to some radiation field (this makes $\dot{E}_c < 0$) and a rotating background that leads to a splitting between pro- and retrograde modes.
The very first polar mode that is likely to become unstable due to this CFS-mechanism is the fundamental pressure mode since it is the lowest order pressure mode. Of course this also depends on the chosen background model; if it doesn't allow high enough angular

velocities so that a counterrotating mode becomes corotating, the instability will not set in. For this reason we will mainly restrict our study of polar perturbations to the $(l = 2, m = 2)$-fundamental mode but we will broaden the range of EoS in our investigation.

4.6 Additional Background Models

Currently the background code adopted in this thesis only allows for polytropic equations of state (see equation (2.17)). The BU series has already been covered properly in Section 4.1, we now will include polytropic fits to tabulated EoS and follow [80] in choosing $\Gamma = 2.46$, $K = 0.00936$ for EoS A and $\Gamma = 2.34$, $K = 0.0195$ to fit EoS II (see also [81, 82] for details). The following Figure 4.14 compares the mass-radius curves for all EoS which are considered in this section in the nonrotating limit; the dots mark the actual background models used for time-evolution.

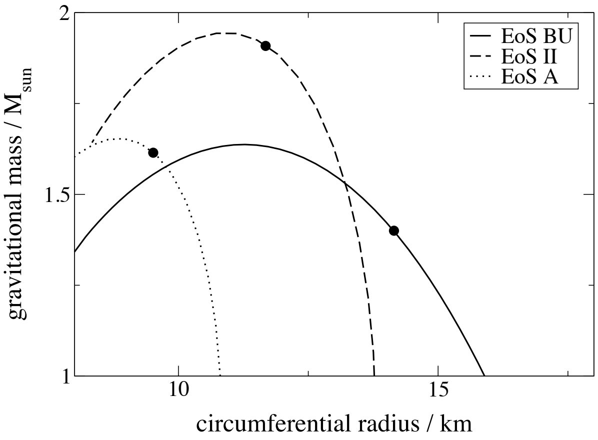

Figure 4.14: Mass-Radius diagrams for different equations of state and nonrotating configurations

The graph for the BU model is actually identical to the corresponding curve in Figure 4.1. As one can see, the trajectories cover a quite wide range in radii and masses; the equilibrium configurations for EoS A and EoS II were chosen to be very close to their maximum allowed masses. The next two Tables 4.4 and 4.5 summarize the basic stellar parameters along the sequence of background models.

As before M is the gravitational mass and R_e the equatorial circumferential radius. Actually we also constructed various stellar models in a rotation frequency range of several hundred Hz. When the nonaxisymmetric oscillations are splitting up and two branches develop for the counter- and corotating modes it sometimes gets difficult to correctly identify them. This ambiguity is avoided if we start observing the splitting right from the beginning at very low rotation rates.

model	Ω (kHz)	r_p/r_e	M ($M_\odot$)	R_e (km)
A0	0.0	1.0	1.62	9.53
A1	4.34	0.95	1.65	9.72
A2	6.11	0.9	1.68	9.93
A3	7.43	0.85	1.72	10.18
A4	8.49	0.8	1.77	10.45
A5	9.36	0.75	1.81	10.77
A6	10.07	0.7	1.86	11.15
A7	10.6	0.65	1.91	11.61
A8	10.94	0.6	1.95	12.17
A9	11.04	0.56	1.96	12.78

Table 4.4: EoS A model parameters

model	Ω (kHz)	r_p/r_e	M ($M_\odot$)	R_e (km)
II0	0.0	1.0	1.91	11.71
II1	3.47	0.95	1.95	11.95
II2	4.88	0.9	1.99	12.22
II3	5.93	0.85	2.03	12.53
II4	6.77	0.8	2.08	12.88
II5	7.46	0.75	2.14	13.28
II6	8.01	0.7	2.19	13.77
II7	8.42	0.65	2.24	14.35
II8	8.67	0.6	2.29	15.08
II9	8.73	0.56	2.3	15.75

Table 4.5: EoS II model parameters

4.7 First Non-Axisymmetric Test Runs

To study nonaxisymmetric oscillations we will not put in a initial energy-density/pressure perturbation as we did for the $m = 0$-case. Instead, again in accordance to [72], a velocity perturbation is used to excite mainly quadrupolar modes. In a spherical coordinate system a small non-zero θ-component is added to the 4-velocity

$$v^\theta = A \sin\left(\frac{\pi r}{r_s(\theta)}\right) \sin\theta \cos\theta \tag{4.9}$$

where A and r_s have the same meaning as in equation (4.1). Since the code presented in this thesis works in cylindrical coordinates a proper coordinate transformation has to be applied; this will introduce additional terms of the form $\sin\theta$ and $\cos\theta$. Additionally, the perturbation equations (2.39)-(2.42) are written with covariant vector components so yet another transformation is needed to alter the contravariant components of equation (4.9). Last but not least we have to take care about the fact that instead of the original hydrodynamical quantities like perturbed energy-density or perturbed velocity, we are using slightly modified evolution variables that turned out to be more useful in the derivation of system (2.39)-(2.42) (see equations (2.35)-(2.38)). After all this has been done very carefully the actual numerical time integration can be performed. Analogue to Figures 4.3 and 4.4 the following Figure 4.15 shows the evolution of the perturbed pressure perturbation after an initial condition of type (4.9) has been applied to a nonrotating BU object.

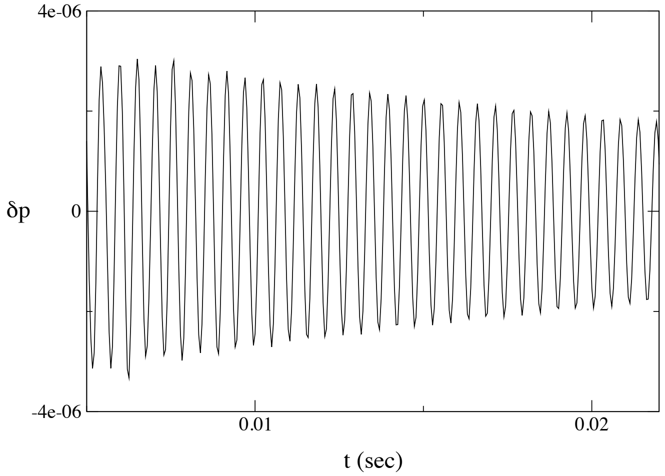

4.15.1: nonaxisymmetric pressure perturbation variation for a BU0 star

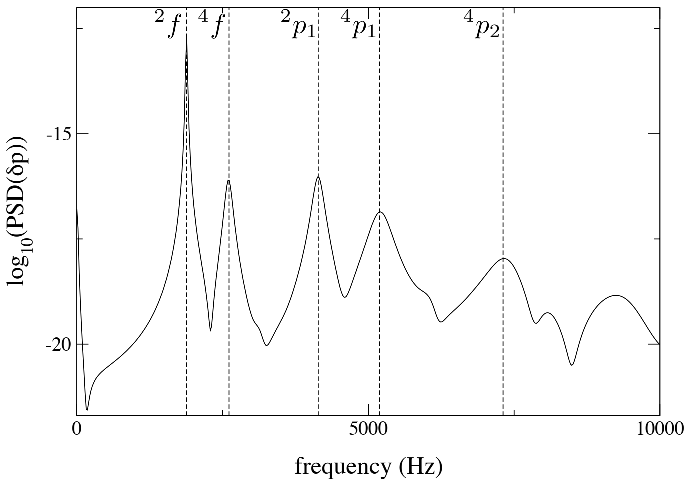

4.15.2: power spectral density of the δp time-series

Figure 4.15: Time series and corresponding PSD plot for an initial velocity perturbation on a BU0 star according to (4.9)

Again only the first 20 msec are depicted even though the actual numerical evolution was stable for at least 60 milliseconds. One can immediately spot two differences if one compares the axisymmetric with the nonaxisymmetric simulations. First of all the dominant mode in Figure 4.15 clearly has a lower frequency than the corresponding $m = 0$ fundamental mode and second, the oscillation is damped stronger. This is a generic behaviour at least in our code since the amount of artificial viscosity needed to get a long term stable evolution is larger for nonaxisymmetric perturbations than for axisymmetric ones. As before the identification of the various frequency peaks in the PSD plot has to be based on the shape of the eigenfunction; this will also be a test whether the mode recycling routine we implemented also works in the nonaxisymmetric case where real and imaginary parts of the perturbation equations explicitly mix. The result of such an extraction for the pressure perturbations is depicted in Figure 4.16; we again chose to monitor a scalar quantity since it is easier to relate its angular behaviour to certain spherical harmonics.
The most strongest peak at $f = 1.879$ kHz can be identified with the fundamental ($l = 2, m = 2$) oscillation mode; the θ-dependence of the corresponding spherical harmonic is given by $Y_2^2 \sim \sin^2\theta$ and keep in mind that the τ-coordinate of the computational domain varies from 0 to 2 and can be thought of being similar to the polar angle in spherical coordinates. The frequency peak at $f = 4.15$ kHz shows a similar angular dependence but additionally a radial node appears near the surface of the star. This leads to the conclusion that this mode labelled as ${}^2p_1$ is simply the first harmonic overtone of the fundamental F-mode. The other eigenfunctions exhibit a different behaviour with respect to θ. Although they all vanish at the boundaries of the computational domain (this is in accordance to the boundary conditions for scalar variables and $m \neq 0$, see Table 2.1), their angular dependence fits perfectly with a ($l = 4, m = 2$)-oscillation since $Y_4^2 \sim \sin^2\theta(7\cos^2\theta - 1)$. The ${}^4f$-mode at $f = 2.61$ kHz apparently has no nodes in radial direction so this is the fundamental mode for ($l = 4, m = 2$). The subsequent peaks at $f = 5.19$ kHz and $f = 7.31$ kHz are its first and second order harmonics which can easily be confirmed by the number of radial nodes that show up in the corresponding eigenfunctions. Similar to the axisymmetric case these additional features were originally not visible at the scale of Figure 4.16; they had to be artificially enhanced to be noticeable. This shows that the eigenmode extraction technique works equally well for nonaxisymmetric simulations and thus is a helpful tool for identifying and examining eigenfunctions.

4.8 Distinguishing Counter- And Corotating Modes

As it has already been pointed out in Section 2.5.2 and proved rigorously in appendix A.2, the only difference in performing a simulation for an $m_0 > 0$ and then running the same simulation with $-m_0 < 0$ is that the imaginary parts of the perturbation quantities will flip in sign. Furthermore it has been shown that this sign flip has no effect on the real part of the complex solution which is taken as the final solution for the purely real initial value problem we want to solve numerically. First of all, this is not only a feature of this specific code; see for example [83] where the Newtonian version of the very same problem has been studied. They also found counter- and corotating modes for $l = 2$ and $m = 2$ with counterrotating modes having higher frequencies in the comoving frame. Still the question is how these different oscillations can be separated in the PSD plot. For this we will make

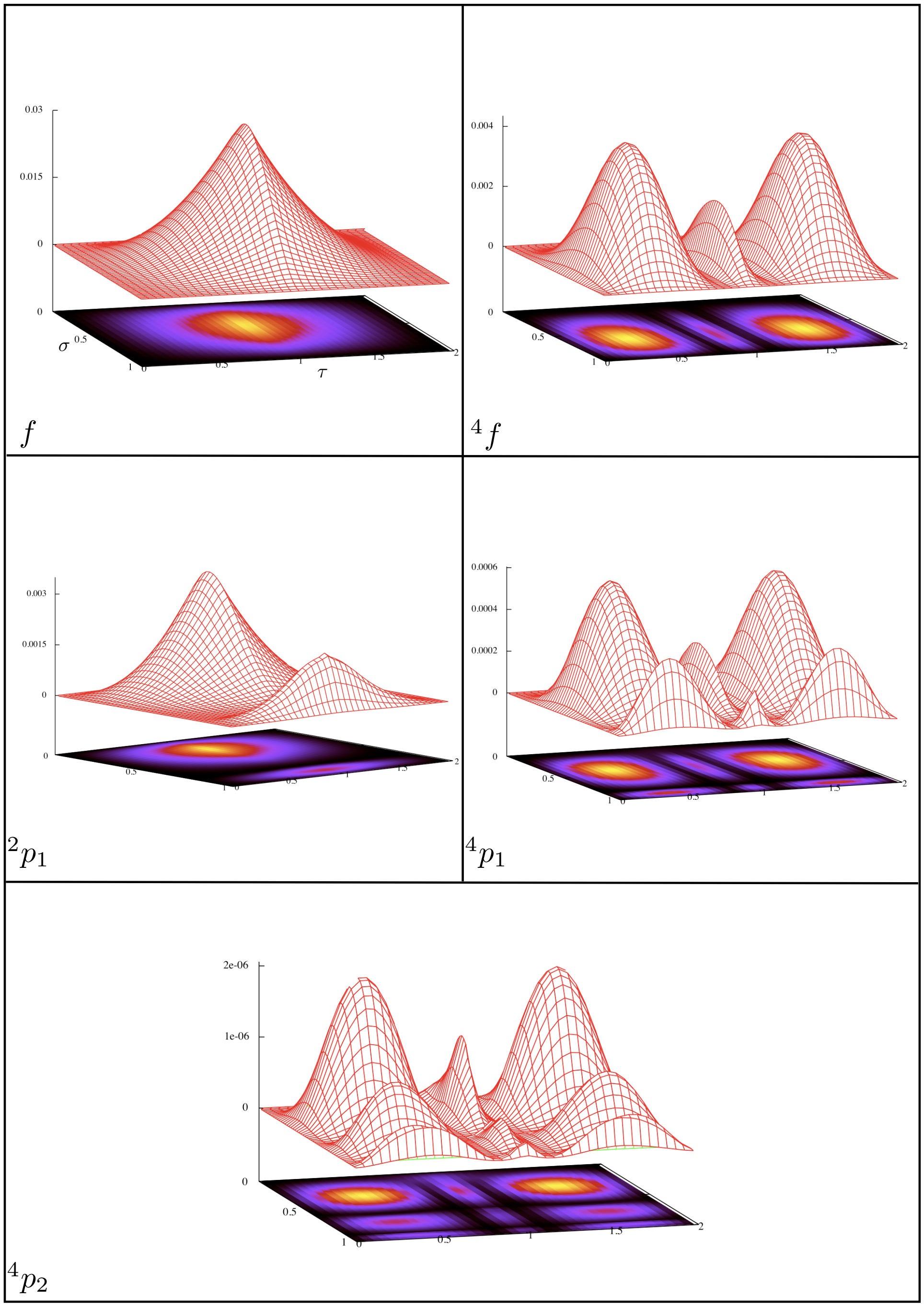

f

^4f

$^2p_1$

$^4p_1$

$^4p_2$

Figure 4.16: Shape of the extracted pressure eigenfunctions for the five labelled peaks in Figure 4.15

use of equations (4.4) and (4.5) which correlate coordinates and measured frequencies in two coordinate systems. It is straightforward to transform any numerically obtained time-series from the comoving frame of reference which is used throughout this thesis to an inertial observer by virtue of equation (4.4). As usual this new time-series can then be Fourier-transformed into frequency space and according to equation (4.5) the mode frequencies in these two frames are related by

$$f_{in} = f_{corot} - \frac{m}{2\pi}\Omega \tag{4.10}$$

It means that an inertial observer will see a frequency decrease for retrograde propagating modes (i.e. $m > 0$ in our notation; see Section 4.5) and an increase for prograde modes by a certain amount that is determined by the azimuthal mode number m and the angular velocity Ω of the star. This is the additional information we can use to distinguish between them in the PSD diagrams.

But let us first verify the statement about the sign flip in the imaginary parts of the complex perturbation variables when changing the sign of m. Figure 4.17 shows real and imaginary parts of δu_ρ for a BU0 star and after evolving trial initial data for roughly 10 msec; solid lines denote the $m = 2$-solution while dashed lines depict the result of a $m = -2$ simulation.

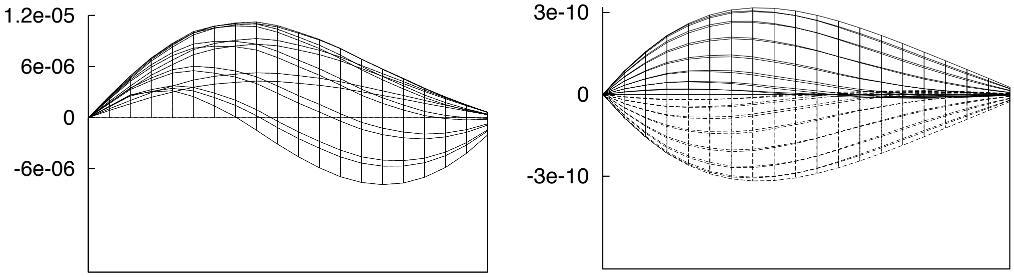

Figure 4.17: *Left panel:* Real part of δu_ρ for both $m = 2$ (solid) and $m = -2$ (dashed) *Right panel:* Imaginary part of δu_ρ for both $m = 2$ (solid) and $m = -2$ (dashed)

Both functions are viewed from a point within the σ-τ–plane. The two solutions for the real part of δu_ρ overlap perfectly; in accordance with the prediction there is no difference. The imaginary part on the other hand shows the predicted change in sign when comparing the various solutions; apparently the numerics is also able to reproduce this analytical property derived in Section 2.5.2.

Next we turn to the actual determination of counter- and corotating modes. For this purpose the following Figure 4.18 shows the splitting of the fundamental mode for a BU star rotating at $\Omega = 694$ Hz. This object has a ratio of polar to equatorial circumferential radius of $r_p/r_e = 0.995$ so it still can be considered as approximately spherical symmetric. Nevertheless one can notice the formation of two different frequency branches whereas in the nonrotating limit there was only one (compare Figure 4.18 with Figure 4.15). Rotation breaks the degeneracy between prograde and retrograde propagating modes and the fundamental oscillation at $f = 1.879$ kHz for the BU0 model gets split up into two parts at $f_1 = 1.784$ kHz and

$f_2 = 1.948$ kHz in the comoving frame. Plotted with dashed lines in Figure 4.18 is the corresponding PSD distribution for an inertial observer; let us focus on the f_1-frequency peak.

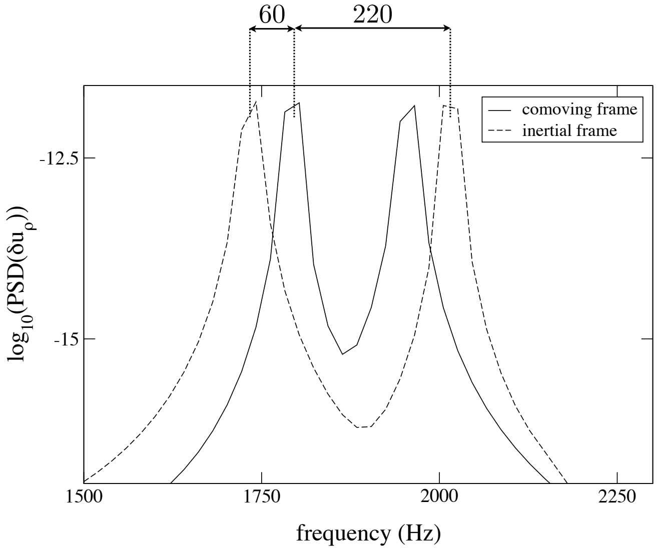

Figure 4.18: Splitting of the fundamental mode in two different frames of reference

The question is now which one of the two maxima in the inertial frame can be related to this specific peak. According to equation (4.10) the frequencies in the different coordinate systems a biased by a factor of $m\Omega/2\pi$ which in this example with $m = 2$ and $\Omega = 694$ Hz turns out to be roughly 220 Hz. Also in Figure 4.18 we indicated the relative distance in frequency space from the f_1-mode to its potential counterparts in the inertial frame; it is quite obvious from the plot which peak we have to choose. The one located at f_1 belongs to the corotating fundamental mode and its frequency increases when observed from an inertial frame of reference while the peak we find at f_2 can be identified with the counterrotating F-mode whose frequency decreases when measured in a coordinate system at rest; in perfect agreement with [83].

After we are able to distinguish between prograde and retrograde propagating modes, we can now turn to the investigation on how the rotation of the compact object affects the nonaxisymmetric perturbations.

4.9 The Non-Axisymmetric Case

The discussion about nonaxisymmetric oscillations will also be divided into two parts concerning axial and polar perturbations. The axial part mainly deals with the fundamental mode; because it has the lowest frequency of all pressure driven modes and therefore is most likely prone to the CFS-instability. Since a compact object can only be spun up to the Kepler-limit, higher order harmonics may actually never reach the regime where their frequencies drop to zero. On the other hand, the growth time of unstable modes with $l = 3, 4, \ldots$ is just too long to become significant; in realistic neutron star models it is very likely that viscosity effects damp the swelling instability away. However we want to stress that the code presented here is in fact able also to follow the evolution of high order nonaxisymmetric perturbations. When starting with (4.9) as trial initial data not many of them are excited though; clearly several mode recycling runs are necessary in these cases. Just for demonstration purposes the following Figure 4.19 depicts the change in frequency of the ${}^2f$-, ${}^4f$- and ${}^2p_1$-mode for several rotation rates of a BU star. As already mentioned the fundamental mode is the strongest one with the most clear peak in the power spectral density and it therefore can be traced continuously throughout the whole range of rotation frequencies. Without any explicit mode recycling runs the other perturbations are somewhat more difficult to track, for the ${}^4f$-mode we had to stop at around 4 kHz since its identification was no longer possible, still it shows that in principle there are no restrictions from a numerical point of view to study higher order modes.

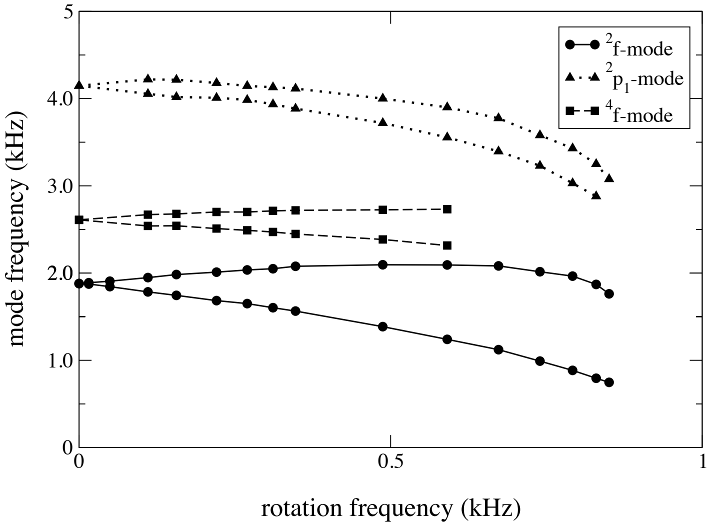

Figure 4.19: Dependence of various nonaxisymmetric modes on the angular velocity of a BU star

Nevertheless we will restrict ourselves from now on to focus on the fundamental mode entirely. Keep in mind however that the Cowling approximation affects the ${}^2f$-mode most rigorously as it already has been pointed out in Section 2.3. For higher harmonics the neglect of metric perturbations is practically of no consequence for the mode frequencies but the accuracy of the Cowling approximation decreases rapidly with decreasing radial node number; the difference can be as high as 100% (see for example [52] and [50]). So we won't get the absolute values right but rather receive an impression about the qualitative behaviour of the nonaxisymmetric quadrupolar fundamental mode once rotation sets in and is increased towards the Kepler limit.

4.9.1 Polar Perturbations

It is well known that the f-mode frequency for nonrotating Newtonian stars only depends on the mean density and the polar order l of the perturbation; the exact formula in the case of uniform density is given by

$$\omega^2 = \frac{2l(l-1)}{2l+1}\frac{M}{R^3} \tag{4.11}$$

and is approximately valid also in the relativistic case; see [18]. Based on the stellar parameters of the various background models in Table 4.1, 4.4 and 4.5 we expect to observe the highest f-mode value for EoS A, followed by EoS II and EoS BU. The following Figure 4.20 shows the results of simulations for the three equations of state.

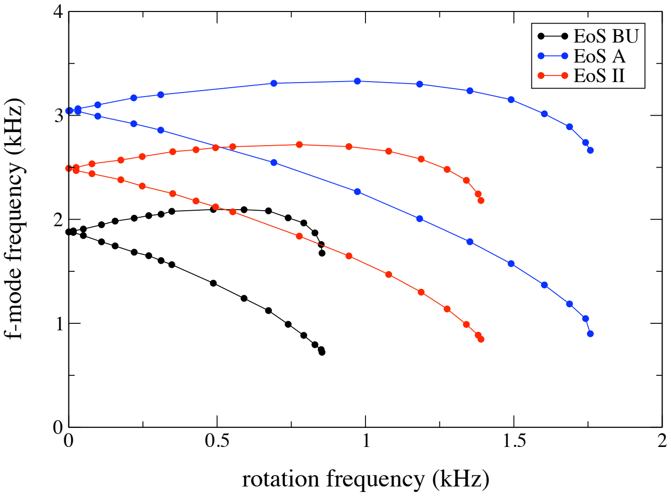

Figure 4.20: Splitting of the fundamental mode for three different EoS in the comoving frame of reference

Every curve concludes at its value for the Kepler-limit; an important difference to the corresponding diagrams in the axisymmetric case (e.g. Figure 4.10) is that instead of angular velocity Ω we now plot the mode frequencies against rotation frequency, that is $\nu_{rot} = \Omega/2\pi$. Keep in mind that Figure 4.20 depicts the frequency variation in a frame of reference corotating with the star. According to the discussion we had in Section 4.8, for each EoS the counterrotating modes are represented by the branches with higher mode frequencies. As we have seen, they get shifted towards lower frequencies when observed in an inertial frame and therefore can become CFS-unstable. From Figure 4.20 it is evident that in the nonrotating limit indeed it is $f^{{}^2f}_{\text{EoS A}} > f^{{}^2f}_{\text{EoS II}} > f^{{}^2f}_{\text{EoS BU}}$; more specifically we find

$$f^{{}^2f}_{\text{EoS A}} = 3.043\,\text{kHz} \qquad f^{{}^2f}_{\text{EoS II}} = 2.491\,\text{kHz} \qquad f^{{}^2f}_{\text{EoS BU}} = 1.879\,\text{kHz}$$

One may even test how good the ratio of the f-mode frequencies is approximated by the corresponding ratio of mean densities according to equation (4.11); masses and radii of the nonrotating background models can be again inferred from the Tables 4.1, 4.4, 4.5.

EoS ratio	frequency ratio	mean density ratio
A/BU	1.62	1.95
A/II	1.22	1.25
II/BU	1.33	1.55

Table 4.6: Comparison between mode frequency- and corresponding mean density-ratios

Table 4.6 actually shows reasonably good agreements especially for the combination of EoS A and EoS II. The obvious discrepancies can be explained by the fact that equation (4.11) is strictly valid only in the case of Newtonian uniform density stars; for relativistic perfect fluids this relation is more a rough rule of thumb anyway. The next Table 4.7 gives a detailed summary about the change of the fundamental mode frequency with rotation.

	EoS BU		EoS II		EoS A	
r_p/r_e	$m = 2$	$m = -2$	$m = 2$	$m = -2$	$m = 2$	$m = -2$
1	1.879	1.879	2.491	2.491	3.043	3.043
0.95	2.078	1.564	2.699	2.073	3.309	2.547
0.9	2.095	1.386	2.719	1.839	3.33	2.267
0.85	2.093	1.24	2.7	1.648	3.301	2.007
0.8	2.082	1.122	2.656	1.47	3.237	1.785
0.75	2.015	0.991	2.58	1.3	3.152	1.574
0.7	1.965	0.884	2.481	1.138	3.015	1.369
0.65	1.87	0.794	2.375	0.989	2.89	1.186
0.6	1.758	0.747	2.244	0.886	2.74	1.045
r_K	1.675	0.722	2.182	0.847	2.664	0.9

Table 4.7: ${}^2f$-mode frequencies (in kHz) for all three EoS; r_K denotes the axis ratio at Kepler-limit

In this table the angular velocity is given in terms of the axis ratio r_p/r_e of the compact star; the value of r_K denotes this ratio for the Kepler-limit which is 0.58 for EoS BU and 0.56 for EoS A and EoS II. The following Figure 4.21 is just another way to look at these results.

There we plot the ${}^2f$-mode frequency normalized by its nonrotating value against the rotation frequency scaled by its corresponding Kepler-limit for the three equations of state. This

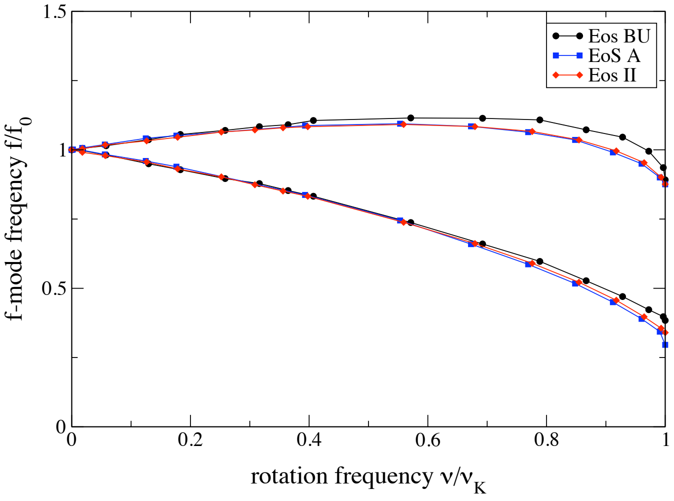

Figure 4.21: Normalized version of Figure 4.20

means that all curves start at the point $(0, 1)$ and will stop at a normalized rotation frequency of 1. It is evident from Figure 4.21 that the three curves are nearly indistinguishable up to a ration of roughly 0.4 and even beyond this value the agreement in the normalized frequencies is striking. If we write for all rotation parameters

$$\frac{f}{f_0} = 1.0 + C_{lm}^{(1)} \left(\frac{\nu}{\nu_K}\right) + C_{lm}^{(2)} \left(\frac{\nu}{\nu_K}\right)^2 \tag{4.12}$$

and make a least-square fit through all the data points one arrives at $C_{22}^{(1)} = -0.25 \pm 0.02$, $C_{22}^{(2)} = -0.25 \pm 0.02$ for $m = 2$ and $C_{2-2}^{(1)} = 0.48 \pm 0.03$, $C_{22}^{(2)} = -0.55 \pm 0.04$ in the $m = -2$ case. To get an impression of how well this 2nd-order approximation fits the data the following Figure 4.22 shows again the three graphs but now together with the fitting polynomial.

Keep in mind though that everything presented up to now is in the comoving frame of reference; the picture changes substantially if one transforms the frequencies from Table 4.7 to an inertial observer. According to equation (4.10) this means to add an extra term $-m\nu$ where ν is the rotation frequency and the following Figure 4.23 shows the result of such a transformation. As already discussed in Section 4.8 the counterrotating $m = 2$ modes now get shifted towards lower frequencies while the corotating $m = -2$ solutions attain higher frequencies; the pro- and retrograde branches are therefore reversed compared to the comoving frame. One can clearly see that all three model series actually reach the point where the ${}^2f$-mode has zero frequency and hence becomes unstable to the CFS-instability; see Section 4.5. For the less compact background models , i.e. the BU equation of state, this happens quite close to its Kepler-limit; the other more compact series reach that particular

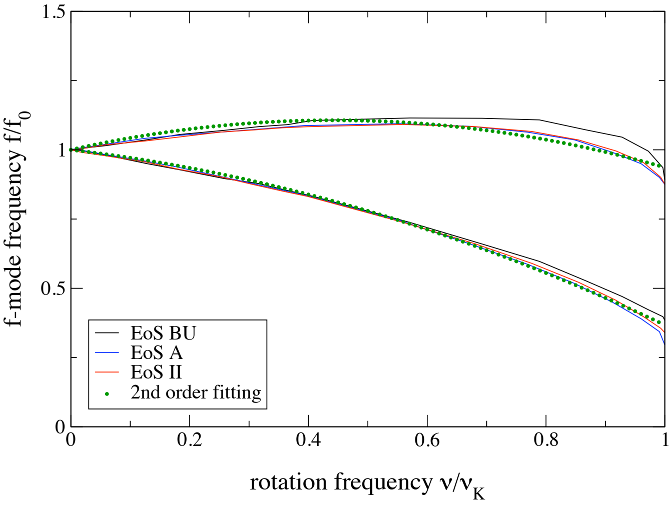

Figure 4.22: The fitting through all data points of Figure 4.21

point considerably earlier. Also pointed out in Section 4.5 and now evident from the figures is that the unstable $m = 2$ mode is seen retrograde in the comoving system but prograde in the inertial frame. One immediately notices that the normalized picture in the inertial frame does not show the nice independence of the mode frequency from the equation of state. The three branches already deviate from each other at low rotation rate where the largest discrepancy can be observed with the BU series.

There is no chance to fit the data points equally well as in the comoving frame. How can we understand this? It is well known from Newtonian theory (see [76] for example) that the frequency shift induced by rotation in the inertial frame can be related to the eigenfunction of the mode via

$$f(\Omega) = f(0) - m\nu(1 - C_{nl}) + \mathcal{O}(\nu^2) \quad \text{with} \quad C_{nl} = \frac{\int_0^R \rho r^2 (2\xi_r \xi_h + \xi_h^2) dr}{\int_0^R \rho r^2 (\xi_r^2 + l(l+1)\xi_h^2) dr} \tag{4.13}$$

Here, ξ_r and ξ_h represent the radial and angular parts of the eigenfunction. On the other hand, equation (4.10) tells us that in order to switch to the comoving frame a factor of $m\nu$ has to be added to relation (4.13). If one now rewrites (4.13) in terms of the scaled variables in Figures 4.21 and 4.23 one arrives at

$$\frac{f}{f_0}|_{in} = 1.0 - m\left(\frac{\nu_K}{f_0}\right)\left(\frac{\nu}{\nu_K}\right) - mC_{nl}\left(\frac{\nu_K}{f_0}\right)\left(\frac{\nu}{\nu_K}\right) + \mathcal{O}((\nu/\nu_K)^2) \tag{4.14}$$

in the inertial frame and

$$\frac{f}{f_0}|_{corot} = 1.0 - mC_{nl}\left(\frac{\nu_K}{f_0}\right)\left(\frac{\nu}{\nu_K}\right) + \mathcal{O}((\nu/\nu_K)^2) \tag{4.15}$$

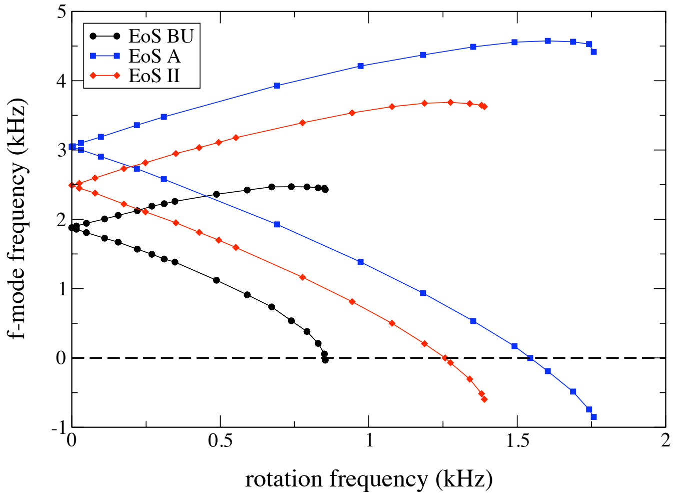

4.23.1: Splitting of the ^2f-mode in the inertial frame

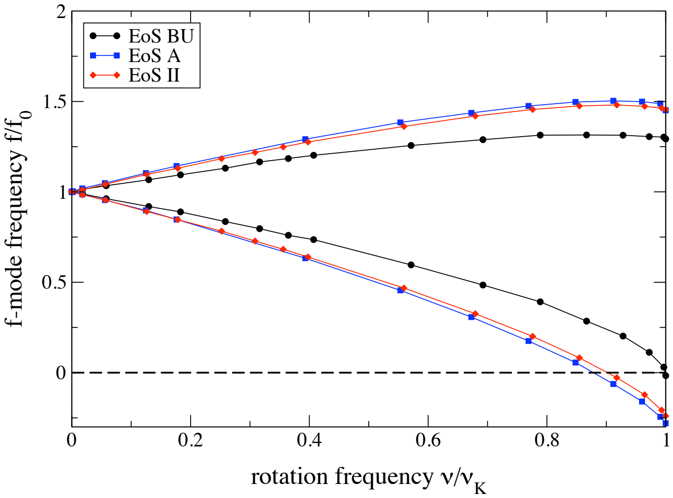

4.23.2: Normalized version of the above picture

Figure 4.23: Same as Figures 4.21 and 4.22 but in the inertial frame

in the corotating system. Now the ratio of ν_K/f_0 is similar for all three equations of state but it is not exactly identical; for EoS BU the value is 0.454 and for EoS A and EoS II it is 0.577 and 0.558 respectively (one can easily compute these values from the Tables 4.1, 4.4, 4.5, 4.7). As we have seen empirically in the comoving system, the slopes of all three branches is nearly identical. This means that the factor C_{nl} in equation (4.15) counterbalances the differences in ν_K/f_0 so that the product of these two terms stays nearly constant. The same product also appears in the inertial frame but this time there is also a term $\sim \nu_K/f_0$ which does not get neutralized in the same way as in the corotating system; see equation (4.14). This explains the apparent differences in the Figures 4.21 and 4.23.
To summarize, we have shown that the code developed during this thesis is also able to evolve nonaxisymmetric polar perturbations up to the Kepler-limit. The computed ${}^2f$-mode frequencies show the expected behaviour on the compactness of the background models and a useful relationship between mode frequency and rotation rate has been found in the corotating frame of reference which is nearly independent of the equation of state investigated so far. Additionally, the neutral points for all three EoS have been identified; beyond this point the ${}^2f$-mode is unstable due to the CFS-criterion. As we have done in the axisymmetric case we will now turn to axial perturbations.

4.9.2 Axial Perturbations

Non-axisymmetric axial perturbations, which are also called r-modes due to the similarity with planetary- or Rossby-waves on Earth, are known to be generically unstable according to the CFS-criterion. From Newtonian theory one can deduce that the frequency of an r-mode in the comoving frame is given by (see [76])

$$f_{corot} = \frac{2m\nu}{l(l+1)} \tag{4.16}$$

where ν is the angular frequency of the star. Keep in mind that whenever the frequency changes sign when transforming from the comoving frame to the inertial system or vice versa the CFS-instability will work. Switching to the inertial frame of reference transforms equation (4.16) into

$$f_{in} = \frac{2m\nu}{l(l+1)} - m\nu \leq 0 \quad \text{for} \quad m > 0 \tag{4.17}$$

independent of the rotation rate. So if the r-modes will be excited, even slowly rotating stars will become unstable and, depending on the maximum amplitude and other damping mechanisms, will emit a certain amount of rotational energy in gravitational waves. This particular class of oscillations therefore may have many possible applications in astrophysics and gravitational wave research, e.g. [27, 84].
We also did a couple of simulations to specifically excite the $(l = 2, m = 2)$ inertial mode for rapidly rotating models and were successful. Inertial modes of fast rotating stars exhibit a strong coupling between axial and polar contributions of various order which makes a unique identification of the corresponding eigenfunction rather tedious. Using spherical coordinates it can be shown (see [85], [37]) that for example the perturbation of the θ-component of the

4-velocity is given by

$$\delta u_\theta \approx \sum_{k=0}^{n} \frac{1}{r} \left(V_{m+2k+1} \frac{\partial P^m_{m+2k+1}}{\partial \theta} + \frac{m}{\sin(\theta)} U_{m+2k} P^m_{m+2k} \right) \tag{4.18}$$

where the summation limit n fixes the number of coupling terms, U and V are power series of $x = r/R$ for the axial and polar contributions and P denote the associated Legendre polynomials of the standard spherical harmonics; similar expressions hold true for the other perturbation quantities.

The case is a little bit different for the fundamental r-mode though. In a Newtonian description this mode has just a single axial contribution and therefore does not mix with higher axial and polar parts. General relativity introduces coupling terms but at least for slow rotation it has been shown in [86], that the amplitude of the dominant coupling term is still an order of magnitude smaller than the original axial part. So according to equation (4.18) we expect the δu_θ dependence to behave like

$$\delta u_\theta \sim \frac{1}{r} \frac{P_2^2}{\sin\theta} = \frac{1}{r} \sin\theta$$

and this is how the initial data has been set up for the axial perturbations. Typically, several mode recycling runs are needed to get a sharp and clean signal in the power spectral density. Also, due to the low frequencies of inertial modes especially at small rotation rates one needs much longer evolution times than for pressure driven modes. We chose to cancel the time-evolution after roughly 50 ms to extract the eigenfrequencies. The numerical code is still stable there and can in principle evolve the initial data for a longer time interval, leading to a more accurate frequency determination. However, we found that an evolution time of about 50 ms and a spatial resolution of 200×160 gridpoints is already quite good for a first estimation; there is only a marginally change when using longer integration intervals. We compare our code with results for a BU6 star rotating at 93% of its maximum speed as described in [87] where a nonlinear general-relativistic code has been used to study the saturation amplitude of r-modes. The following Figure 4.24 gives a summary of the results. By means of repeated mode recycling, the fundamental r-mode can be significantly enhanced as depicted in the PSD plot of Figure 4.24. We also checked the angular dependence of the extracted eigenfunction. Since δu_θ should be $\sim \sin(\theta)$ the ρ- and ζ-components of the perturbed 4-velocity are modified by an additional factor of $\cos(\theta)$ and $\sin(\theta)$ respectively. Keep in mind that the grid variable τ which takes values from 1 to 2 can be thought of similar to the polar angle θ in spherical coordinates; see the discussion of Figures 3.3, 3.4 in this thesis.

Then it is clear that the eigenfunction for δu_ρ and δu_ζ depicted in the bottom row of Figure 4.24 show indeed the expected behaviour. The fundamental r-mode has a frequency of $f_c = 518$ Hz in the comoving frame which translates to a frequency of $f_i = 1.066$ kHz in the inertial frame. This is in excellent agreement with [87] where they found it at $f_i = 1.03$ kHz and also with [88] where they saw the mode at $f_i = 1.05$ kHz; nonlinear effects in the simulations of [87] may explain the larger discrepancy there.

There has also been a debate about the existence of a continuous spectrum for inertial mode frequencies. Most of the analytic results for r-modes have been derived in Newtonian theory, e.g. equations (4.16), (4.17). The question now is, how these results change when including

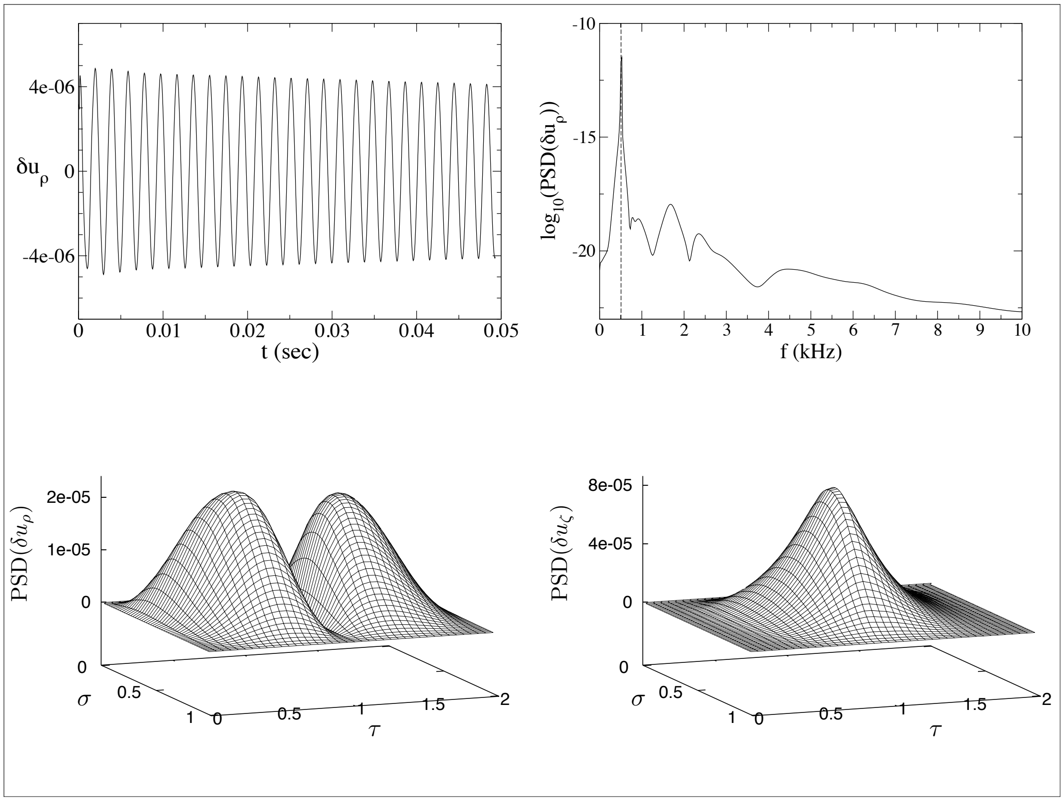

Figure 4.24: *Top Left:* Time evolution of δu_ρ *Top Right:* Corresponding power spectral density plot *Bottom Left:* Shape of the δu_ρ eigenfunction *Bottom Right:* Shape of the δu_ζ eigenfunction

general relativistic effects. With the line-element of a rotating compact object in the inertial frame

$$ds^2 = -e^{2\nu}dt^2 + e^{2\lambda}dr^2 + r^2(d\theta^2 + \sin^2\theta d\phi^2) - 2\omega\sin^2\theta dt d\phi \tag{4.19}$$

a similar calculation both in the Cowling-approximation and the slow-rotation limit leads to

$$f(r) = -m\nu\left[1 - \frac{2}{l(l+1)}\left(1 - \frac{\omega(r)}{2\pi\nu}\right)\right] \tag{4.20}$$

where $\omega(r)$ correlates to the dragging of inertial frames near a rotating relativistic object. Note that equation (4.20) reduces to (4.17) in the case of zero angular momentum of the star but as soon as rotation sets in, equation (4.20) tells us that each fluid layer oscillates with a slightly different frequency. Instead of a single peak in the power spectral density, one therefore has a band of continuous frequencies whose limits are determined by the values of the frame-dragging potential ω at the center and the surface of the star. Initially Kojima [89, 90] investigated the singular structure of the corresponding eigenvalue problem for slowly rotating stars; this conclusion was later put on a rigorous mathematical footing, see [91]. However it has also been pointed out there that the continuous spectrum might be just an artifact of the slow-rotation approximation. Another complication results from the coupling between polar and axial contributions in the corresponding perturbation equations since the inclusion of rotational effects leads to a set of equations with infinitely many coupling terms that have to be truncated after a specific polar index $l < l_m$ in order to be solved numerically, see [92, 93, 94, 95]. Depending on the compactness and the value of l_m, the continuous spectrum would change its location and width.

A natural question now would be if we see any traces of a continuous spectrum in our simulations. The following Figure 4.25 shows the result in the $(l = 2, m = 2)$-case.

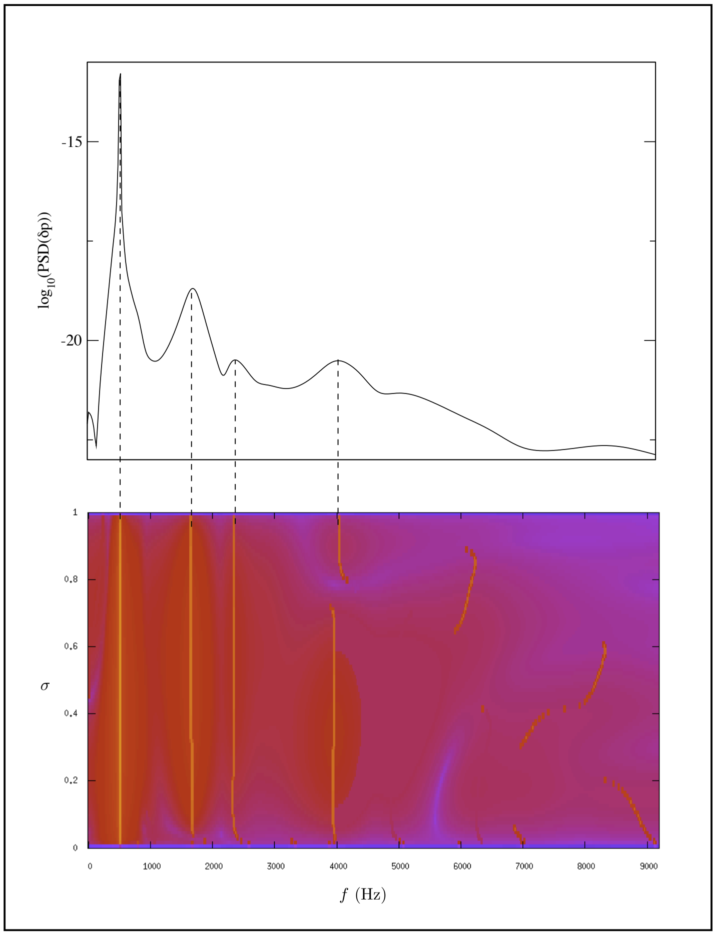

Figure 4.25: *Top Panel:* PSD plot of the $(l = 2, m = 2)$-pressure perturbation at $(\sigma, \tau) = (0.5, 0.5)$ *Bottom Panel:* Frequency distribution along a fixed value of $\tau = 0.5$ and varying radial distance σ

The top picture basically depicts the same circumstance as in the top right panel of Figure 4.24; this time the pressure perturbation is plotted. As usual in our simulations the arbitrary point $(\sigma, \tau) = (0.5, 0.5)$ is chosen to extract the time-series needed for the power spectral density calculation. The bottom picture shows the colour-coded PSD amplitude at a constant $\tau = 0.5$ and varying $\sigma \in [0, 1]$. If one recalls that σ can be interpreted as radial coordinate, this means that we move from the center of the star radially outwards to the surface at $\sigma = 1$. The straight vertical lines one can spot in this plot depict the radial variations of certain mode frequencies. As already discussed in this section, the peak at $f_1 = 518$ Hz belongs to the quadrupolar inertial mode. The next two peaks located at $f_2 = 1.68$ kHz and $f_3 = 2.34$ kHz can be identified with the co- and counterrotating branches of the $(l = 3, m = 2)$ fundamental mode while the last peak at $f_4 = 3.98$ kHz that is unambiguously discernable belongs to its first overtone; the node in radial direction is clearly visible. Since we performed mode-recycling specifically for the low-frequency inertial mode, the other more diffuse peaks at higher frequencies are pure numerical junk.
Keep in mind that $Y_2^3 \sim \sin^2\theta\cos\theta$ so we expect the shape of the pressure eigenfunction to feature two maxima and a node along the equatorial plane. The first overtone should additionally exhibit a node in the radial direction; something similar we have already seen in Figure 4.11 for axisymmetric pressure modes. The following Figure 4.26 shows the extracted shape of the eigenfunctions and confirms the assumptions.

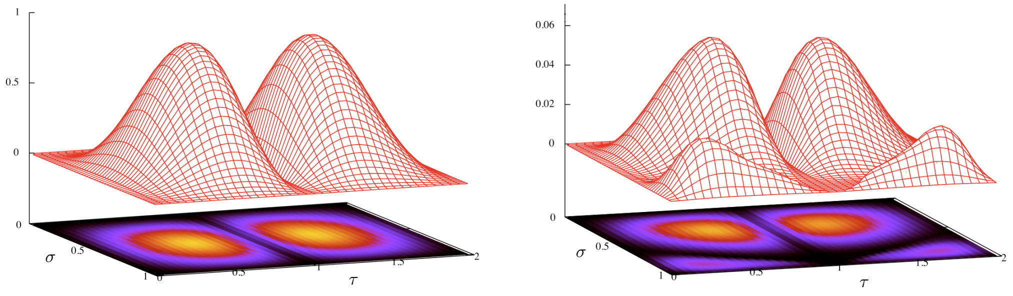

4.26.1: The shape of the $(l = 3, m = 2)$ pressure eigenfunction

4.26.2: The shape of the first $(l = 3, m = 2)$ overtone

Figure 4.26: Shape of the eigenfunctions from the dominant peaks in Figure 4.25

Now that the basic features of the PSD plot in the upper panel of Figure 4.25 have been determined, we can pick up the original problem about a possible continuous spectrum. As already discussed earlier, the different layers of the compact star would oscillate with different frequencies. Since the frame-dragging potential $\omega(r)$ is a monotonically increasing function of the radial distance, larger distance from the center of the star means higher oscillation frequency. It is pretty much evident from the bottom picture in Figure 4.25 that we cannot observe such a behaviour for the inertial mode depicted there. Instead of a tilt to the right we expect from a continuous spectrum, the peak stays at $f_1 = 518$ Hz for all radial points. Keep in mind that the background model is a BU6 star rotating at 93% of its

Kepler-limit, so we are definitely beyond the slow-rotation approximation. Another point worth mentioning is, that no decomposition of the angular part into spherical harmonics is used in our formulation of the perturbation equations. So concerning the coupling between polar and axial contributions, there is no need to constrain the coupling terms up to a certain polar order l_m since in principle all coupling terms are already included there. So in summary we have not seen any traces of a continuous spectrum in the simulations.

5

Summary and Outlook

In this thesis, we solved for the first time the linearized perturbation equations for fast rotating relativistic stars up to the Kepler-limit in the Cowling approximation. Instead of recasting the equations into an eigenvalue problem, the hydrodynamic evolution variables were directly integrated in time.

After a short and general introduction into the research field of stellar oscillations in Chapter 1, we began in Chapter 2 with the mathematical treatment of the problem. There, we derived the full nonlinear formulation of oscillations of compact objects within the framework of General Relativity. Since the nonlinear evolution of both the spacetime and the fluid is quite difficult, certain approximations may help to simplify this problem. First of all, the restriction to small perturbations leads to a set of coupled linear equations in which the evolution of the spacetime is still included. Second, the freezing of the spacetime to its stationary background values further reduces the complexity of the equations. In this so-called Cowling approximation only the fluid variables are treated as dynamical evolution quantities. Although these two approximations ease the numerical treatment of the original problem considerably, it has not yet been solved. We approached this issue with a novel formulation of the evolution equations in a comoving frame of reference. Due to a specific combination of background quantities and evolution variables, we derived a very elegant and simple set of equations and boundary conditions. We were also able to predict and proove analytically several properties of the evolution system which served as an additional test for the numerical implementation.

In Chapter 3 we developed an accurate and long-term stable algorithm for integrating the time-evolution equations derived in the preceding chapter. The background model we used was supplied as part of a collaboration within the SFB/TR7 and employed a rather novel numerical approach, i.e. so-called pseudospectral methods. We tried to extend this numerical technique also in the time-domain but it turned out that numerical instabilities near the rotation axis of the compact object eventually destroy the stability of the system. Actually, the rotation axis as well as the surface of the star are the critical regions, where all other codes have similar stability problems. It is the major reason why up to now this linear problem was an unsolved issue. For the first time we were successful in overcoming these instabilities. This was achieved by a transition to more traditional finite-difference schemes and the use of additional artificial viscosity terms in the equations. It turned out that these dissipation terms were the key ingredient for a stable time-evolution for all rotation rates up to the breakup-frequency.

After establishing a stable evolution scheme in Chapter 3, the subsequent Chapter 4 thoroughly tests this new code and compares its output with already published results. By explicitly adding artificial viscosity we are changing the original system that we wanted to solve initially. Hence it is not clear a priori what effect, if any, the additional dissipation terms have on the mode frequencies. For this reason its impact on the pristine set of equations was kept as small as possible. In the end it turned out that there is no apparent influence of the explicit viscosity on the oscillation frequencies. By varying the strength of the dissipation, there is only a negligible effect on the mode frequencies.

Our results, first tested in the case of axisymmetric perturbations, are in excellent agreement with nonlinear simulations; both for no rotation and rapid rotation. We were also able to extract the spatial variation of many eigenfunctions; an information that can be used as initial data in subsequent simulations for sharpening the frequency peaks. The long-term stability of the numerical code also allowed the study of low-frequency inertial modes that are only present in rotating stars. Our results for axisymmetric inertial modes in the Cowling approximation show excellent agreement with previous nonlinear simulations in the conformal flatness approach.

We then turned to the investigation on non-axisymmetric perturbations which are of special astrophysical relevance since they may lead to rotational instabilities and the emission of large amounts of gravitational radiation. Examining various polytropic equations of state, we were able to identify the neutral points of quadrupolar pressure-driven oscillations, i.e. the onset of the secular instability. One particular new result we found was, that when measured in the corotating frame of reference, the splitting of the fundamental quadrupolar mode into pro- and retrograde travelling waves proved to be independent of the specific EoS for a wide range of rotation frequencies. This might be crucial for future gravitational wave asteroseismology since it allows a robust determination of the masses and radii of rotating neutron stars.

Finally, we tested the code on non-axisymmetric inertial modes which are generically unstable to the emission of gravitational waves and which may explain the low rotation periods of young neutron stars. Again, the frequency of the fundamental quadrupolar inertial mode computed with our method agrees very well with other nonlinear simulations. Additionally, we addressed the still open question about the existence of a continuous spectrum for inertial modes. At least all the simulations carried out in this thesis show no trace of it.

Starting now from this established and well-tested code, one can take several directions. We can imagine at least two different tracks that can be tackled now. First of all we restricted ourselves in this thesis to study rapid, albeit uniform rotation. It is well known that especially in the very early stages of the creation of a neutron star, they will spin differentially. Differential rotation increases the maximum angular velocity a compact object can attain before it gets torn apart by centrifugal forces. Considering non-axisymmetric perturbation, this has two effects. First of all, even if the angular frequency of a uniformly rotating star is not high enough in order to drive a certain perturbation unstable, this may actually be the case for the corresponding differentially rotating star because of its larger Kepler-limit. Second, one knows from simulations in the slow-rotation approximation that the splitting between pro- and retrograde travelling modes is larger in the case of differential rotation, see for example [96], [97] . This will lead to an onset of rotational instability at even smaller rotation rates. But a systematic investigation of mode frequencies and eigenfunctions in the case of rapid differential rotation is still missing.

Another problem that can be addressed now is the effect of the dynamic spacetime on the oscillations. In this thesis we were still working in the Cowling approximation, i.e. the spacetime is fixed to its stationary background values. Dropping this assumption will lead to an improvement in the determination of the neutral points of the fundamental quadrupolar mode and of course also to a whole new class of oscillations; the w-modes. One finally would be able to compute in a self-consistent way the amount of gravitational radiation emitted as well as the exact waveforms. With the advent of gravitational wave astronomy, this task becomes even more important since it will allow the determination of fundamental stellar parameters from its gravitational wave signals. From a numerical point of view, the emission of gravitational radiation is just another dissipative mechanism. So instead of the artificial viscosity that is needed right now to stabilize the system against exponentially growing modes, maybe the dissipation of energy into the spacetime is the only viscous effect one needs for a stable evolution. Even if this turns out to be wrong, we now know how to apply artificial viscosity efficiently.

Finally, these two different approaches should be merged in order to provide a complete survey of oscillation modes of rotating compact objects within the framework of linear perturbation theory. This will prove to be an efficient tool for investigating rotational instabilities and thereby providing valuable information for future gravitational wave asteroseismology.

A

Proofs about the Perturbation Equations

A.1 A Toy Model

In this appendix we will prove some of the statements about the perturbation equations we made in Subsection 2.5.2. Before we do so it is worth to study analytically a simple linear toy problem; this will also illustrate the complex approach we are doing with the original equations. We will take a look at a coupled system of two equations and try to mimic the behaviour of the original perturbation equations (2.39)-(2.42) derived in 2.5.1. In order to make it manageable we will neglect all ρ- and ζ-derivatives and end up with our toy model we want to solve

$$\begin{aligned} \dot{u}_1 &= u_2 \\ \dot{u}_2 &= \partial_\varphi u_2 - u_1 \end{aligned} \tag{A.1}$$

with unknown functions $u_1 = u_1(\rho, \varphi, t)$ and $u_2 = u_2(\rho, \varphi, t)$.
The azimuthal part we decompose into periodic functions and since it it easier to work in a complex notation we will write

$$\begin{aligned} u_1 &= f \cdot e^{im\varphi} \\ u_2 &= g \cdot e^{im\varphi} \end{aligned} \tag{A.2}$$

The system of equations (A.1) is linear which means that the final real solution is obtained by taking the real part of this decomposition. Inserting (A.2) into (A.1) leads to

$$\begin{aligned} \dot{f} &= g \\ \dot{g} &= im \cdot g - f \end{aligned} \tag{A.3}$$

where f, g are now functions of ρ and t only. With our $e^{im\varphi}$-approach we were able to get rid of the angular dependence completely. The next step is to transform this first oder system of coupled equations into an uncoupled second order system. Differentiating the first equation of (A.3) again with respect to time and inserting the second equation as well as the other way round will give us the desired result

$$\begin{aligned} \ddot{f} - im \cdot \dot{f} + f &= 0 \\ \ddot{g} - im \cdot \dot{g} + g &= 0 \end{aligned} \tag{A.4}$$

The evolution equations for f and g are therefore identical so it is sufficient to study the solution of one of these equations. The next step is to assume a harmonic time-dependence and to write

$$f(\rho,t) = \tilde{f}(\rho) \cdot e^{i\omega t}$$

We insert this into the first equation of (A.4) and we end up with a quadratic equation for the frequency ω.

$$\omega^2 - m\omega - 1 = 0 \tag{A.5}$$

Equation (A.5) has the two solutions

$$\omega_1 = \frac{1}{2}\left(m + \sqrt{m^2+4}\right) \qquad \text{and} \qquad \omega_2 = \frac{1}{2}\left(m - \sqrt{m^2+4}\right) \tag{A.6}$$

The general solution for f is therefore a linear superposition of the two fundamental solutions with frequencies ω_1 and ω_2. Together with some integration constants $a_1, a_2, \alpha, \beta \in \mathbb{R}$ we can write

$$u_1 = \mathrm{Re}\left(a_1 e^{i(\omega_1 t + m\varphi + \alpha)} + a_2 e^{i(\omega_2 t + m\varphi + \beta)}\right) \tag{A.7}$$

and a similar solution for u_2 accordingly.

For simplicity let us forget about the second fundamental solution for a moment and write ω for ω_1. In this case we have

$$\begin{aligned} u_1 &= a\cos(\omega t + m\varphi + \alpha) \\ u_2 &= b\cos(\omega t + m\varphi + \beta) \end{aligned}$$

Then it is

$$\begin{aligned} \dot{u}_1 &= -a\omega\sin(\omega t + m\varphi + \alpha) \\ &\overset{!}{=} u_2 = b\cos(\omega t + m\varphi + \beta) \end{aligned}$$

This equation can be satisfied by setting $\alpha = \pi/2$, $\beta = 0$ and $b = -a\omega$. Now let us look at the second equation of (A.1). With our just determined integration constants it follows that

$$\begin{aligned} \dot{u}_2 &= -b\omega\sin(\omega t + m\varphi) \\ &\overset{!}{=} \partial_\varphi u_2 - u_1 = -bm\sin(\omega t + m\varphi) - \frac{b}{\omega}\sin(\omega t + m\varphi) \end{aligned}$$

But this turns out to be exactly the condition (A.5) which is fulfilled for ω so indeed we have shown that

$$\begin{aligned} u_1 &= \frac{b}{\omega}\sin(\omega t + m\varphi) \\ u_2 &= b\cos(\omega t + m\varphi) \end{aligned}$$

is a solution of (A.1), the function $b = b(\rho)$ is thereby determined by the initial conditions. The analytic procedure we have presented here in the case of a simple coupled system of two differential equations we are applying numerically for the more complicated system (2.39)-(2.42) of four coupled equations with nonconstant coefficients. Of course we have to make a trade-off here: The price for getting rid completely off the dependence in the φ-component is that we are now solving four more equations (i.e. the imaginary parts as well) and then as a final step take the real part of the numerically obtained solution. The good point is that although it is not possible to solve the original system (2.39)-(2.42) analytically it is still possible to derive certain properties of this system which then can be checked during the simulations to test the integrity of our numerical implementation. This will be the subject of the next section.

A.2 Analytical Proofs

Let us consider the original set of evolution equations (2.39)-(2.42) and forget about the exact style of the coefficients. For the sake of simplicity we will set them to unity without loss of generality and study the system

$$\begin{aligned}
\dot{f}_1 &= H_{,\rho} + f_3 + H \qquad (A.8)\\
\dot{f}_2 &= H_{,\zeta} + f_3 + H \\
\dot{f}_3 &= im(f_3 + H) + f_{1,\rho} + f_{2,\zeta} + f_1 + f_2 \\
\dot{H} &= im(H + f_3) + f_{1,\rho} + f_{2,\zeta} + f_1 + f_2
\end{aligned}$$

As already discussed in 2.5.2 it becomes even more evident here that these four equations can be very well separated into two groups where the first two only differ in their spatial differentiation and the last two equations are identical here; this is of course because we set all coefficients to ±1.

Let now $\mathcal{A} = (a_1, a_2, a_3, A)$ be a solution of (A.8) for $m = m_0$. Since (A.8) is a system of complex differential equations it has a real part as well as an imaginary part. If we explicitly write down the corresponding equations, we arrive at eight real-valued equations of the form

$$\begin{aligned}
\dot{a}_1^{\mathcal{R}} &= A_{,\rho}^{\mathcal{R}} + a_3^{\mathcal{R}} + A^{\mathcal{R}} \\
\dot{a}_1^{\mathcal{I}} &= A_{,\rho}^{\mathcal{I}} + a_3^{\mathcal{I}} + A^{\mathcal{I}} \\
\dot{a}_2^{\mathcal{R}} &= A_{,\zeta}^{\mathcal{R}} + a_3^{\mathcal{R}} + A^{\mathcal{R}} \\
\dot{a}_2^{\mathcal{I}} &= A_{,\zeta}^{\mathcal{I}} + a_3^{\mathcal{I}} + A^{\mathcal{I}} \\
\dot{a}_3^{\mathcal{R}} &= -m_0 a_3^{\mathcal{I}} - m_0 A^{\mathcal{I}} + a_{1,\rho}^{\mathcal{R}} + a_{2,\zeta}^{\mathcal{R}} + a_1^{\mathcal{R}} + a_2^{\mathcal{R}} \\
\dot{a}_3^{\mathcal{I}} &= m_0 a_3^{\mathcal{R}} + m_0 A^{\mathcal{R}} + a_{1,\rho}^{\mathcal{I}} + a_{2,\zeta}^{\mathcal{I}} + a_1^{\mathcal{I}} + a_2^{\mathcal{I}} \\
\dot{A}^{\mathcal{R}} &= -m_0 A^{\mathcal{I}} - m_0 a_3^{\mathcal{I}} + a_{1,\rho}^{\mathcal{R}} + a_{2,\zeta}^{\mathcal{R}} + a_1^{\mathcal{R}} + a_2^{\mathcal{R}} \\
\dot{A}^{\mathcal{I}} &= m_0 A^{\mathcal{R}} + m_0 a_3^{\mathcal{R}} + a_{1,\rho}^{\mathcal{I}} + a_{2,\zeta}^{\mathcal{I}} + a_1^{\mathcal{I}} + a_2^{\mathcal{I}}
\end{aligned}$$

Here we denoted with a superscript whether we take the real part or the imaginary part of a complex perturbation variable. Now the first statement we want to proof is the following:

1. If $\mathcal{A} = (a_1^{\mathcal{R}}, a_1^{\mathcal{I}}, a_2^{\mathcal{R}}, a_2^{\mathcal{I}}, a_3^{\mathcal{R}}, a_3^{\mathcal{I}}, A^{\mathcal{R}}, A^{\mathcal{I}})$ is a solution of (A.8) for $m = m_0$ then it is

true that $\mathcal{B} = (b_1, b_2, b_3, B)$ is a solution to the same problem with $m = -m_0$ and

$$\begin{array}{rlrl} b_1^{\mathcal{R}} &= a_1^{\mathcal{R}} & b_1^{\mathcal{I}} &= -a_1^{\mathcal{I}} \\ b_2^{\mathcal{R}} &= a_2^{\mathcal{R}} & b_2^{\mathcal{I}} &= -a_2^{\mathcal{I}} \\ b_3^{\mathcal{R}} &= a_3^{\mathcal{R}} & b_3^{\mathcal{I}} &= -a_3^{\mathcal{I}} \\ B^{\mathcal{R}} &= A^{\mathcal{R}} & B^{\mathcal{I}} &= -A^{\mathcal{I}} \end{array}$$

In other words, if we multiply the imaginary parts of a $m = m_0$ solution with a factor of -1 we get another solution for $m = -m_0$.

The proof is quite straightforward; we will show it for the first equation of each group since the other calculations are practically identical. We have

$$\begin{aligned} \dot{b}_1^{\mathcal{R}} &= \dot{a}_1^{\mathcal{R}} = A_{,\rho}^{\mathcal{R}} + a_3^{\mathcal{R}} + A^{\mathcal{R}} = B_{,\rho}^{\mathcal{R}} + b_3^{\mathcal{R}} + B^{\mathcal{R}} \\ \dot{b}_1^{\mathcal{I}} &= -\dot{a}_1^{\mathcal{I}} = -A_{,\rho}^{\mathcal{I}} - a_3^{\mathcal{I}} - A^{\mathcal{I}} = B_{,\rho}^{\mathcal{I}} + b_3^{\mathcal{I}} + B^{\mathcal{I}} \end{aligned}$$

and for the second group

$$\begin{aligned} \dot{b}_3^{\mathcal{R}} &= \dot{a}_3^{\mathcal{R}} \\ &= -m_0 a_3^{\mathcal{I}} - m_0 A^{\mathcal{I}} + a_{1,\rho}^{\mathcal{R}} + a_{2,\zeta}^{\mathcal{R}} + a_1^{\mathcal{R}} + a_2^{\mathcal{R}} \\ &= m_0 b_3^{\mathcal{I}} + m_0 B^{\mathcal{I}} + b_{1,\rho}^{\mathcal{R}} + b_{2,\zeta}^{\mathcal{R}} + b_1^{\mathcal{R}} + b_2^{\mathcal{R}} \\ \dot{b}_3^{\mathcal{I}} &= -\dot{a}_3^{\mathcal{I}} \\ &= -m_0 a_3^{\mathcal{R}} - m_0 A^{\mathcal{R}} - a_{1,\rho}^{\mathcal{I}} - a_{2,\zeta}^{\mathcal{I}} - a_1^{\mathcal{I}} - a_2^{\mathcal{I}} \\ &= -m_0 b_3^{\mathcal{R}} - m_0 B^{\mathcal{R}} + b_{1,\rho}^{\mathcal{I}} + b_{2,\zeta}^{\mathcal{I}} + b_1^{\mathcal{I}} + b_2^{\mathcal{I}} \end{aligned}$$

If we now compare the final lines of the equations for $\mathcal{B}$ with the corresponding ones for $\mathcal{A}$ we see that they are of the same form except that m_0 is replaced by $-m_0$ which proofs our claim.

From here it is very easy to show the second statement, i.e.

2. The final, physical solution of the real initial value problem is independent of the sign of m.

If $z(\rho, \zeta, t) = u(\rho, \zeta, t) + iv(\rho, \zeta, t)$ is an arbitrary complex-valued perturbation variable that solves one of the equations in (2.39)-(2.42), then due to linearity the real part of $ze^{im\varphi}$ is the actual solution of the real-valued initial problem. It then follows that

$$\begin{aligned} \operatorname{Re}\left(ze^{im\varphi}\right) &= \operatorname{Re}\left[(u+iv)(\cos(m\varphi) + i\sin(m\varphi))\right] \\ &= u\cos(m\varphi) - v\sin(m\varphi) \end{aligned}$$

For $m = m_0 > 0$ we therefore have

$$\operatorname{Re}\left(ze^{im_0\varphi}\right) = u\cos(m_0\varphi) - v\sin(m_0\varphi)$$

For $m = -m_0 < 0$ the imaginary part of z switches its sign and then

$$\operatorname{Re}\left(ze^{-im_0\varphi}\right) = u\cos(-m_0\varphi) + v\sin(-m_0\varphi) = u\cos(m_0\varphi) - v\sin(m_0\varphi)$$

which proofs the claim.

B

Documentation of the Software Package

B.1 General Layout

Here, we will review the crucial parts of our software which are necessary to understand when performing simulations and data analysis. The various modules of the package are put into different directories, according to the tasks they have to perform. Starting at the top-level directory we have the module `akm` to compute equilibrium configurations of stationary compact stars with polytropic equations of state (non-rotating as well as rotating). For a couple of EoS we have already generated background solutions for a variety of rotation rates; the corresponding data files can be found in the second module `background_files`. The last folder at this level `complex` contains all the source code that is related to the time evolution, analysis of the frequency spectrum, mode recycling and other things; we will cover it in a moment. In many of the modules one will need the same information about important setup-data to specify before compiling the source code; most of them are gathered together in the appropriate `makefile`. Of particular interest are

- `M_OLD` The number of grid points in the numerical domain of the `akm` module for computing the background model.
- `M1` The number of grid points in the σ-direction of our code.
- `M2` The number of grid points in the τ-direction of our code. The total number of points in our numerical domain is `M1`·`2M2`.
- `T_MAX` The maximum number of timesteps for the current simulation.
- `TS` The size of the timestep for the current simulation (depends on the resolution).
- `T_OUT` Specifies, after how many timesteps data are written to an output file.

The module folder `complex` consists of several subpackages. In this folder one first has to use `initial_data_generator`, responsible for calculating appropriate initial data and there is `time_evolution`, the central module of this thesis which will perform the numerical integration of the perturbation equations. The remaining modules are post-processing and data-analysis tools. They consist of `recycling` to extract the full two-dimensional eigenfunction at a specific frequency, `dft` will compute the power spectral density (PSD) and

its frequency peaks of a given time series and `convenience` can be used to either modify certain aspects of a recycled eigenfunction before injecting it into a new mode recycling run or, since it is a very common task, to extract peak frequencies of PSD data without running again `dft` on all output files.
In the next few sections we will briefly review the different modules and explain their syntax. In any case, if a program is started without any additional arguments, a little help menu with basic information is being displayed.

B.2 The Modules

B.2.1 `akm`

As described in [57], an iterative Newton-Raphson method is used to compute highly accurate equilibrium structures of compact polytropic objects. An iterative scheme always needs a trial solution as starting point for the method and the data files in `background_files` can serve as this starting point. From there, one can explore the very large parameter space of solutions. In particular one can prescribe the ratio of polar coordinate radius to equatorial coordinate radius r_p/r_e and the central pressure p_c or for example r_p/r_e and gravitational mass M. One can also vary the value of the polytropic index N to study the effects of different equations of state and last but not least one of course can increase the accuracy of the model by adding more grid points.
The code uses dimensionless units, so since $G = c = 1$ in gravitational units one can use the polytropic constant K to get rid of the remaining dimension. In these units $K^{N/2}$ has units of length so this sets the fundamental length scale of the system and one can introduce dimensionless quantities, for example $\bar{\Omega} = K^{N/2}\Omega$ for the angular velocity or $\bar{M} = K^{-N/2}M$ for the mass.

B.2.2 `initial_data_generator`

This module imports a background model from `akm` and implements trial initial data for $l = 0, \ldots, 3$ according to [72]. Of course one can also program arbitrary initial data. The syntax is
⟨program_name⟩ and the following flags:
-N polytropic index
-b background model filename
-l l-value

B.2.3 `time_evolution`

This is the central module of the whole package. It imports an `akm`-generated background model and an initial data file and then performs a numerical integration of the perturbation equations. The output data files that are created periodically (as specified in the `makefile`) are stored in a specific folder; the `data`-folder. The post-processing and analysis tools then can access these files to perform their tasks. Since a successful time-evolution in our case only is possible with the utilization of artificial viscosity, the user of this module has to fine

tune the influence of this viscosity. This is done by varying the viscosity coefficients which are `#define`-statements in the header file righthandside.h. The syntax of this module is
⟨program_name⟩ and the following flags:
-b background model filename
-p initial data filename
-N polytropic index
-m m-value

B.2.4 `dft`

This tool takes the output files in the `data`-folder to compute a time series of all perturbation variables, the corresponding fourier spectra and also prints out the frequency peaks at one single point the user has to specify. The output files of this module are also stored in a specific folder; the `results`-folder. The syntax here is
⟨program_name⟩ and the following flags:
-b background model filename
-s σ-value for the evaluation
-t τ-value for the evaluation
-a φ-angle for the evaluation
-m m-value
-N polytropic index

B.2.5 `recycling`

This module will perform a mode recycling run on all data files in the `data`-folder. The user has to specify a frequency at which the eigenfunction, or in this case the amplitude of the corresponding peak in the fourier spectrum should be extracted. Since the peaks will differ slightly for the different perturbation quantities the user also has to specify a certain range in which the algorithm will search for peaks if it does not find one at the original peak frequency. Typically this range lies within the frequency resolution of the simulation. The proper syntax is
⟨program_name⟩ and the following flags:
-a φ-angle for the evaluation
-m m-value
-N polytropic index
-f frequency of the eigenfunction
-d allowed +/- deviation from the frequency in Hertz

B.2.6 `convenience`

The last tool is a convenience wrapper for all the little tasks one has to perform more or less repeatedly. For example it often happens that one wants to calculate the frequency peaks of a given PSD-file. It is not necessary to examine all the data files with the `dft`-module again; the work has already been done. In such a case this tool simply takes the fourier transform and recalculates its frequency peaks. Another task is the modification of eigenfunctions for a mode recycling run; this is also done here. The syntax is

⟨program_name⟩ and the following flags:
-f filename to modify or analyze
-o option (either 0 for peak analysis or 1 for eigenmode modification)

Bibliography

[1] S. Chandrasekhar. *Ellipsoidal figures of equilibrium.* Yale University Press, 1969.

[2] H. Shapley. On the nature and cause of cepheid variation. ApJ, 40:448–465, 1914.

[3] A.S. Eddington. *The Internal Constitution of the Stars.* Cambridge University Press, 1926.

[4] T. G. Cowling. The non-radial oscillations of polytropic stars. MNRAS, 101:367–+, 1941.

[5] P. Ledoux. Contributions à l'Etude de la Structure Interne des Etoiles et de leur Stabilité. *Memoires of the Societe Royale des Sciences de Liege*, 9:3–294, 1949.

[6] J. Papaloizou and J. E. Pringle. Non-radial oscillations of rotating stars and their relevance to the short-period oscillations of cataclysmic variables. MNRAS, 182:423–442, February 1978.

[7] B. L. Schumaker and K. S. Thorne. Torsional oscillations of neutron stars. MNRAS, 203:457–489, May 1983.

[8] K. D. Kokkotas and B. G. Schmidt. *Quasi-Normal Modes of Stars and Black Holes.* Living Reviews in Relativity. MPI for Gravitational Physics, 1999.

[9] H.-P. Nollert. Quasinormal modes: the characteristic "sound" of black holes and neutron stars. *Classical and Quantum Gravity*, 16:159–+, December 1999.

[10] S. Chandrasekhar. The Dynamical Instability of Gaseous Masses Approaching the Schwarzschild Limit in General Relativity. ApJ, 140:417–+, August 1964.

[11] K. S. Thorne and A. Campolattaro. Non-radial pulsation of general-relativistic stellar models. i. analytic analysis for $l \geq 2$. ApJ, 149:591–+, September 1967.

[12] R. Price and K. S. Thorne. Non-radial pulsation of general-relativistic stellar models. ii. properties of the gravitational waves. ApJ, 155:163–+, January 1969.

[13] K. S. Thorne. Nonradial pulsation of general-relativistic stellar models. iii. analytic and numerical results for neutron stars. ApJ, 158:1–+, October 1969.

[14] K. S. Thorne. Nonradial Pulsation of General-Relativistic Stellar Models.IV. The Weak-field Limit. ApJ, 158:997–+, December 1969.

[15] K. D. Kokkotas and B. F. Schutz. Normal modes of a model radiating system. *General Relativity and Gravitation*, 18:913–921, September 1986.

[16] K. D. Kokkotas and B. F. Schutz. W-modes - A new family of normal modes of pulsating relativistic stars. MNRAS, 255:119–128, March 1992.

[17] Y. Kojima. Two Families of Normal Modes in Relativistic Stars. *Progress of Theoretical Physics*, 79:665–675, March 1988.

[18] N. Andersson, Y. Kojima, and K. D. Kokkotas. On the Oscillation Spectra of Ultracompact Stars: an Extensive Survey of Gravitational-Wave Modes. ApJ, 462:855–+, May 1996.

[19] M. Shibata, T. W. Baumgarte, and S. L. Shapiro. The Bar-Mode Instability in Differentially Rotating Neutron Stars: Simulations in Full General Relativity. ApJ, 542:453–463, October 2000.

[20] S. Chandrasekhar. Solutions of two problems in the theory of gravitational radiation. *Physical Review Letters*, 24:611–615, 1970.

[21] J. L. Friedman and B. F. Schutz. Secular instability of rotating Newtonian stars. ApJ, 222:281–296, May 1978.

[22] J. N. Imamura, J. L. Friedman, and R. H. Durisen. Secular stability limits for rotating polytropic stars. ApJ, 294:474–478, July 1985.

[23] S. Yoshida and Y. Eriguchi. Gravitational radiation driven secular instability of rotating polytropes. ApJ, 438:830–840, January 1995.

[24] P. Kaaret, Z. Prieskorn, J. J. M. i. Zand, S. Brandt, N. Lund, S. Mereghetti, D. Götz, E. Kuulkers, and J. A. Tomsick. Evidence of 1122 Hz X-Ray Burst Oscillations from the Neutron Star X-Ray Transient XTE J1739-285. ApJ, 657:L97–L100, March 2007.

[25] N. Andersson. A New Class of Unstable Modes of Rotating Relativistic Stars. ApJ, 502:708–+, August 1998.

[26] J. L. Friedman and S. M. Morsink. Axial Instability of Rotating Relativistic Stars. ApJ, 502:714–+, August 1998.

[27] N. Andersson and K. D. Kokkotas. The R-Mode Instability in Rotating Neutron Stars. *International Journal of Modern Physics D*, 10:381–441, 2001.

[28] J. M. Weisberg and J. H. Taylor. The Relativistic Binary Pulsar B1913+16: Thirty Years of Observations and Analysis. In F. A. Rasio and I. H. Stairs, editors, *Binary Radio Pulsars*, volume 328 of *Astronomical Society of the Pacific Conference Series*, pages 25–+, July 2005.

[29] R. A. Hulse and J. H. Taylor. Discovery of a pulsar in a binary system. ApJ, 195:L51–L53, January 1975.

[30] L. Ju, D. G. Blair, and C. Zhao. Detection of gravitational waves. *Reports of Progress in Physics*, 63:1317–1427, 2000.

[31] N. Andersson and K. D. Kokkotas. Gravitational Waves and Pulsating Stars: What Can We Learn from Future Observations? *Physical Review Letters*, 77:4134–4137, November 1996.

[32] N. Andersson and K. D. Kokkotas. Towards gravitational wave asteroseismology. MNRAS, 299:1059–1068, October 1998.

[33] N. Andersson, K. D. Kokkotas, and B. F. Schutz. Space-time modes of relativistic stars. MNRAS, 280:1230–1234, June 1996.

[34] W. Kastaun. High-resolution shock capturing scheme for ideal hydrodynamics in general relativity optimized for quasistationary solutions. Phys. Rev. D, 74(12):124024–+, December 2006.

[35] Wolfgang Kastaun. *Developing a code for general relativistic hydrodynamics with application to neutron star oscillations*. PhD thesis, Eberhard-Karls Universität Tübingen, 2007.

[36] W. Kastaun. Inertial modes of rigidly rotating neutron stars in Cowling approximation. Phys. Rev. D, 77(12):124019–+, June 2008.

[37] Efstratios Boutloukos. *Oscillations of rapidly rotating neutron stars*. PhD thesis, Eberhard-Karls Universität Tübingen, 2006.

[38] S. Boutloukos and H.-P. Nollert. Eigenmode frequency distribution of rapidly rotating neutron stars. Phys. Rev. D, 75(4):043007–+, February 2007.

[39] Isabel Rica Méndez. *Zeitentwicklung langsam rotierender Neutronensterne auf allgemein-relativistischem Hintergrund*. PhD thesis, Eberhard-Karls Universität Tübingen, 2008.

[40] N. Stergioulas, T. A. Apostolatos, and J. A. Font. Non-linear pulsations in differentially rotating neutron stars: mass-shedding-induced damping and splitting of the fundamental mode. MNRAS, 352:1089–1101, August 2004.

[41] Charles W. Misner, Kip S. Thorne, and John Archibald Wheeler. *Gravitation*. W.H. Freeman and Company, 1973.

[42] Ray d'Inverno. *Introducing Einstein's Relativity*. Oxford University Press, 1992.

[43] R. Arnowitt, S. Deser, and C.W. Misner. The dynamics of general relativity. In L. Witten, editor, *Gravitation:An Introduction to Current Research*. Wiley, New York, 1962.

[44] Johannes Ruoff. *The Numerical Evolution of Neutron Star Oscillations*. PhD thesis, Eberhard-Karls Universität Tübingen, 2000.

[45] R. Emden. *Gaskugeln*. Teubner, 1907.

[46] S. Rosseland and G. Randers. On the Stability of Pulsating Stars. *Astrophysica Norvegica*, 3:71–+, March 1938.

[47] P. N. McDermott, H. M. van Horn, and J. F. Scholl. Nonradial g-mode oscillations of warm neutron stars. ApJ, 268:837–848, May 1983.

[48] L. S. Finn. Relativistic stellar pulsations in the Cowling approximation. MNRAS, 232:259–275, May 1988.

[49] L. Lindblom and R. J. Splinter. The accuracy of the relativistic Cowling approximation. ApJ, 348:198–202, January 1990.

[50] S. Yoshida and Y. Kojima. Accuracy of the relativistic Cowling approximation in slowly rotating stars. MNRAS, 289:117–122, July 1997.

[51] J. A. Font, T. Goodale, S. Iyer, M. Miller, L. Rezzolla, E. Seidel, N. Stergioulas, W.-M. Suen, and M. Tobias. Three-dimensional numerical general relativistic hydrodynamics. II. Long-term dynamics of single relativistic stars. Phys. Rev. D, 65(8):084024–+, April 2002.

[52] H. Dimmelmeier, N. Stergioulas, and J. A. Font. Non-linear axisymmetric pulsations of rotating relativistic stars in the conformal flatness approximation. MNRAS, 368:1609–1630, June 2006.

[53] J. M. Bardeen and R. V. Wagoner. Relativistic Disks. I. Uniform Rotation. ApJ, 167:359–+, August 1971.

[54] H. Komatsu, Y. Eriguchi, and I. Hachisu. Rapidly rotating general relativistic stars. I - Numerical method and its application to uniformly rotating polytropes. MNRAS, 237:355–379, March 1989.

[55] N. Stergioulas and J. L. Friedman. Comparing models of rapidly rotating relativistic stars constructed by two numerical methods. ApJ, 444:306–311, May 1995.

[56] N. Stergioulas. http://www.gravity.phys.uwm.edu/rns/source/, 1995.

[57] M. Ansorg, A. Kleinwächter, and R. Meinel. Highly accurate calculation of rotating neutron stars. Detailed description of the numerical methods. A&A, 405:711–721, July 2003.

[58] Y. Kojima. Equations governing the nonradial oscillations of a slowly rotating relativistic star. Phys. Rev. D, 46:4289–4303, November 1992.

[59] A. Stavridis and K. D. Kokkotas. Evolution Equations for Slowly Rotating Stars. *International Journal of Modern Physics D*, 14:543–571, 2005.

[60] Claudio Canuto, M.Y. Hussaini, and Alfio Quarteroni. *Spectral Methods in Fluid Dynamics*. Springer Series in Computational Physics. Springer, 1988.

[61] John P. Boyd. *Chebyshev and Fourier Spectral Methods*. Lecture Notes In Engineering. Springer, 1989.

[62] Lloyd N. Trefethen. *Spectral Methods in MATLAB*. Society for Industrial and Applied Mathematics, 2000.

[63] V. Ferrari, L. Gualtieri, and S. Marassi. New approach to the study of quasinormal modes of rotating stars. Phys. Rev. D, 76(10):104033–+, November 2007.

[64] J. Hennig and M. Ansorg. A Fully Pseudospectral Scheme for Solving Singular Hyperbolic Equations. *ArXiv e-prints*, 801, January 2008.

[65] S. A. Teukolsky. Stability of the iterated Crank-Nicholson method in numerical relativity. Phys. Rev. D, 61(8):087501–+, April 2000.

[66] M. D. Duez, P. Marronetti, S. L. Shapiro, and T. W. Baumgarte. Hydrodynamic simulations in 3+1 general relativity. Phys. Rev. D, 67(2):024004–+, January 2003.

[67] M. D. Duez, Y. T. Liu, S. L. Shapiro, and B. C. Stephens. General relativistic hydrodynamics with viscosity: Contraction, catastrophic collapse, and disk formation in hypermassive neutron stars. Phys. Rev. D, 69(10):104030–+, May 2004.

[68] G. Leiler and L. Rezzolla. Iterated Crank-Nicolson method for hyperbolic and parabolic equations in numerical relativity. Phys. Rev. D, 73(4):044001–+, February 2006.

[69] Bertil Gustafsson, Heinz-Otto Kreiss, and Joseph Oliger. *Time dependent problems and difference methods*. Wiley, 1995.

[70] William H. Press, Saul A. Teukolsky, and William T. Vetterling. *Numerical Recipes in C*. Cambridge University Press, 1995.

[71] fftw@fftw.org. http://www.fftw.org/.

[72] J. A. Font, H. Dimmelmeier, A. Gupta, and N. Stergioulas. Axisymmetric modes of rotating relativistic stars in the Cowling approximation. MNRAS, 325:1463–1470, August 2001.

[73] G. B. Cook, S. L. Shapiro, and S. A. Teukolsky. Spin-up of a rapidly rotating star by angular momentum loss - Effects of general relativity. ApJ, 398:203–223, October 1992.

[74] G. B. Cook, S. L. Shapiro, and S. A. Teukolsky. Rapidly rotating polytropes in general relativity. ApJ, 422:227–242, February 1994.

[75] E. Gourgoulhon and S. Bonazzola. A formulation of the virial theorem in general relativity. *Class. Quantum Grav.*, 11:443–452, 1994.

[76] W. Unno, Y. Osaki, and H. Shibahashi. *Nonradial Oscillations of Stars*. University of Tokyo Press, 1989.

[77] J. L. Friedman. Generic instability of rotating relativistic stars. *Communications in Mathematical Physics*, 62:247–278, 1978.

[78] J. L. Friedman and B. F. Schutz. Lagrangian perturbation theory of nonrelativistic fluids. ApJ, 221:937–957, May 1978.

[79] J. L. Friedman and B. F. Schutz. On the stability of relativistic systems. ApJ, 200:204–220, August 1975.

[80] H. Sotani and K. D. Kokkotas. Probing strong-field scalar-tensor gravity with gravitational wave asteroseismology. Phys. Rev. D, 70(8):084026–+, October 2004.

[81] J. Diaz Alonso and J. M. Ibanez Cabanell. Field theoretical model for nuclear and neutron matter. II Neutron stars. ApJ, 291:308–318, April 1985.

[82] W. D. Arnett and R. L. Bowers. A Microscopic Interpretation of Neutron Star Structure. ApJS, 33:415–+, April 1977.

[83] D. I. Jones, N. Andersson, and N. Stergioulas. Time evolution of the linear perturbations of a rotating Newtonian polytrope. MNRAS, 334:933–940, August 2002.

[84] K. D. Kokkotas and N. Andersson. Oscillation and instabilities of relativistic stars. In R. Cianci, R. Collina, M. Francaviglia, and P. Fré, editors, *Recent Developments in General Relativity*, pages 121–139, 2002.

[85] K. H. Lockitch and J. L. Friedman. Where are the R-Modes of Isentropic Stars? ApJ, 521:764–788, August 1999.

[86] K. H. Lockitch, J. L. Friedman, and N. Andersson. Rotational modes of relativistic stars: Numerical results. Phys. Rev. D, 68(12):124010–+, December 2003.

[87] N. Stergioulas and J. A. Font. Nonlinear r-Modes in Rapidly Rotating Relativistic Stars. *Physical Review Letters*, 86:1148–1151, February 2001.

[88] S. Yoshida, S. Yoshida, and Y. Eriguchi. R-mode oscillations of rapidly rotating barotropic stars in general relativity: analysis by the relativistic Cowling approximation. MNRAS, 356:217–224, January 2005.

[89] Y. Kojima. Chapter 4. The Rotational Effects of General Relativity on the Stellar Pulsations. *Progress of Theoretical Physics Supplement*, 128:251–293, 1997.

[90] Y. Kojima. Quasi-toroidal oscillations in rotating relativistic stars. MNRAS, 293:49–+, January 1998.

[91] H. R. Beyer and K. D. Kokkotas. On the r-mode spectrum of relativistic stars. MNRAS, 308:745–750, September 1999.

[92] J. Ruoff, A. Stavridis, and K. D. Kokkotas. Inertial modes of slowly rotating relativistic stars in the Cowling approximation. MNRAS, 339:1170–1182, March 2003.

[93] J. Ruoff, A. Stavridis, and K. D. Kokkotas. Evolution equations for the perturbations of slowly rotating relativistic stars. MNRAS, 332:676–688, May 2002.

[94] J. Ruoff and K. D. Kokkotas. On the r-mode spectrum of relativistic stars: the inclusion of the radiation reaction. MNRAS, 330:1027–1033, March 2002.

[95] J. Ruoff and K. D. Kokkotas. On the r-mode spectrum of relativistic stars in the low-frequency approximation. MNRAS, 328:678–688, December 2001.

[96] A. Stavridis, A. Passamonti, and K. Kokkotas. Nonradial oscillations of slowly and differentially rotating compact stars. Phys. Rev. D, 75(6):064019–+, March 2007.

[97] A. Passamonti, A. Stavridis, and K. D. Kokkotas. Nonaxisymmetric oscillations of differentially rotating relativistic stars. Phys. Rev. D, 77(2):024029–+, January 2008.

[98] Jørgen Christensen-Dalgaard. *Lecture Notes on Stellar Oscillations*. Institut for Fysik og Astronomi, Aarhus Universitet, 1995.

Deutsche Zusammenfassung

Im Laufe ihres Evolutionszyklus können kompakte relativistische Objekte Instabilitäten unterworfen sein, die letztendlich zu Schwingungen des gesamten Sternes führen. So oszillieren beispielsweise neu enstandene Neutronensterne kurz nach ihrer Entstehung in einer Supernova-Explosion. Auch als Mitglied in einem kompakten Binärsystem kann es zu Schwingungen kommen, falls der enge Abstand zum Begleitstern zu Gezeitenkräften und dem damit verbundenen Austausch von Masse und Drehimpuls führt. Die Rotation dieser Objekte beeinflusst zusätzlich die zu erwartenden Oszillationsfrequenzen und überschreitet die Winkelgeschwindigkeit des Sterns einen bestimmten kritischen Wert, wird der ganze Stern dynamisch instabil. Abhängig von der Art der rückwirkenden Kraft werden Sternoszillationen in verschiedene Klassen unterteilt; jede von ihnen enthält wertvolle Informationen über das Sterninnere; einen Bereich also, den man mit anderen Mitteln nur schwer untersuchen kann. Es ist deshalb von besonderem Interesse, eben diese Schwingungen hochrelativistischer Objekte zu untersuchen.

Im Laufe der letzten etwa 20 Jahre sind solche Untersuchungen immer wichtiger geworden. Gegenwärtig werden große Anstrengungen unternommen, erstmals Gravitationswellen direkt nachzuweisen. Instabil schwingende Neutronensterne sind ein möglicher Kandidat für diesen Nachweis und die Analyse der von ihnen erhaltenen Gravitationsstrahlung liefert grundlegende Informationen über wichtige Parameter wie etwa Masse, Radius und die genaue Form der Zustandsgleichung supranuklearer Materie. Die meisten dieser Studien gehen jedoch von nichtrotierenden Sternen aus, da die Kombination von Rotationseffekten und Allgemeiner Relativitätstheorie sowohl analytisch als auch numerisch sehr schwer zu behandeln ist. Es wurden deshalb im Laufe der Zeit verschiedene Näherungen eingeführt; am naheliegendsten ist vermutlich die Beschränkung auf kleine Winkelgeschwindigkeiten. Dies ist eine Approximation, die sehr häufig in der Newtonschen Theorie von Sternschwingungen Anwendung findet.

Obwohl der Großteil unseres Wissens über die Oszillationen kompakter Objekte auf linearen Störungsrechnungen basiert, ist es in Einzelfällen auch gelungen, die vollen nichtlinearen, relativistischen Gleichungen der Hydrodynamik numerisch zu lösen. Außerdem wird auch daran gearbeitet, Effekte der differentiellen Rotation zu berücksichtigen; gerade für neu entstandene Neutronensterne ist dies von besonderer Bedeutung. Differentielle Rotation beeinflusst das instabile Verhalten sowohl langsam als auch schnell rotierender Neutronensterne, wurde bisher jedoch nicht ausführlich genug behandelt und ist momentan ein zum Großteil ungelöstes Problem.

Da dynamische Instabilitäten meist in Verbindung mit schnell rotierenden Neutronensternen auftreten, ist es von großem Interesse, die verschiedenen Oszillationen gerade diesen Types genauer zu untersuchen. Als ersten Schritt kann man dabei die schon weiter oben erwähnte Einschränkung auf kleine Winkelgeschwindigkeiten fallen lassen und gleichzeitig die dynamische Entwicklung der Raumzeit im Rahmen der Allgemeinen Relativitätstheorie vernachlässigen. Dies war bisher auch der Ansatz für die meisten Untersuchungen der Schwingungen schnell rotierender Neutronensterne, entweder auf störungstheoretischer Grundlage oder im nicht-linearen, axialsymmetrischen Fall.

In der vorliegenden Doktorarbeit wird eine neue Methode vorgestellt, welche die 2D Zeitentwicklungsgleichungen direkt numerisch integriert. Dies ist die erste Untersuchung ihrer Art; frühere 2D Störungsrechnungen wurden entweder vollständig innerhalb der Newtonschen Theorie ausgeführt oder durch einen harmonischen Ansatz auf ein Eigenwertproblem reduziert. Der Vorteil des neuen Verfahrens liegt darin, daß er ohne große Probleme auf differentielle Rotation und die dynamische Entwicklung der Raumzeit ausgeweitet werden kann. Auf der anderen Seite steht nun erstmals ein Werkzeug zur Verfügung, um Rotationsinstabilitäten in schnell rotierenden Neutronensternen zu untersuchen; eine Anwendung, die gerade im Hinblick auf die Gravitationswellen-Asteroseismologie von besonderer Bedeutung ist.

Curriculum Vitae

Persönliche Angaben

Name	Erich Gaertig
Familienstand	ledig
Staatsangehörigkeit	deutsch
Geburtsdatum	21.06.1976
Geburtsort	Piešt'any, Slowakische Republik

Schulbildung

1982 - 1986	Städtische Gemeinschaftsgrundschule Beverungen
1986 - 1992	Realschule Beverungen, Fachoberschulreife Juni 1992
1992 - 1995	Städtisches Gymnasium Beverungen Abitur Juni 1995, Note: 1,5

Wehr- / Zivildienst

1995 - 1996	Grundwehrdienst bei der Technischen Spezialkompanie 300 in Höxter

Wissenschaftlicher Werdegang

1996 - 2002	Studium der Physik an der Eberhard-Karls–Universität Tübingen, Diplom März 2002, Note 'sehr gut'
1999 - 2001	Wissenschaftliche Hilfskraft an der Fakultät für Mathematik der Universität Tübingen
2002 - 2008	Anfertigung der vorliegenden Dissertation *Linear Oscillations of Compact Stars in the Cowling Approximation* am Institut für Astronomie und Astrophysik der Universität Tübingen unter Anleitung von Prof. Dr. H. Ruder und Prof. Dr. K. Kokkotas
2002 - 2008	Wissenschaftlicher Angestellter am Institut für Astronomie und Astrophysik der Universität Tübingen

Akademische Lehrer

G. Betsch, H. Clement, A. Fäßler, H. Fischer, F. Gönnenwein, P. Grabmayr, W.-H. Hartmann, F. Hasselbach, R. Hübener, H. Kaul, F. Loose, E. Plies, H. Ruder, N. Schopohl, G. Wagner, K. Werner